Determination of Critical Aggregation Phenomena using Raman Spectroscopy

by

Geraldine Alice Annick Fournier

A thesis submitted in partial fulfillment of the requirements for the degree of

Master of Science

in

Chemical Engineering

Department of Chemical and Materials Engineering
University of Alberta

Abstract

The tendency of asphaltenes to aggregate in crude oil is observed at SATP and is enhanced at elevated temperatures. At these conditions, asphaltenes aggregation is a problem as it will ultimately lead to mesophase formation, a precursor of coke, known for causing plugging and fouling of pipelines and other equipment in refineries. It is becoming crucial to develop new technics using on-line sensors for characterization of heavy oil components in order to predict the onset of aggregation and prevent those shut downs.

Previous studies have been done to determine the early stages of asphaltene aggregation, also called CNAC, in organic solvents using absorbance, fluorescence spectrometry, calorimetric titration or thermo-optical diffusivity. The ultimate goal of this work is to develop an *in situ* technique that is able to track aggregation at reaction conditions by using Raman spectroscopy, even though no structural information is available. This thesis describes the foundations of the *in situ* technique at ambient conditions.

Aggregation of strongly associating model compounds such as surfactants was first investigated with Raman spectroscopy using a 785 nm laser. Intensity ratios as a function of the surfactant concentration showed progressive transitions which were interpreted as indicators of the critical micelle concentration. The good agreement with the literature encouraged the continued development of this method as an analytical tool to study the aggregation phenomena of highly complex associating compounds such as vacuum residue. Raman spectra of Athabasca VR solutions in toluene were observed in the concentration range between 0.1 wt. % and 0.0005 wt. % at room temperature and atmospheric pressure. Specific intensity ratios plotted *versus* the vacuum residue concentration showed a breakpoint around 0.006 wt. %. Such values were in agreement with the CNAC reported in previous articles. Therefore, Raman spectroscopy stands as an effective tool to detect and give reliable quantitative data for physical phenomena such as micellization and particles aggregation.

Acknowledgements

First and Foremost, I would like to thank Dr. William McCaffrey for his supervisions and suggestions during my studies. His guidance helped me in all time of research and writing of this thesis.

A very special thanks also goes to James Sawada who helped me prepare many experiments and offered much advice and insights throughout this project.

I would also like my lab colleagues and friends, David Dinh, Samuel Cardozo and Daniel Palys for their help, encouragements and all the unforgettable moments we spent together.

Finally, I thank my parents for the support they provided me throughout my studies at the University of Alberta and who cheered me up whenever I felt home sick.

Table of Contents

List of Tables

List of Figures

List of Symbols

α	polarizability
α_0	Polarizability when no vibration
c	speed of light, $cm.s^{-1}$
E	electric field, $V.cm^{-1}$
E_o	amplitude of the electric field
h	Planck's constant
K	stiffness of the spring, $N.m^{-1}$
λ	wavelength of the scattered photon, nm
λ_0	wavelength of the incident photon, nm
m_i	mass of atom i, kg/atom
P	induced moment, $V.cm^{-1}$
t	time, s
μ	reduced mass, kg/atom
ϑ_0	laser frequency, s^{-1}
ϑ_{vib}	vibrational frequency, s^{-1}
ϑ_{stokes}	frequency of the stokes photon, s^{-1}
$\vartheta_{anti-stokes}$	Frequency of the anti-stokes photon, s^{-1}
$\bar{\vartheta}$	Frequency expressed in wavenumbers or Raman shift, cm^{-1}
x_i	displacement of atom i from its equilibrium position, cm
X	internuclear distance, cm
X_0	vibrational amplitude, cm

1. Introduction

Petroleum is a valuable natural resource and is a major source of energy for the world, especially as a source of transportation fuels. Modern society is built and dependent on many other petroleum-derived chemicals and products such as plastic, detergents, fertilizers, pesticides or paint. It is estimated that 94 millions of barrels are consumed daily on a global scale and the demand is expected to continue growing for the next five years (1). As conventional oil world's reserves are however decreasing, the processing of unconventional resources such as extra heavy oil and bitumen are expending in order to meet this growing demand. The world's total bitumen reserves are estimated to be more than three trillion barrels, mainly located in Saudi Arabia, Venezuela and Canada. Proven oil sand's reserves in Canada are currently 168 billion barrels but potential reserves of bitumen in oil sand deposits are estimated to be 1.7 trillion (2), (3). Currently, 2.16 million barrels a day of oil sands are produced in Canada and the production is expected to reach 3.95 million barrels a day in 2025 (4). Although unconventional oils are found in abundant quantities, they possess a high content of undesirable high molecular weight and polar compounds such as asphaltenes. Normally concentrated in the vacuum residue portion collected at the end of the crude oil distillation process, asphaltenes can be however, found in any distilled fractions (5). The significant amount of asphaltenes in unconventional crude oils makes the transportation, the upgrading and refining processes more difficult (5). Asphaltene aggregation when diluent is added to unconventional bitumen for transportation is one example of the possible complications. As some bitumens are too dense and viscous to be transported, they are diluted with a mixture of lighter aromatics such as naphtha prior to shipping. Asphaltene aggregation results in the formation of deposits inside the pipelines and can lead to operational delays. Additionally, the presence of asphaltenes can trigger well boring, plugging and fouling of reactors as well as catalysts poisoning, resulting in massive shutdowns. This project investigates asphaltene aggregation inside organic solvents by modelling the bitumen-diluent mixture by solutions of vacuum residue in toluene. A wide range of instrumental methods were used to investigate the onset of asphaltene self-association in organic solvents (6) (7) (8) (9) (10) (11) but very few spectroscopic studies have been carried out on this subject. Previous work has used Raman spectroscopy to study basic reactions using standard solvents (12) and this project intends to study other physical changes such as surfactants micellization or asphaltene aggregation with the same technique. The critical micelle concentrations of standard surfactants in aqueous media have been largely studied and values obtained using different methods were reported to be in the same range. If the onset of micellization for such well-known systems can be detected from Raman spectroscopic studies, the same approach should be tested

for more complex phenomena such as asphaltene self-association in vacuum residue-toluene systems.

1.1. Thesis overview

The aim of this project is to investigate the onset of self-association for surfactants in different media and vacuum residue in organic solvents using Raman spectroscopy. This project can be described in four parts:

- The first part of this project aims to study the Raman signals of pure compounds in order to validate the experimental setup.
- The second part investigates the influence of intermolecular forces on the Raman spectra of weakly associating systems, in order to illustrate the challenges of working with interacting systems.
- A third part develops analytical tools to study the self-association of two surfactants, which are strongly associating model compounds.
- The last part of this project applies the model built for surfactants to the aggregation process of highly complex and unknown structures that are vacuum residue and asphaltenes.

2. Literature Review

The literature review covers the basic theory of Raman spectroscopy, as well as environmental factors influencing the Raman signal. This review features characteristics of simple diatomic species, basic hydrocarbon systems and more complex compounds such as bitumen or asphaltenes. Since crude oil constituents aggregate in organic media, it is important to understand the environmental phenomena involved in such processes and their consequences on the Raman signal. A subsequent section recounts the historical comparison of asphaltenes self-association with that of surfactants and provides a general background of such systems in different media. Finally, a description of the different techniques used to detect the onset of aggregation is provided and the use of Raman spectroscopy as a new method of detection for such phenomena is also discussed.

2.1. Vibrational spectroscopy

Raman scattering phenomenon is intimately correlated to the vibrational states of molecular bonds such as stretching, twisting and bending. Rotational transitions will not be treated, as they are unobservable in the condensed phases studied in this project. To introduce the basic principles of Raman spectroscopy, this section studies the stretching vibration of a diatomic molecule and treats the example of molecular bromine as an illustration throughout section 2.1. Such a molecule was chosen because it is, unlike most diatomic molecules, a liquid at room temperature. Other types of vibrations, allowed for molecules containing more than two atoms, such as bending or twisting, are mentioned in section 2.1.6.

The vibrations of a molecule can be described in two different ways. The difference in these explanations lies in how light is defined. The classical approach views light as a continuous oscillating field and subsequently performs the analysis based on approximations of the oscillating harmonic vibrational modes. Unlike the classical approach, light can also be defined as a beam composed of massless discrete photons which scatter based on their interactions with the sample. Both models can be used and combined together to describe the origin of Raman spectroscopy. Sections 2.1.1 and 2.1.2 explains the basic theory of bond vibrations through the harmonic approximation and section 2.1.3 uses a quantic point of view to give additional information about vibrational transitions.

2.1.1. The harmonic oscillator approximation

A diatomic molecule can be represented as a one-dimensional harmonic oscillator, where the two atoms, respectively of mass m_1 and m_2, are connected by a spring of stiffness K. The two atoms are considered to oscillate with the amplitudes x_1 and x_2 along the same axis. In this

system, stretching or compressing the spring creates potential energy, which is further converted into kinetic energy, inducing the movement of the two nuclei. The inverse mechanism also happens. The movement of the two nuclei for a harmonic oscillator, when the spring is stretched or compressed, is a function of time and is described by Equation 1.1 (13):

$$\left(\frac{1}{m_1}+\frac{1}{m_2}\right)\cdot\left(\frac{d^2x_1}{dt^2}+\frac{d^2x_2}{dt^2}\right)=-K\cdot(x_1+x_2) \qquad \text{Eq. 1.1}$$

m_1 and m_2 are the atomic masses of atoms 1 and 2 respectively and x_1 and x_2 are the displacements from their respective equilibrium positions. X is the nuclear distance between the two atoms and is defined as $X = x_1 + x_2$. By also combining the masses of both atoms into a reduced mass, μ, the equation can be solved as a one-particle problem.

$$\mu=\frac{1}{\frac{1}{m1}+\frac{1}{m2}} \qquad \text{Eq. 1.2}$$

μ is expressed in kg/atom and the force constant of the bond, K, is expressed in N.m^{-1}. As such, Equation 1.1 can be rewritten:

$$\mu\left(\frac{d^2X}{dt^2}\right)=-K\cdot X \qquad \text{Eq. 1.3}$$

The solution of this equation is harmonic and is defined as :

$$X=X_0\cdot\cos(2\pi\vartheta_{vib}t) \qquad \text{Eq. 1.4}$$

Where X is the internuclear distance as a function of the time, in cm, and X_0 is the vibrational amplitude, in cm. ϑ_{vib} is defined as the fundamental vibrational frequency of the stretching mode and is expressed in s^{-1}. ϑ_{vib} is described by the following formula, known as Hooke's law (13), (14).

$$\vartheta_{vib}=\frac{1}{2\pi}\cdot\sqrt{\frac{K}{\mu}} \qquad \text{Eq. 1.5}$$

This formula indicates that the stretching mode of the bond, also known as the fundamental vibration in this case, is associated with one vibrational frequency. The position of the fundamental in the Raman spectrum is influenced by two parameters: the reduced mass of the atoms and the spring stiffness. Heavier molecules will vibrate at lower frequencies whereas lighter molecules will vibrate at higher frequencies. For example, the stretching vibration of the C-H bond, of reduced mass, $\mu = 1.544.10^{-27}$ kg/atom, is localised above 3000 cm^{-1} and the

stretching vibration of the C-I bond, of reduced mass of $\mu = 1.82198.10^{-26}$ kg/atom, is localised around 500 cm^{-1} (15).

The waves per unit length or wavelength, $\bar{\vartheta}$, is more often used than ϑ_{vib} in Raman spectroscopy. Although it is expressed in cm^{-1}, it is usually referred as a frequency (14). This convention is followed in the rest of the thesis for simplicity.

$$\bar{\vartheta} = \frac{\vartheta_{vib}}{c} = \frac{1}{2\pi c} \cdot \sqrt{\frac{K}{\mu}} \qquad \text{Eq. 1.6}$$

In the above equation, c is the speed of light in $cm.s^{-1}$, and $\bar{\vartheta}$ is expressed in cm^{-1}. As an example, the molecule of bromine has a force constant of 203 $N.m^{-1}$ and a reduced mass of $\mu = 6.634.10^{-26}$ kg/atom. As such, Equation 1.6 predicts a fundamental vibration of 293.5 cm^{-1}, which is in good agreement with the frequency of 317 cm^{-1} reported in the literature (16).

The value of the bond force constant is highly influenced by the surrounding molecules and a change in environment might result in frequency shifts. More details are given in section 2.1.8.

2.1.2. Polarizability of a molecule/induced polarization

Raman spectroscopy relies on the interaction of monochromatic light with specific types of bonds within molecules. The light acts as the excitation source that changes the polarizability of the molecules. Although light is defined by its electric and magnetic components, only the electric field is taken into account in vibrational spectroscopy. The magnetic field will not be mentioned in the following sections, and the laser source is assumed to only interact via its electric field.

The laser, with an oscillating electric field E, of frequency ϑ_0, penetrates into the sample and interacts with the electronic clouds around the molecular bonds of the molecules, causing a charge separation inside the bond. The nuclei will be moved towards the negative pole, and the electrons will migrate towards the positive pole of the electric field. This process results in a modification of the polarizabilities, α, and the creation of an induced dipole moment or induced polarizability P (13). Figure 2-1 illustrates the movement of the electric charges inside a diatomic molecule inserted into an electric field.

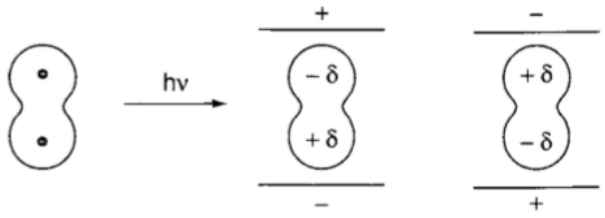

Figure 2-1: Charge distortion in a diatomic molecule when inserted into an electric field (13).

The polarizability measures the ease with which the electron cloud of a molecule can be modified by an external electric field. It is a good indicator of the electric charge displacement within the bond. A high polarizability results in a high induced polar moment and a strong Raman signal (13). The induced polarizability, P, is proportional to the electric field of the laser source and can be written (13), (15):

$$P = \alpha \cdot E = \alpha \cdot E_0 \cdot cos(2\pi\vartheta_0 t) \qquad \text{Eq. 1.7}$$

In the above equation, E is the electric field in V.cm^{-1}, E_0 is the amplitude of the electric field in V.cm^{-1} and ϑ_0 is the laser frequency in s^{-1}. The incident electric field and the polarizability oscillate with time at frequency ϑ_0.

The polarizability of a diatomic molecule is a function of the interatomic distance, X, in cm (17).

$$\alpha = \alpha_0 + \frac{\partial \alpha}{\partial X} \cdot X \qquad \text{Eq. 1.8}$$

α_0 is the polarizability of the bond when no vibration occurs and X is defined in Equation 1.4. Equation 1.8 shows that the polarizability fluctuates with the interatomic distance and time. The further apart the atoms are, the greater the polarizability, the easier the bond distortion and the stronger the vibration.

By combining Equations 1.4, 1.7 and 1.8, the induced polarization P, expressed in V.cm^{-1}, can be rewritten in Equation 1.9 as:

$$P = \left(\alpha_0 + \frac{\partial \alpha}{\partial X} \cdot X_0 \cdot \cos(2\pi\vartheta_{vib} t) \right) \cdot E_0 \cdot \cos(2\pi\vartheta_0 t) \qquad \text{Eq. 1.9}$$

Manipulation of Equation 1.9 results in Equation 1.10 (13), (17).

$$P = \alpha_0 \cdot E_0 \cdot \cos(2\pi\vartheta_0 t) + \frac{\partial \alpha}{\partial X} \cdot \frac{E_0 \cdot X}{2} \cdot [\cos(2\pi(\vartheta_0 + \vartheta_{vib})t) + \cos(2\pi(\vartheta_0 - \vartheta_{vib})t)] \qquad \text{Eq. 1.10}$$

Equation 1.10 shows that the induced dipole created inside the diatomic molecule is a function of the laser frequency and the stretching vibrational frequency of the bond. The first term in the equation, ϑ_0 , relates to Rayleigh scattering and the second terms, $\vartheta_0 \pm \vartheta_{vib}$, correspond to Raman scattering. Both concepts are explained in the following section in the light of quantum mechanics.

2.1.3. Rayleigh and Raman scattering

Scattering refers to the change of direction of the incident particles after interacting with other particles in the medium. When a sample is illuminated with a laser, 99% of the incident light is transmitted or reflected and only a miniscule fraction of the remaining 1% is scattered.

From a quantic point of view, the presence of electromagnetic waves from a laser source can be absorbed by an electron resulting in its excitation into a higher energy state, called virtual state, for a short period of time. Electrons excited to a higher energy state then emit a photon upon their return to the ground level and the energy of scattered radiation is measured by Raman spectroscopy. The frequency of the released photon can either be of the same as the laser source, i.e. ϑ_0, or it can be of a different frequency, i.e. $\vartheta_0 \pm \vartheta_{vib}$.

Raleigh scattering is an elastic collision, meaning that the emitted photon is of the same frequency as the incident excitation source ϑ_0 because there is no loss of energy during the collision. The molecule, which is initially found on the fundamental ground level, acts like an antenna which retransmits the incident frequency. The process in which the electron returns to its ground state energy level is referred to as relaxation. Molecules are said to have isotropic polarizabilities when they exhibit Rayleigh scattering. Since Rayleigh scattering is of no interest for this thesis, all elastic scattering is removed from the backscattered light through the use of a notch filter, placed inside the probe.

Raman scattering, however, happens after inelastic collisions between the incident photons and the bonds within a molecule. In terms of potential energy, the incident photon of energy $h\vartheta_0$ will transmit a small portion of its energy to the electron cloud, sending it to a different vibrational level. The energy levels are quantified and their potential energy, noted $E_{pot,harmo}$, is given in Equation 1.11:

$$E_{pot,harmo} = \left(n + \frac{1}{2}\right) \cdot \frac{h}{2\pi} \cdot \sqrt{\frac{K}{\mu}} = \left(n + \frac{1}{2}\right) \cdot h \cdot \vartheta_{vib} \qquad \text{Eq. 1.11}$$

In the above equation, $E_{pot,harmo}$ is expressed in Joules, h is the Planck's constant, expressed in $kg.m^2.s^{-1}$ and n is the vibrational quantic number, which can only take integer values. The term υ is usually preferred to describe the quantic number but is not used in this thesis for clarity purposes.

According to Equations 1.11, the energy of the diatomic molecule can only take discrete values, i.e. $\frac{1}{2}\pi \cdot \hbar \cdot \vartheta_{vib}$, $\frac{3}{2}\pi \cdot \hbar \cdot \vartheta_{vib}$, $\frac{5}{2} \cdot \hbar \cdot \vartheta_{vib}$ and electrons can only be found on these levels of energies. The harmonic approximation only allows transitions between two adjacent vibrational states. Such energy variation is noted $\Delta E_{pot,harmo}$ and is defined as:

$$\Delta E_{pot,harmo} = h \cdot \vartheta_{vib} = h \cdot c \cdot \bar{\vartheta} \qquad \text{Eq. 1.12}$$

In the above equation, $\Delta E_{pot,harmo}$ is expressed in Joules. The vibrational frequency of the bond can be directly calculated by measuring the energy difference between the initial and final vibrational levels. Two types of Raman scattering can result in such energy variation and are referred a Stokes and anti-Stokes scattering. Figure 2-2 illustrates the energy transitions depending on the two types of Raman scattering introduced in Equation 1.10:

- The Stokes scattering, during which the electrons gain kinetic energy and level up on a higher energy level. Relaxation results in the release of a photon, whose energy is described in Equation 1.13.

$$\vartheta_{stokes} = \vartheta_0 - \vartheta_{vib} \qquad \text{Eq. 1.13}$$

  Where ϑ_{stokes} is the frequency of the Stokes scattered photon, ϑ_0 is the laser frequency and ϑ_{vib} is the vibrational frequency of the bond, all of them expressed in cm^{-1}. In the example of bromine illuminated by a 785 nm laser source, the Stokes line appears at $\frac{1}{785\ nm} - 316\ cm^{-1}$ =12738 cm^{-1} -316 cm^{-1} = 12422 cm^{-1}

- The Anti-Stokes scattering, during which the relaxation of the electron cloud from an vibrational excited state to the ground state, is accompanied by the release of a photon with a higher energy than the incident one. Equation 1.14 describes the energy of an Anti-Stokes photon.

$$\vartheta_{anti-stokes} = \vartheta_0 + \vartheta_{vib} \qquad \text{Eq. 1.14}$$

  Where $\vartheta_{anti-stokes}$ is the frequency of the Stokes scattered photon, ϑ_0 is the laser frequency and ϑ_{vib} is the vibrational frequency of the bond. All these frequencies are

expressed in cm^{-1}. The Anti-Stokes line for the fundamental vibration of bromine appears at 13054 cm^{-1}.

Figure 2-2 summarizes how the different types of scattering can be processed in the Raman spectrometer. A more detailed description of the equipment is given in section 3.1

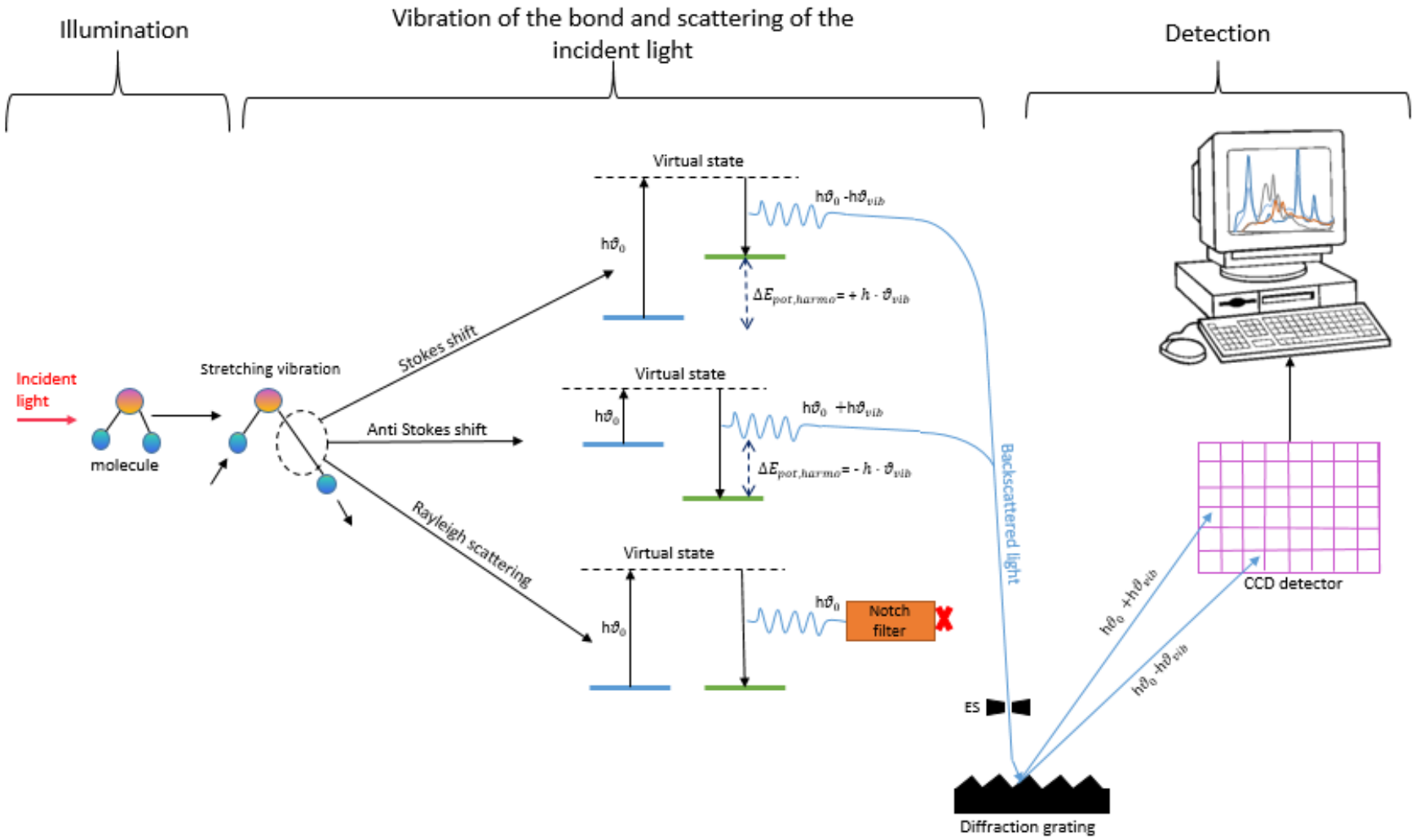

Figure 2-2: Overview of backscattered light processed inside the Raman setup. The energies of the scattered photons are calculated in the harmonic approximation. The initial energy levels are in blue and the final energy levels are presented in green. The energy difference between the two levels is represented by $\Delta E_{pot,harmo}$.

As previously stated, only a small portion of incoming light is scattered. The Rayleigh scattering only represents 10^{-3} of the incident light but has still a higher probability to happen than Raman scattering, which has an intensity 10^{-6} to 10^{-8} less intense than the exciting source (14), (15). The Stokes and anti-Stokes bands are symmetrically located on each side of the Rayleigh frequency. According to the Boltzmann law, more molecules are found in the ground level state than in the excited states, which makes the Raman Stokes scattering more likely to occur than the anti-Stokes scattering.

2.1.4. Modification of the harmonic oscillator approximation

Although the harmonic oscillator is adequate to explain the basic aspects of the vibrational theory, some features are not described in this model. Anharmonic terms need to be added to the harmonic potential E_{pot} to better describe the behaviour of the diatomic molecule. These new terms take into account non-ideal phenomena such as repulsion forces between the two atoms or the fact that a molecule cannot stretch indefinitely without breaking (17).

$$E_{pot,anharmo} = \left(n+\frac{1}{2}\right)\cdot\frac{h}{2\pi}\cdot\sqrt{\frac{K}{\mu}} - \left(n+\frac{1}{2}\right)^2\cdot\frac{h}{2\pi}\cdot\sqrt{\frac{K}{\mu}}\cdot x_e + higher\ terms \qquad \text{Eq. 1.15}$$

Where $E_{pot,anharmo}$ is the potential energy of the anharmonic oscillator expressed in Joules, n is the vibrational quantic number and x_e is an anharmonic constant.

The anharmonic model allows the presence of overtones, which are energetic transitions greater than $h\cdot\vartheta_{vib}$ (Eq 1.12) (14). Energy shifts which are observed from an energy level n = 0 to an energy level n =m result in a modification of the potential energy. Such energy difference is noted $\Delta E_{pot,anharm}(m)$ and described in Equation 1.16.

$$\Delta E_{pot,anharm}(m) = m\cdot h\cdot\vartheta_{vib} - \left(m+\frac{1}{2}\right)^2\cdot h\cdot\vartheta_{vib}\cdot x_e + \frac{1}{4}\cdot h\cdot\vartheta_{vib}\cdot x_e + higher\ terms \qquad \text{Eq. 1.16}$$

Equation 1.16 can also be modified in Equation 1.17:

$$\Delta E_{pot,anharm}(m) = \left[m - \left(m+\frac{1}{2}\right)^2\cdot x_e + \frac{1}{4}\cdot x_e + higher\ terms\right]\cdot h\cdot\vartheta_{vib} \qquad \text{Eq. 1.17}$$

Such transitions corresponding to Δn=±2, ±3, ±4, ±m result in the apparition of new bands located at frequencies proportional to the frequency of the fundamental (17). These bands also have different intensities than the fundamental vibration in the Raman spectrum. Figure 2-3

illustrates the concept of overtones for molecular bromine. In this simple example, the frequencies of the first, second and fifth overtones are almost multiple of the fundamental. Such wavelength can be predicted by using the harmonic potential.

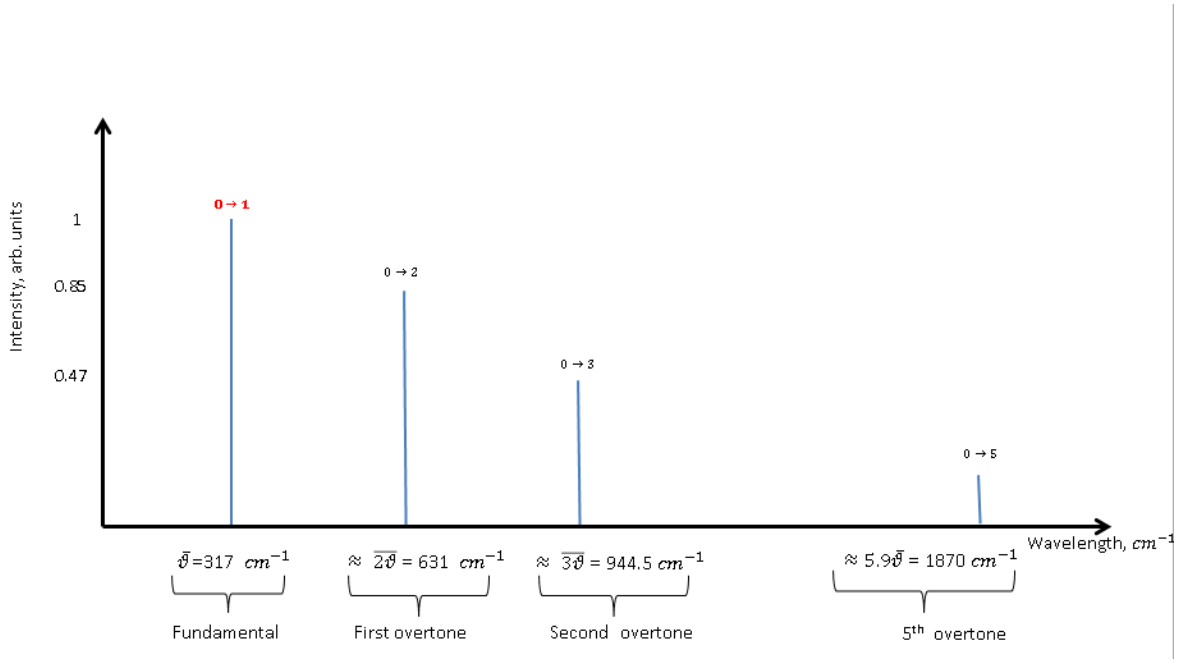

Figure 2-3: Representation of the fundamentals and overtones for the molecule of bromine (Br_2)

Additionally, both the harmonic and anharmonic models describe the presence of hot bands, which are transitions between excited adjacent energetic levels (17). As the vibrational levels are equally spaced in the harmonic model, the hot bands have the same frequency as the fundamental. In the anharmonic mode, however, hot bands do not necessarily result from the same energy transitions and have different frequencies. Figure 2-4 summarizes the concept of overtones and hot bands for molecular bromine.

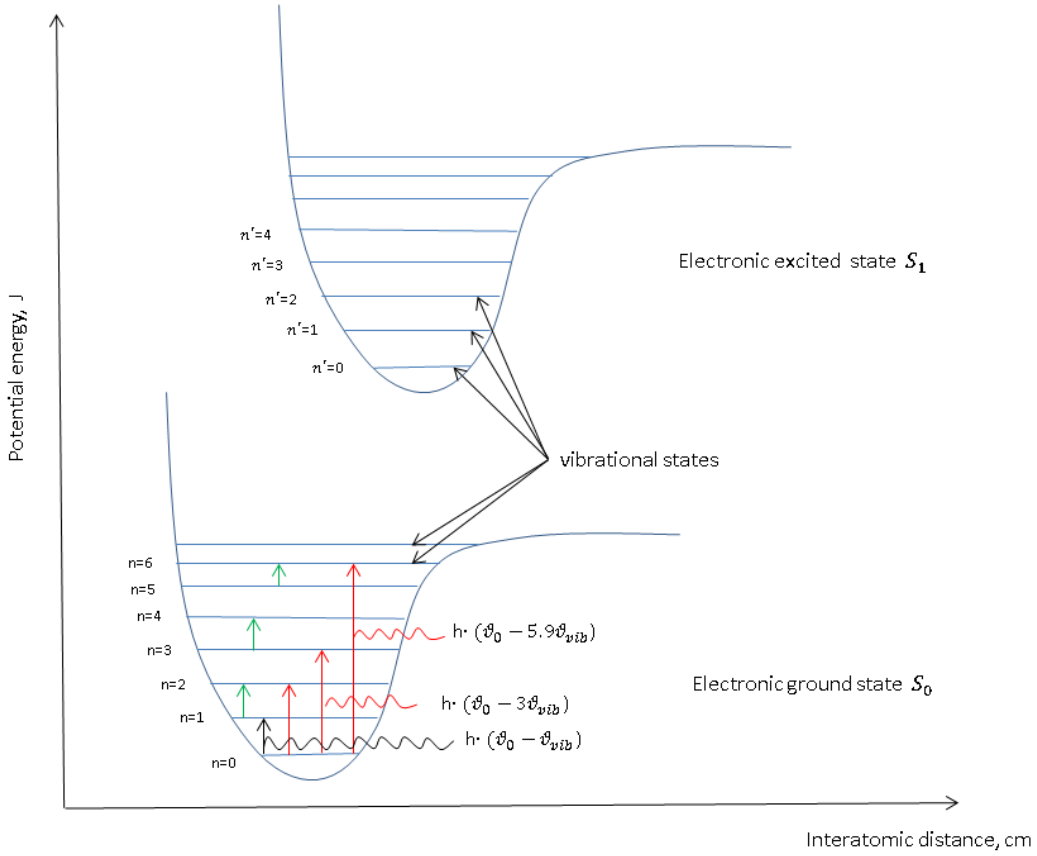

Figure 2-4: Electronic and vibrational energy levels for molecular bromine. The fundamental is illustrated by a black arrow, the overtones are illustrated by red arrows and the hot bands are illustrated by green arrows. Raman spectrometry measures the transition between the vibrational levels.

Overtones will introduce more bands whereas degeneracy, which occurs when two different vibrations have a similar or same frequency, results in less visible bands in the spectrum. Combination bands can also be observed when frequencies of vibrations add up, leading to the apparition of an extra band at higher frequency (18).

Finally, the anharmonic model can also predict Fermi resonance, which occurs when an overtone of one vibration or a combination band interacts with another fundamental. This is only possible when the frequencies of both bands are relatively similar (within 30 cm^{-1}) and that the symmetry of both vibrations are suitable. Fermi resonance can result in a displacement of bands and an unexpected intense overtone band, explaining the presence of two bands instead of the expected fundamental (14), (17), (18).

The anharmonic model is more adapted to explain the theory of Raman spectroscopy because it explains the presence of overtones, hot bands, combination bands and Fermi resonance whereas

only fundamental transitions and other transitions to adjacent energy levels where described by the harmonic model. As illustrated in the previous sections, the Raman signal of a simple molecule like bromine does not come down to one fundamental vibration. As such, polyatomic molecules or mixtures, affected by a wide range of environmental factors, are expected to give multiple and more complex Raman signals.

2.1.5. Raman shift

Raman spectrometers usually collect the Stokes scattered radiation, which is a vibrational unit different from the frequency of the incident light. Such a frequency variation was established in section 2.1.3:

$$\vartheta_{stokes=}\ (\vartheta_0 - \vartheta_{vib}) \qquad \text{Eq. 1.13}$$

The Raman shift, expressed in cm^{-1}, is defined as the difference between the wavelength of the scattered photon and the incident photon. As such, it should be written $\Delta\bar{\vartheta}$ but is often referred as $\bar{\vartheta}$ for brevity.

$$\bar{\vartheta} = \left(\frac{1}{\lambda_0} - \frac{1}{\lambda_{stokes}}\right).10^{-7} = \frac{\vartheta_0}{c} - \frac{(\vartheta_0 - \vartheta_{vib})}{c} = \frac{\vartheta_{vib}}{c} \qquad \text{Eq. 1.16}$$

In the above equation, λ_0 is the wavelength of the incident photon in nm, λ_{stokes} is the wavelength of the scattered photon in nm, ϑ_0 and ϑ_{vib} are expressed in s^{-1} and c is the speed of light in $cm.s^{-1}$.

Equations 1.6 and 1.16, which are established in the classical and quantic approaches respectively, show that the Raman shift is independent of the excitation wavelength. The choice of the laser, however, influences other parameters of the Raman signal and will be discussed in section 3.1.1.

The Raman spectra are typically presented in the form of a plot of Raman shift *versus* intensity. For pure compounds, the intensity of the Raman spectrum is directly proportional to concentration.

2.1.6. Selection rules

2.1.6.1. Change of polarizability

In order for Raman scattering to occur, one important criteria must be met. These are referred to as selection rules and are further elaborated in this section. The first selection rule comes from Equation 1.10 and states that a vibration is Raman active only if it changes the polarizability of the bond (14). In other words, a vibration is Raman active only if it modifies the

amplitude of the dipole moment oscillations. The peak intensities are directly related to the value of $\frac{\partial \alpha}{\partial X}$. Vibrations which result in a high polarizability variations are characterized by high intensities in the Raman spectrum. If this condition is not met, only Rayleigh scattering occurs and no information about the vibrational modes can be obtained.

2.1.6.2. Symmetric properties

The second rule is based on symmetric considerations and predicts if a molecule is likely to have a strong Raman or IR signal. Centrosymmetric molecules are generally sensitive to inelastic scattering, making Raman spectroscopy a powerful technique to detect and analyse these types of compounds (14). The rule of mutual exclusion for centrosymmetric molecules states that vibrations cannot be both Raman and IR active. Vibrations, which are not symmetric to the center of symmetry, are Raman inactive but IR active. Any vibration, however, which is symmetric to the center of symmetry, is Raman active but is not observed in the IR spectrum (15)

2.1.6.3. Raman spectroscopy as a fingerprint method

Intensities and frequencies in the Raman spectrum are characteristic of the sample studied and can be estimated for simple molecules. Molecules composed of heavy atoms such as iodine, bromine, chlorine and heavy metals have loose electric clouds that can be easily displaced by an electric field. Consequently, any bond involving these atoms is likely to be characterized by a strong Raman signal. Additionally, covalent bonds are characterized by intense bands whereas ionic bonds have usually weak Raman signals. As an example, electronegative atoms within polar bonds attract electrons towards themselves and make electron displacement more difficult. This phenomenon will lead to weak Raman signals for chemical entities such as $O-H$ or $Cl-C$. Water is an example of such systems that result in a weak Raman spectrum. As the two ionic bonds of water undergo stretching or bending, their polarizabilities are modified with atom displacements. The polarizability variation, $\frac{\partial \alpha}{\partial X}$, is, however, not significant because of the difficult mobility of the electrons within the polar bonds. Such chemical entities have strong IR signals, as the electric field will not interact similarly with the two different parts of the bond. Chemical entities that give poor signals in Raman spectroscopy are easily detected when using IR spectroscopy, explaining why these techniques are often used to complement each other.

Pi bonds have a higher polarizability than single bonds as the electron clouds are localised outside of the nuclear axis and are further away from the nuclei. The change of polarizability triggered by atom displacements during vibrations is therefore greater for multiple bonds than

for single bonds. This can explain why carboxyl groups have a stronger Raman signals than hydroxyl groups.

Moreover, Raman spectroscopy can be designated as a fingerprint method as each bond is determined by a specific stiffness and a specific reduced mass. Depending on the nature of the atoms involved in the bond and the nature of the bond itself, each Raman active mode vibrates at one specific frequency ϑ_{vib}, with more of less intensity. Raman signals are proportional to the size and the nature of the molecular bonds in a molecule. Double and triple bonds are characterized by higher force constants and vibrate at higher frequencies (14).

Raman spectroscopy of simple structures can be predicted by adapting the harmonic approximation. The number of possible vibrations for a molecule is a function of each individual couple harmonic oscillators. The fundamental vibrations can be decomposed as individual normal modes of vibrations corresponding to each bond inside the molecule. This number is approximated to 3n-5 (3n-3(translational) -2(rotational)) for a linear molecule and 3n-6 normal modes of vibrations (3n-3(translational) -3(rotational)) for a nonlinear molecule, n being the number of atoms in the molecule (15). As an example, water is a nonlinear triatomic molecule and present three normal vibrations: symmetric stretching, asymmetric stretching and symmetric bending. The molecule of carbon dioxide, CO_2, is a linear triatomic molecule which has four normal vibrations: symmetrical and asymmetrical stretching as well two bending vibrations. Only the symmetrical stretching is Raman active in this molecule, all the other being IR active (15).

The rules predicting the Raman or IR activity of a molecule, as well as the number of Raman bands, were established in the case of diatomic or simple molecules and are not suited for complex and large entities. The group theory is a more accurate method, which classifies molecules into point groups using their geometrical properties and predicts the activity of normal vibrations for such molecules. The description and use of this mathematical model is, however, outside the scope of this project.

2.1.7. Raman spectroscopy for molecular scale characterization

The Raman and IR spectroscopies are two techniques that are able to provide information about molecular bond vibrations and changes triggered by inter and intra molecular interactions. Each technique relies on different physical phenomena. IR spectroscopy detects variations of dipolar moments, resulting from a wide range of infrared excitation waves, whereas Raman spectroscopy is sensitive to polarizability changes within a compound excited by a

monochromatic light. Vibrational modes which are both Raman and IR active have similar vibrational frequencies but do not exhibit the same intensity: A vibration showing a strong Raman signal is characterised by a weak or a non-existent IR signal and vice versa.

Raman and IR spectroscopy are complementary fingerprints methods and can be paired to obtain more precise data about the sample of interest. Only the Raman technique was chosen in this project because of the several advantages that are listed below:

- Raman spectroscopy is an ideal technique to study a wide range of materials. It is sensitive to homogeneity, the degree of disorder and the crystallinity of the sample. It is a non-destructive method.
- Raman spectroscopy does not require a thorough sample preparation. The nature and aspect of the sample does not affect the process. Liquids and solids can be directly analysed with minimal preparation.
- Since the Raman signals of glasses such as sapphire window are weak, samples can be placed inside a container and observed through a glass. This type of procedure makes observation of samples easier and faster.
- Raman spectroscopy is sensitive and can be used on small quantities.
- The use of a remotely located laser probe allows the analysis of the sample that can be subjugated in severe conditions with minimal damage to the equipment.
- Water has a weak Raman signal and a strong IR fingerprint. Therefore, the study of aqueous solutions is made easier in Raman spectroscopy compared to IR spectroscopy because water does not interfere and does not hinder the signal of the sample (13).

The next section reports the influence of environmental effects on the Raman signal.

2.1.8. Environmental factors influencing the Raman signal

2.1.8.1. Effect of the structural configuration

In standard hydrocarbon systems, Zhang *et al*. found that saturated groups such as methylene and methyl groups are localised in a specific region of the Raman spectrum, regardless of the unique molecular compound they are associated with (19). A related study by Stephenson showed that the C-H stretching band is located in the range 3064- 2880 cm^{-1} for all standard hydrocarbon species (20).

Differences can, however, be observable for hydrocarbons with different structures and with different environments. Although the Raman spectra of these species are fingerprints of the

common base groups such as methyl, methylene, branched methyl and naphthene, their vibrational frequencies are functions of their relative locations to other functional groups and are sensitive to geometric steric hindrances (19). For example, the methylene peak in cyclohexane is located 16 cm^{-1} away from the methylene peak in the n-hexane spectrum, observed differences is accounted for by cyclic tension.

Another factor, which can influences frequency shifts, is the degree of branching and ramification, as shown in the case of a C-H bond for a methylene group. Vibrational frequency for the most intense C-H stretching is reported at 2872 cm^{-1} for normal paraffin as compared to 2911 cm^{-1} for isoparaffin (19). Furthermore, the methylene and methyl peaks are found at slightly different positions in the Raman spectrum, depending on the presence and proximity of double bonds in the structure.

These observations justify why the Raman shifts for chemical functional groups are given over a range of shifts. Therefore, the assignment of a specific wavelength to a particular functional group is not encouraged.

The analysis becomes, however, more difficult when more than one compound is present in solution. Dollish predicted that mixtures of five to ten hydrocarbon species show approximately a dozen peaks in their Raman spectra but that the analysis gets more complicated as the number of chemicals increases (21). Frequency and intensity variations, overlapping and disappearance of bands should always be expected as molecular interactions and environmental conditions influence the general shape of the spectrum. Section 2.1.8.2 introduces the concept of intermolecular forces and illustrates some of their effects on the Raman signal.

2.1.8.2. Effect of intermolecular forces

Intermolecular interactions such as Van der Waals forces, electrostatic forces, charge transfer or hydrophobic interactions are commonly observed when mixing two or more chemicals together. Mixtures are referred as non-ideal solutions when their behaviour is affected by intermolecular interactions. The deviation from ideality depends on the nature of the compounds mixed together and becomes greater as the complexity of the structure increases or as the number of chemicals inside the solution increases. Much difficulty is encountered when modeling these forces as they tend to fluctuate with time. This section summarizes the effect of such physical phenomena on the Raman spectrum.

Intermolecular forces in binary and ternary systems were widely studied in the past. Many authors investigated the impact of these forces on different hydrocarbon mixtures in terms of

excess thermodynamic functions (22), (23). As for spectroscopic considerations, intensities and frequencies in the Raman signals of mixtures are affected by intermolecular forces and collisions between molecules.

Van der Waals forces are known to be of weak intensities, but their presence can be detected in the Raman spectra through the examination of intensity changes and wavelength shifts. As indicated by Equation 1.10, the incoming monochromatic light interacts with the molecules, resulting in the creation of an induced polarization P within the molecules.

$$P = \alpha_0 \cdot E_0 \cdot \cos(2\pi\vartheta_0 t) + \frac{\partial\alpha}{\partial X} \cdot \frac{E_0 \cdot X}{2} \cdot [\cos(2\pi(\vartheta_0 + \vartheta_{vib})t) + \cos(2\pi(\vartheta_0 - \vartheta_{vib})t)] \quad \text{Eq. 1.10}$$

Where ϑ_{vib} is the stretching vibrational mode, specific to the nature of the molecular bond. It is proportional to the square root of the bond strength, which is directly influenced by intermolecular forces. As an example, dipole-induced interactions occur when a non-polar molecule is in the proximity of a polar molecule. The electrons within the non-polar molecule will migrate inside the bond, resulting in a charge separation between the negative and positive charges. As such, the previously non-polar molecule now has an induced dipole, which has the same electronic direction as the dipole of the influencing polar molecule. With the new electron configuration, electron cloud densities can become quite localized. Such a change in electronegativity influences the values of vibrational modes from ϑ_{vib} to ϑ'_{vib} . As the frequencies of the Raman scattered photons are shifted from $\vartheta_0 + \vartheta_{vib}$ to $\vartheta_0 + \vartheta_{vib}{}'$ or from $\vartheta_0 - \vartheta_{vib}$ to $\vartheta_0 - \vartheta_{vib'}$, wavelengths shifts in non-ideal solutions will be observed. As thus, greater intermolecular interactions lead to greater shifts in the initial vibration frequency ϑ_{vib}.

Similarly, hydrogen bonding results in frequency shifts. This intermolecular force reflects the tendency of hydrogen atoms to interact with electronegative atoms. It is believed to be the strongest intermolecular force and usually weakens bonds within the affected molecule, resulting in a decrease of the vibrational frequency.

2.1.8.3. Fluorescence

Fluorescence is a light emission process related to the relaxation of an electronic excited state, which usually occurs in polyaromatic molecules or any other conjugated systems (24). Such molecules are defined as fluorophores and are one of the most abundant species found in heavy oil, vacuum residue or asphaltenes. Fluorescence is an intense phenomenon and is often seen as a problem in Raman spectroscopy as it covers up most of the Raman signal and can cause

saturation of the signal. The analysis is more complicated and sometimes impossible when working with highly fluorescent samples.

The fluorescence mechanism includes a two-stage relaxation process after excitation of the electron cloud to a higher electronic state S_1 (25). The first step includes successive radiationless relaxations from the excited vibrational states of S_1 to the lowest excited vibrational level of S_1. Such transitions release energy which is further dissipated. The second relaxation, from this excited state to the ground state S_0, is accompanied by the emission of fluorescent photon, which has a lower energy and a longer wavelength than the incident one. This reemission process usually takes between 10^{-9} to 10^{-7} seconds, as the fluorescence lifetime is comparable to the lifetime of singlet states. The fluorescence cycle is repeated until the fluorophore is permanently damaged. The number of emission-relaxation cycles that can undergo a molecule is dependent on its nature and the surrounding environment. This irreversible degradation, known as photobleaching, is explained in the section 2.1.8.4.

2.1.8.4. Photobleaching and phosphorescence

Photobleaching describes the irreversible destruction of fluorophores after exposing the sample to the laser light for a long period of time. Photobleaching can be described as a three-level mechanism. After absorbing a photon, the electrons level up from the ground state S_0 to an excited singlet state, S_1, just as in fluorescence. Instead of relaxing to lower energetic levels, the electrons are further excited to the first excited triplet state T_1, where their spins are no longer paired with the ground state electrons. The transition from a singlet state to a triplet state is called intersystem crossing and becomes favourable when the vibrational levels of the latter excited states are close together or overlapping. Electrons, which are already on excited states, i.e. S_1 or T_1, can absorb another photon and undergo a similar process (26).

The lifetime of the electrons on the triplet state is longer than on any singlet states, usually in the order of microseconds (25). This can be explained by the Pauli Exclusion Principle, which states that a pair of electron in the same energy level must have opposite spins. Therefore, the electrons have to reverse their spins one more time before cooling down to the ground state level S_0. Such a long stay on the triplet state enables the bond, and therefore the molecule, to irreversibly change conformation or undergo chemical reactions with the neighbouring molecules. Such interactions can degrade the molecule permanently. This phenomenon permanently decreases the background fluorescence and can be used in Raman spectroscopy as a preliminary step in order to increase the quality of the signal.

If the electrons change their spins before and relaxe to the ground energy state S_0, photons are reemitted. This mechanism is known as phosphorescence and is differentiated from fluorescence because the reemission process has a decay time, usually 10^{-4} to 10 seconds, which is the lifetime of a triplet state. Absorption, fluorescence, photobleaching and phosphorescence are illustrated in the Jablonski diagram, presented in Figure 2-5.

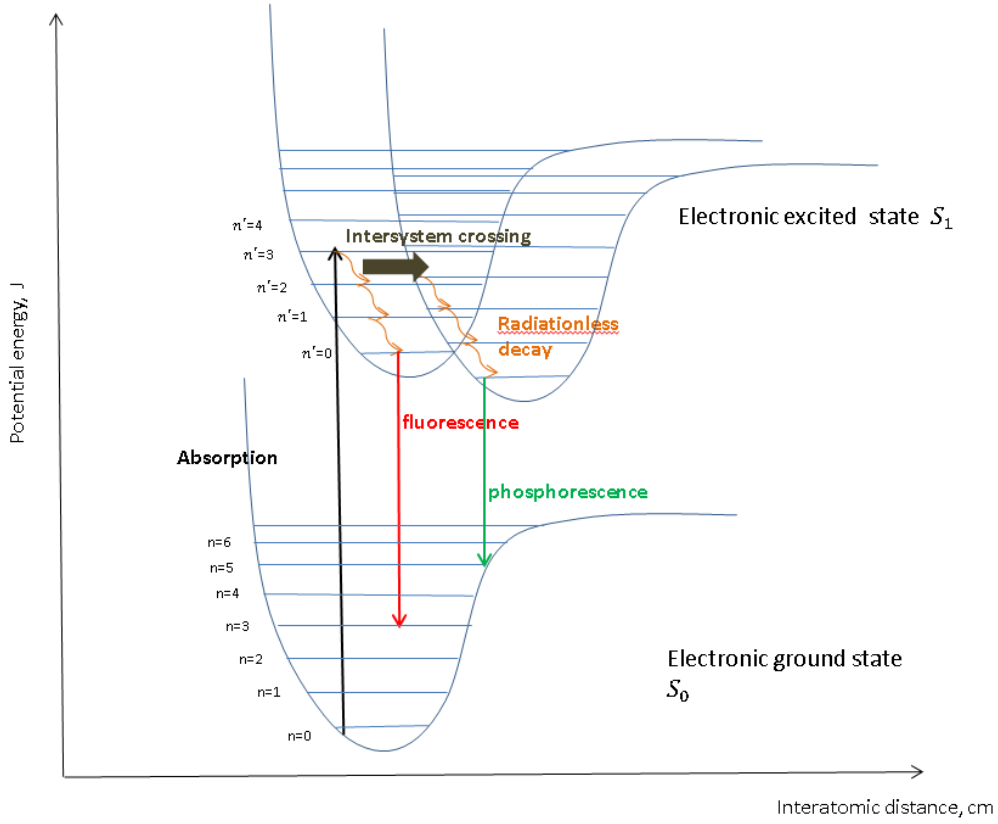

Figure 2-5: Jablonski diagram representing absorption, fluorescence, phosphorescence and photobleaching mechanisms.

The following section gives a review on the chemical structures and the Raman spectra of oil compounds.

2.2. Interacting systems- Example of hydrocarbon mixtures and oil components

2.2.1. Definition of the different oil fractions

Crude oil is a mixture of thousands of hydrocarbon species, resulting from the decaying of organic matter over millions of years in underground reservoirs. Depending on its source, crude oil's chemical composition and physical properties often vary significantly. Crude oil is typically categorized into two groups: conventional and unconventional oils. The first one refers to any crude oil extracted from the ground by the means of drilling systems based on natural well pressures with minimal heating. These oils usually have higher paraffinic and naphthenic concentrations and are characterized by low density or high ° API. Conventional oils can be easily transported via pipelines since they naturally have lower viscosities. Conversely, unconventional crude oils can have higher densities, low ° APIs and high viscosities. Bitumen is an example of an unconventional oil and is abundantly found in the Athabasca, Cold Lake and Peace River basins in Canada (5). With a density above 1000 kg/m^3 and a viscosity above 1000 mPa.s, bitumen is very challenging to recover and to convert into products. Given the vast size of such reservoirs, these oils present an option to replace the decreasing reserves of light crude oil. As extra heavy oils and bitumen do not flow easily, additional heating and pumping is required in order to extract them from the ground (5).

The processes behind the extraction, refining and upgrading of crudes are specifically designed based on the unique properties of the oil in question. Figure 2-6 illustrates the fractionation of the crude oil into different boiling ranges.

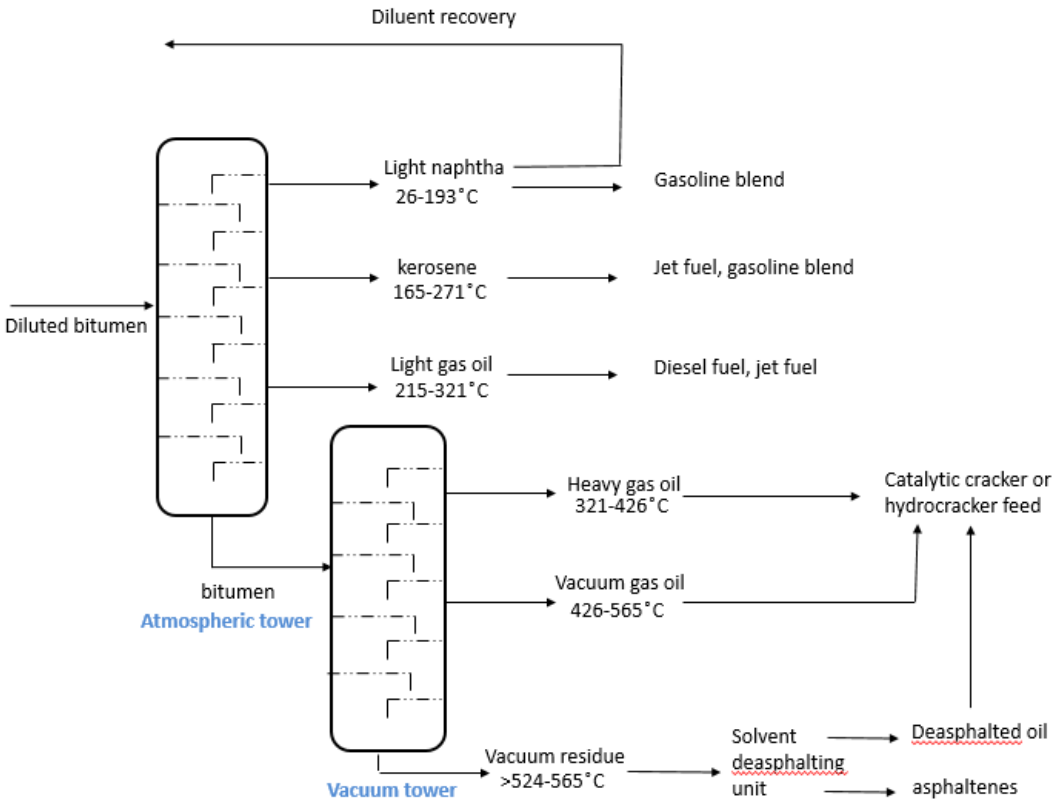

Figure 2-6: Generalized separation scheme of crude oil, adapted from Gray (5)

After extraction and preliminary treatments, the diluted bitumen is processed through an atmospheric distillation unit, where the solvent is recovered and the lightest oil fractions are fractionated. Such a process yields a variety of products including naphtha, kerosene or light gas oil. As an example, the naphtha fraction boils from 26°C to 193 °C and is further processed to recover the solvent used in the extraction process or mixed in the gasoline blend. Gasoline is a mixture of more than 500 hydrocarbons, mostly aliphatic in nature and containing on average four to twelve carbon atoms and some aromatics. Diesel, which is produced from the gas oil stream, has a similar composition as gasoline but contained longer hydrocarbons. The production of gasoline and diesel as transportation fuels is usually one of the main activities of a refinery.

In the case of heavy crude oils and bitumen, the bitumen collected at the bottom of the distillation tower is sent through a vacuum distillation unit. This unit is operated under vacuum to enable the fractionation of heavier compounds at lower temperature without causing thermal cracking (5). The heaviest fraction, which boils at temperatures equal or higher than 525°C, is known as vacuum residue (VR). This fraction is collected at the bottom of the vacuum distillation tower and consists in a mixture of all the products that could not be distilled. This

fraction is the richest in heteroatoms, asphaltenes and metal content and represents up to 50 vol. % of some heavy crude oil (5). The complex nature of VR makes it a difficult entity to analyse and to process but it certainly remains a key compound because of its abundance. Much work is being made to understand the chemical and physical structure of VR in attempt to find new applications.

2.2.2. Raman study of hydrocarbon systems and oil fractions

A variety of spectroscopic methods, such as thermal lens spectroscopy, UV-Vis and FTIR absorption spectroscopy, were used to gain insight into the structure of crude oil and its fractions. This thesis will focus on the use of Raman spectroscopy and some examples of Raman studies carried out on oil components are presented in this section. The case of gasoline is presented before crude oil as its Raman signal is easier to interpret.

2.2.2.1. Gasoline

Raman spectroscopy was used to study different samples of unleaded gasoline, 98 octane, from Denmark. When the Raman spectra were collected using a 514 nm laser, a wide fluorescence background was observed which prevented interpretation of the results. Hansen used NIR FT-Raman spectroscopy to reduce the noise (27). Both spectra obtained with the Raman and NIR-FT Raman spectroscopies are presented in Figure 2-7. The main peaks in the NIR-FT Raman spectrum were identified by comparing them with well-known standard compounds (27).

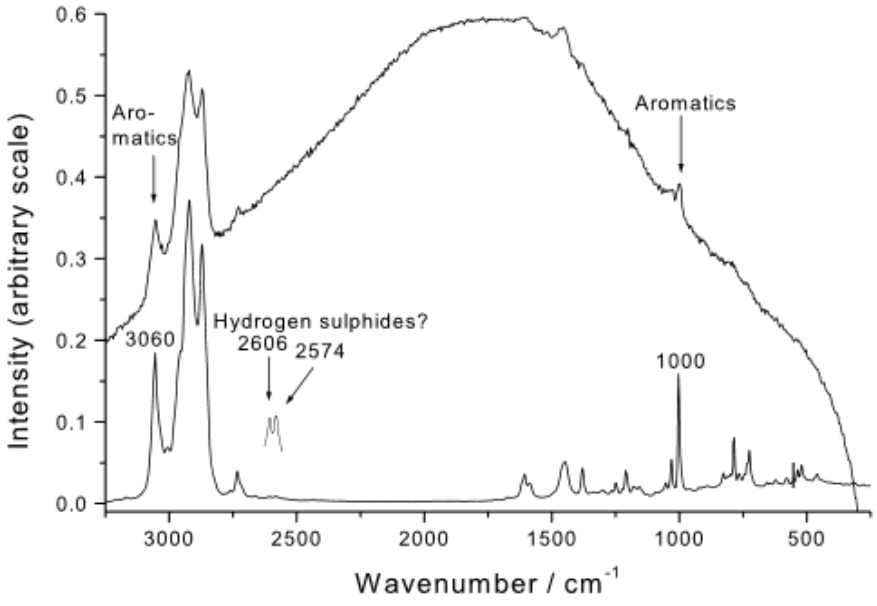

Figure 2-7: Raman spectrum of unleaded gasoline obtained with a 514.53 cm (upper curve) and Raman spectrum of the same sample obtained with NIR-FT Raman spectroscopy (lower curve) (27).

Peaks at 3060 cm^{-1} and 1000 cm^{-1} were directly assigned to the carbon-hydrogen symmetric stretching (C-H symmetric stretching) and carbon-carbon benzene stretching (C-C benzene stretching) vibrations respectively by comparing them with vibrations of pure benzene (3063 cm^{-1} and 993 cm^{-1}). Heptane was also used as a model compound for gasoline. Bands at 1450 cm^{-1} and 1300 cm^{-1} found in the Raman spectrum of pure heptane, which are attributed to C-H bending and CH_2 in phase twisting respectively, are located around the same area in the NIR FT-Raman spectrum of gasoline.

Comparison with the literature for H_2S, R-SH and Ar-SH systems enabled the identification of the higher frequency peaks. Peaks at 2606 cm^{-1} and 2574 cm^{-1} in the Raman spectrum of gasoline were assigned to the S-H stretching similar to that observed in hydrogen sulphide and in alkanethiols. Although all the previous bands were easily attributed to the vibrations of standard molecules, the study of other bands requires more care. There is an intense band observed at 2875 cm^{-1} in gasoline. Caution must be used in attributing this band to a specific type of bond since there are at least three separate phenomena that will result in adsorption at 2875 cm^{-1}:

- The CH_3 and CH_2 stretching vibration in the range of 3120-2862 cm^{-1}.
- The coupling of one CH_3 bending vibration overtone with the CH_3 symmetric stretching at 2865 cm^{-1} in substituted aromatics.
- Considering that the band at 2875 cm^{-1} in the spectrum of gasoline is also intense, it might also be the results of overtones and fundamentals combinations.

Another band observed at 726 cm^{-1} in the spectrum of gasoline can either be assigned to MTBE (Methyl Tertiary Butyl Ether), which is a fuel additive or to the C-C stretching vibration located at 722 cm^{-1}.

The example of gasoline shows the difficulties and limits of spectral interpretation. Some of the peaks were easily assigned whereas some bands could not be attributed with absolute certainty. This results from shifts in frequencies and intensities due to interactions between aromatics and other compounds in gasoline.

2.2.2.2. Raman spectrum of light crude oil

The Raman spectra of light crude oil is more complicated than gasoline and is characterised by the presence of aliphatic and cyclic alkanes, unsaturated hydrocarbons, aromatic molecules and functional groups including sulphur and other heteroatoms. Orange *et al.* showed that highly fluorescent crude oil samples can be studied with the Raman spectroscopy by using a 488 nm

laser (24). The Raman spectra of two different light crude oils from Washington State with similar chemical compositions and densities were analysed. When compared, these spectra showed similarities such as methylene scissor vibrations in the range 1470-1430 cm^{-1} and CH_2 rocking in the 1310-1175 cm^{-1} region, both of which are good indicators of the proportion of methylene groups inside the oil. Other common peaks were assigned to specific vibrations such as ring stretching vibrations of aromatics around 1600 cm^{-1}, benzene breathing mode in the 1010-900 cm^{-1} region and thiol vibrations in the 2600-2400 cm^{-1} range. As the complexity of the crude oil increases, the number of interactions increases and the fluorescence can become greater, obstructing the Raman signal. Basic interpretations of Raman spectra for light crude oils can be possible when the fluorescence is minimised.

2.2.2.3. Raman spectrum of bitumen

The study of heavy oils adds another level of complexity. Unlike gasoline and light crude oil, which can be modeled as mixtures of aliphatic and aromatics, heavy oils have a much larger boiling point range and large degree of chemical variety due to the presence of functional groups, heteroatoms and metals.

Little work has been made to try to understand the Raman spectrum of bitumen, most likely due to its lack of clearly defined adsorption bands. Zhang *et al.* studied bitumen from the Yingdong 2 well and reported two clusters of peaks: One cluster with two major peaks at 1397 cm^{-1} and 1614 cm^{-1} and another cluster with peaks at 2970 and 3200 cm^{-1}. No definitive assignment was made for these major peaks but the authors attributed the weak peaks at 2970 and 3200 cm^{-1} to methyl and methylene vibrations in bitumen. Jehlicka *et al.* used Raman spectroscopy to observe solid bitumens obtained from Klecany and Zbecno in Czech Republic, as illustrated in Figure 2-8 (28). The solid bitumen studied was formed in sedimentary rocks during the migration process of organic and hydrocarbon-rich matter in the Precambrian era. Although they also observed two clusters of peaks, their interpretation was slightly different from the one proposed by Zhang. The second high frequency cluster, with peaks at 2674, 2930 and 3140 cm^{-1}, was proposed to be overtones of the lower frequency peaks.

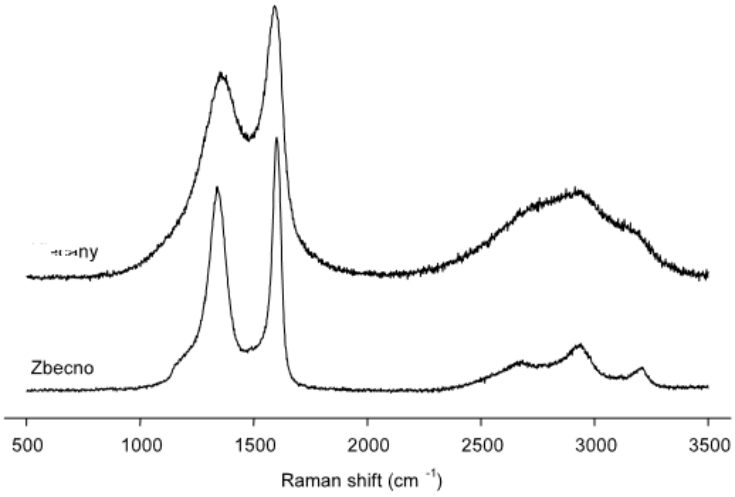

Figure 2-8: Raman spectra of two solid bitumen formed in sedimentary or metasedimentary rocks. Two samples were obtained from Klecany and Zbecno, located at 60 km from each other. (28)

The high number of functional groups and structures involved affects the presence and the location of the Raman fingerprinting bands. Each peak on these spectra is a combination of signals that are influenced by thousands of species interacting inside the sample. Other data analysis techniques such as the principal component analysis (PCA) are better candidates to study the Raman spectra of complex compounds. The PCA method describes the sample as a mixture of alternate components called principal components (PCs). The Raman spectrum appears as a matrix which is defined according to the PCs signals. The use of this technique is beyond the scope of this work.

This project aims to understand the effects of physical interactions before investigating the chemical composition of heavy feeds. VR contains a high proportion of asphaltenes, which aggregate in crude oil and organic solvents. This thesis focuses on the interfacial activities of such compounds in organic solvents. Section 2.3 studies associative model systems first in order to develop analytical tools.

2.3.Associative systems: Example of surfactants

2.3.1. Definitions and properties

Surfactants are defined as molecules that lower the surface tension of a liquid. They are commonly used as detergents, foaming agents or emulsifiers. The example of a water-air interface is treated in this section but the principle remains the same for other interfaces such as liquid/liquid systems. In aqueous solutions, molecules of surfactants have a tendency to migrate

to the air-water interface with their hydrophobic tails orientated towards the air while their hydrophilic head-groups remain in the aqueous medium.

Once the air-water interface becomes saturated, surfactant molecules begin to form spherical aggregates inside the solution with their ionic head-groups pointing towards the water and their hydrocarbon tails trapped inside the core. These surfactant aggregates are called micelles and minimize the contact between the hydrophobic tails and water. In a nonpolar environment, aggregates with the opposite configuration are formed. The formation of reverse micelles is driven by the strong repulsions between the polar groups of the surfactant and the organic solvent. The formation of micelles in water and reverse micelles in organic media are spontaneous phenomena, which occur when the concentration of surfactant reaches the critical micelle concentration (CMC). The literature does not report a specific CMC but rather a range. The CMC is an ill-defined concept because techniques used to determine this property are measurement dependent. Figure 2-9 represents the evolution of six physical parameters with the concentration of sodium dodecyl sulfate (SDS) in water as well as the concentration range reported for the CMC of SDS.

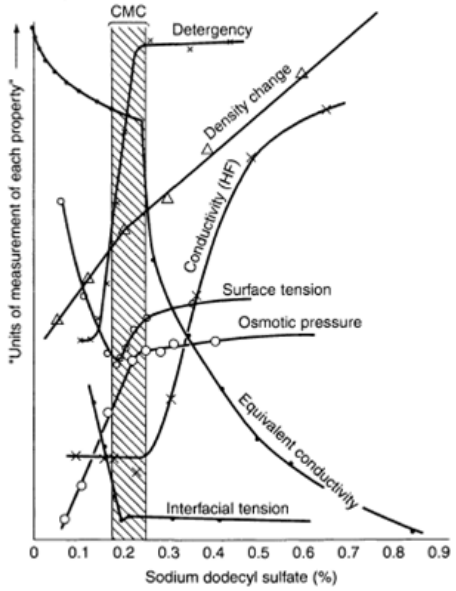

Figure 2-9: Illustration of the CMC range and the sharp transitions of different physical properties induced by an increase of the SDS concentration (29).

Depending on which measuring technique is used, the CMC ranges from 6.25 mmol/L (0.18 wt. %) to 8.7 mmol/L (0.25 wt. %). The tendency of a surfactant to form micelles in water and reverse micelles in organic media depends on its chemical composition and structure. The

hydrophilic-lipophilic balance number, HLB, measures the solubility of a surfactant and is one indicator of its association ability. It reflects the relative strength of the hydrophilic portion (head group) compared to the lipophilic part (hydrocarbon tail) of a surfactant molecule. Highly hydrophilic surfactants, which are easily miscible in water, have a high HLB number. Sodium dodecyl sulphate, SDS, with a HLB of 40, is an example of such surfactants. The head group of SDS, SO_4^- Na^+, is strongly hydrophilic in character. Dioctyl sulfosuccinate sodium salt, commonly referred to as Aerosol OT or AOT in the literature, is an example of a surfactant with a relatively low HLB of 7.7. This type of surfactant has poor solubility in water but is highly soluble in a broad range in organic polar and non-polar solvents such as toluene, cyclohexane and aliphatic hydrocarbons. AOT is able to stabilize water-in-oil microemuslions and to solubilize a large amount of water inside the reverse micelles. Microemulsions are thermodynamically stable systems that can be described as a water pool separated from the oil phase by a monolayer film of surfactant molecules. Section 2.3.4 gives more details about these structures.

The variations of different physical parameters with the concentration of surfactants such as surface tension, conductance or fluorescence ratios, show abrupt changes corresponding to the critical micelle concentration (30), (31), (32). Previous work showed that Raman spectroscopic study of intensity ratios can also be used to determine the critical micelle concentration of surfactants.

2.3.2. Raman study of normal micelles in water

The formation of micelles affects the structure and organisation of both surfactant and associated water molecules. Dolenko *et al.* investigated the influence of micelles on the surrounding molecules of water. They focused their work on the I(3414)/I(3260) intensity ratio, which represents the ratio of poorly bonded hydroxyl groups to the strongly bonded hydroxyl groups (33). An abrupt shift of this parameter was observed and interpreted as the onset of micellization. Other studies showed that the hydrocarbon chains of surfactants are sensitive to environmental changes and adopt different conformations depending on the surrounding medium (34). Raman spectroscopy is sensitive enough to detect these conformational changes and the Raman signals of aqueous solutions of different surfactants were investigated. In these studies, the region associated with skeletal C-C vibrations, 1150-1050 cm^{-1}, is highly informative. For solid SDS, two main peaks in this region of the Raman spectrum were reported at 1063 cm^{-1} and 1134 cm^{-1} and both attributed to all-trans skeletal vibrations (35). Another peak localised at 1080 cm^{-1} was attributed to the asymmetric C-C stretching in gauche conformation. In this same study, the investigation of the trans/gauche equilibrium with temperature was carried out by

looking at the evolution of I(1063)/I(1080) and I(1134)/I(1080) intensity ratios with temperature. It was observed that increasing the temperature resulted in broadening and intensification of the peak at 1080 cm^{-1} compared to the peaks at 1063 and 1134 cm^{-1}. As the temperature increases, the band at 1063 cm^{-1} appeared to become a shoulder of the large gauche characteristic band at 1080 cm^{-1}. The transition from a crystalline state, that is well ordered, to a liquid state, where molecules have more degrees of freedom, is accompanied by an increase of gauche conformations within the hydrocarbon tails. This explains the shift of the trans/gauche equilibrium as temperature increases. The micellization process can be compared to this system. Although the spontaneous formation of micelles results in the creation of a well-ordered system with a lower energy than when no micelles were present, the order of the hydrocarbon chains is disrupted. Before micellization, the alkyl tails are localised at the air-water interface and are surrounded by molecules of water and air. Once micelles start to form, a hydrocarbon micro-phase within the core of the micelles is created, allowing more degrees of freedom for the hydrocarbon tails. The comparison between this associative system with what happens when melting SDS leads to the assumption that hydrocarbon tails are more disordered in the core of the micelles and mainly adopt gauche conformations.

The addition of electrolytes such as sodium chloride (NaCl) in aqueous solutions of many surfactants was shown to result in a decrease of the CMC (31). The CMC of SDS for different concentrations of salt in water are reported in Table 2-1. These same values are given again in Table 4-9 in section 4.3.1.2 along with the values obtained in this project.

Table 2-1: Values of the CMC for SDS in aqueous solutions

Concentration NaCl (mol/L)	**Raman spectroscopy** I(3400)/I(3200) (33)	**Conductimetry** (31)	**Fluorescence** (32)	(30)
0	0.006	0.0078	0.0082	0.0073
0.02		0.0033		
0.1		0.0017		

As the concentration of salt increases, the position of the breakpoint, and therefore the CMC, shifts towards lower values. As illustrated in Table 2-1 and Figure 2-9, the value of the CMC is

measurement dependant. Such variability explains why the aggregation process of surfactant is more likely to occur throughout a CMC range rather than at a specific concentration.

2.3.3. Raman study of Dioctyl Sulfosuccinate Sodium salt (AOT) reverse micelles

Dioctyl sulfosuccinate sodium salt, or AOT, has the ability to form normal micelles in water and reverse micelles in organic solvents. In a nonpolar solvent, the polar head-groups of the surfactant associate with each other to lower the repulsions with the organic solvent and form reverse micelles. Studies using calorimetry, spectroscopy or water-soluble dyes reported a wide range of values for the critical micelle concentration of AOT in organic solvents. Selected results are presented in Table 2-2.

Table 2-2: values of the CMC for AOT in hydrocarbon solvents

	CMC (mmol/L)				
Solvent	**Calorimetry**	**Spectrophotometry**	**Light scattering**	**Dyes**	**SANS**
benzene	0.86 (36)	-	2.7 (37)	-	-
cyclohexane	-	-	1.2-1.3 (38)	1.8-0.2 (38)	0.225 (38)
isooctane	0.84 (36)	1.1 (36)	-	-	-

As illustrated in Table 2-2, there is a considerable range in reported CMCs. This wide range may be due to uncertainties of the different measuring methods used with nonpolar solvents. Additionally, contamination by dissolution of water from the atmosphere may also account for such variability. The influence of water on reverse micelles is described in section 2.3.4.

2.3.4. AOT/water/isooctane microemulsions

As mentioned previously, water in oil microemulsions (w/o microemulsions) are defined as reverse micelles of surfactants in organic solvents which contain solubilized water in their cores. The head groups of the surfactant molecules interact with water and their hydrocarbon tails interact with the organic solvent. The water solubilized inside the reverse micelles exhibits different properties depending on the water-to-surfactant molar ratio. The molar ratio, noted w_o= [water] / [AOT], is a measure of the number of surfactant molecules per reverse micelles, and gives information about the size and the structure of the aggregates.

Moran *et al.* studied the effect of the molar ratio on the water properties inside a reverse micelle for AOT systems (39). Frequency variations resulting from these conformational changes were

observed and three regimes were determined to qualify the state of water inside the micellar structure.

- At low molar ratio of 3 or less, the sulfonate head-group of AOT interacts strongly with the first three molecules of water, resulting in a decrease of the symmetric sulfonate stretching frequency, from 1064 cm^{-1} to 1052 cm^{-1}.
- For values of w_o ranging from 5 to 11 ($5 \leq w_o \leq 11$), water molecules still interact with the hydrated polar head group SO_3^- by forming hydrogen bonds but frequency shifts are less noticeable. In both cases, the confined water inside these micellar aggregates has different properties from the bulk water.
- At higher values of w_o ($w_o \geq 12$), the amount of solubilized water inside the pool increases, resulting in water bulk-like properties and marking the formation of w/o microemulsions. The frequency of the SO_3^- symmetric vibration, however, stays constant above that number. These structures are qualified as large micelles and can solubilize an important amount of water. Maitra and Kumarjain also noticed that an increase in w_o results in conformational changes of the hydrocarbon chains (34). In dry micellar system, which does not contain any water, the hydrocarbon tails mainly adopt an all-trans conformation. In w/o microemulsions, they are likely to be found in a gauche conformation.

Kawai *et al.* (40) also found that the size of AOT micellar aggregates in w/o microemulsions changes until a critical concentration. A "critical concentration for the formation of swollen micelles or w/o microemulsions" was defined and corresponds to the minimal concentration of AOT at which the micellar weight of the aggregates becomes constant. Beyond this concentration, the size of the reverse micellar aggregates stays constant but the number of aggregates continues to increase. This allows for additional water to be solubilized. This physical phenomenon results in a sharp increase of the maximum amount of solubilized water with the concentration of the surfactant. Raman spectroscopic studies on water/AOT /hydrocarbon solvent showed that the symmetric sulfonate stretching mode of AOT at 1063 cm^{-1} is shifted towards lower frequency as the value of w_o increases (39). Similar trends were also observed in the IR spectra (41), (42).

2.4.Associative systems: Example of asphaltenes

2.4.1. Definition

As described earlier, bitumen and VR can be fractionated through the addition of an aliphatic hydrocarbon solvent such as heptane or pentane. Such procedure results in the precipitation of asphaltenes. These compounds are defined as a solubility class that is n-heptane/n-pentane/n-hexane-insoluble and toluene-soluble. Asphaltenes are the heaviest fraction of the crude oil with an estimated molar mass varying from 700 g/mol to 10,000 g/mol depending on the experimental conditions and the solvent used (43), (44). Recent studies showed that asphaltenes have a low molecular weight, around 750-1000 g/mol (45).

The analysis of asphaltenes is a difficult task because of their complex nature. Asphaltenes are composed of thousands molecules and contain different chemical groups such as thiophene, sulfide, porphyrin, pyrrole. Additionally, metallo-organic complexes are commonly found in asphaltenes. They are called porphyrins and contain metals such as nickel, vanadium or iron that are attached to organic molecules. The proportion of these functional groups depends on the origin of the crude oil, which explains why asphaltenes from different sources exhibit different chemical and physical behaviours. Secondly, the separation of asphaltenes into individual components is an unachievable task and no asphaltene molecule has been isolated so far (44). The structure of asphaltenes has, however, been widely studied and is still a subject under debate. Two structural models were proposed to describe the geometrical arrangement of asphaltenes:

- The island model or continental model consists in one central condensed aromatic region per asphaltene molecule with attached alkyl groups (46). Figure 2-10 gives an example of typical continental arrangements, with an aromatic core constituted of six to ten aromatic rings and peripheral alkyl chains constituted of three to nine carbon atoms.

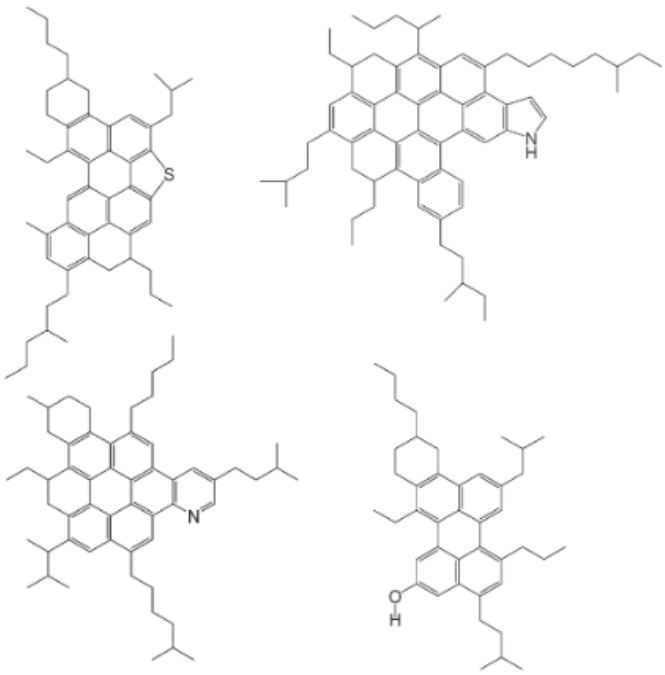

Figure 2-10: Molecular structure proposed by Mullins in 2010 (47)

- The archipelago model is characterized by multiple smaller aromatic cores, which are composed of four to eight benzene rings on average, and are interconnected by alkyl and/or thioether bridges. The paraffinic and iso-paraffinic natures of these bridges were demonstrated by thermal cracking studies (48), (49). Figure 2-11 illustrates a typical structure of archipelago asphaltenes.

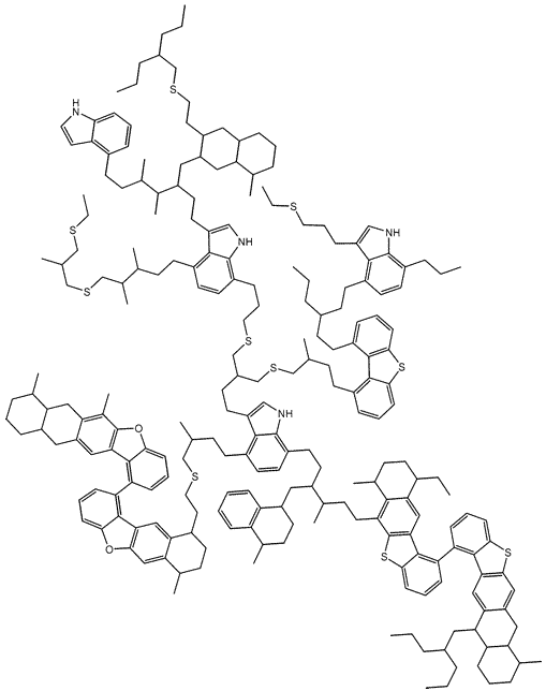

Figure 2-11: Archipelago model for asphaltenes suggested by Sheremata *et al.* (50)

As mentioned in the introduction, asphaltenes are generally undesirable compounds in crude oil, as they tend to aggregate and precipitate. Self-association of asphaltenes results in sedimentation deposits inside reactors and pipelines, massive shut downs and heavy economic impacts.

2.4.2. Aggregation of asphaltene in organic solvent

2.4.2.1. Concept of asphaltenes aggregation

Before the 1990s, the colloidal model was extensively applied to asphaltenes in order to describe their structures and understand their tendency to self-associate in oil (51), (52), (7), (8), (43) (6). This concept was later discarded and a step-wise aggregation model to describe asphaltene association is now widely accepted. Some reasons for such a change are listed below:

- Asphaltenes are highly heterogeneous compounds and unlike surfactants, they would not self-associate in a narrow range of concentrations. The aggregation process of thousands of asphaltene molecules, however, takes place over a wide range of concentration (53).
- The presence of water influences asphaltene association (44). Asphaltenes from oil sands are intimately associated with water as crude oil coexists with connate water in underground reservoirs. Furthermore, extraction and production of heavy oils require

the use of water. Solubilisation and calorimetric studies were used to demonstrate that traces of water (as low as 0.01%) were enough to induce and affect the formation of aggregates in toluene (44). No discontinuity in physical parameters and therefore no CMC-like behaviour of asphaltenes were observed in a water-free environment. This observation suggests that the formation of structures similar to reverse micelles are only possible in the presence of water. Due to the abundance of water in the atmosphere and in the oil, it is likely to contaminate solvents. Unless precautionary measures are taken to rigorously dry the solvents, water contamination probably occurred in previous experiments described in the literature, thus accounting for the observation of a "CMC". The aggregation of asphaltenes around microdroplets of water is favoured by the presence of oxygenated groups such as carboxylic acids, phenols and other polar groups such as sulfoxydes, which interact through hydrogen bonding with molecules of water. The same study showed that the solubility of asphaltenes decreases with the amount of water present, meaning that there is substantial interactions between water and asphaltenes.

- Asphaltenes have a more diverse chemical and structural configuration than surfactants (54). They are one of the most complex structures in crude oil, composed of aromatic areas attached to each other by alkyl bridges and do not have a distinct hydrophilic polar head group and hydrophobic hydrocarbon part like surfactants. The estimated overall polar moment arising in asphaltenes is not as high as in surfactants (55), meaning that the driving mechanism of asphaltene aggregation does not rely on the same combination of intermolecular forces as micellization does.
- Another study by Andersen used isothermal calorimetry titration (ICT) to study the dissociation process of concentrated solutions of surfactants, dyes and asphaltenes (53). The study showed that the dissociation process of asphaltenes is more similar to that of dyes than it is to surfactants.

Considering the nature of asphaltenes, the influence of water in the aggregation process and their similarity with dyes, the concept of micellization is not an accurate description of the self-association process of asphaltenes. Therefore, the term "critical micelle concentration" should not be used to describe asphaltene association, as these entities are not likely to form normal or reverse micellar structures. A step-wise model is more adapted to describe the aggregation of asphaltenes in apolar media because of the complexity of the intermolecular forces and the undeniable presence of water in crude oil. Previous reports of asphaltene CMCs in apolar media are most likely presenting aggregation phenomena rather than micellization. It is, therefore,

relevant to present the values of CMC reported in the literature. Table 2-3 reports some values of CMC obtained by different studies.

Table 2-3: CMC of asphaltenes in different solvents.

references	asphaltene	CMC (g/L)	solvent	method
Andersen and Birdy (7)	C7I	3.24	toluene	Calorimetry
		4.49	quinoline	
		0.6	CCL_4	
Andersen and Christensen (8)	Boscan	2.6	toluene	Calorimetry
	VBH6	4.5	toluene	
Sheu *et al.* (52)	C7I*	0.25	pyridine	Surface Tension
Loh *et al.* (6)	C5I*	15.4	toluene	Surface Tension
	C5I	9	nitrobenzene	Surface Tension
	C5I	12.1	Pyridine	Surface Tension
	C7I	6.5	toluene	Surface Tension
	C7I	6.1	nitrobenzene	Surface Tension

* C5I are pentane insoluble asphaltenes and C7I are the heptane insoluble asphaltenes

Section 2.4.2.2 gives an overview of the forces involved in the aggregation mechanism of asphaltenes in organic media.

2.4.2.2. Interactions driving the association of asphaltenes

In the case of surfactants, the driving force of micellization is the hydrophobic force between the polar head-groups and the apolar solvent or between the lipophilic tails and the aqueous environment. Aggregation of asphaltenes in organic solvents is more complex and driven by a combination of intermolecular forces. Murgich studied the predominant forces involved in the self-association of asphaltenes in a condensed phase found in crude oil (55). The intermolecular forces involved in the formation of aggregates are a combination of Van der Waals forces, intermolecular charge transfers, coulombic interactions, repulsion and induction (55), (56).

In both the continental and archipelago models, the Coulombic interactions are present. Asphaltenes are considered to be the most polar fraction of crude oils, due to their high heteroatom content. Opposite charges scattered across asphaltene molecules result in

attractions between molecules, defined as the Coulomb force. At intermolecular distance of greater than 10 Å, these interactions are dominant.

At shorter distance, other forces become more significant. The nature of these interactions varies from the continental model to the archipelago model.

- In the continental model, the polarizable aromatic cores (PAH) are the main sites of intermolecular interactions (47), (57). London dispersion (induced dipole-induced dipole) and Keesom forces (dipole- induced dipole) lead to anisotropic attractions between Pi electrons (π electrons) and, in a more general way, aromatic sheets. Stacking of aromatics layers, as illustrated in Figure 2-12, is dependent on the size of the polyaromatic region and the attraction becomes greater as the aromatic area gets bigger (58).

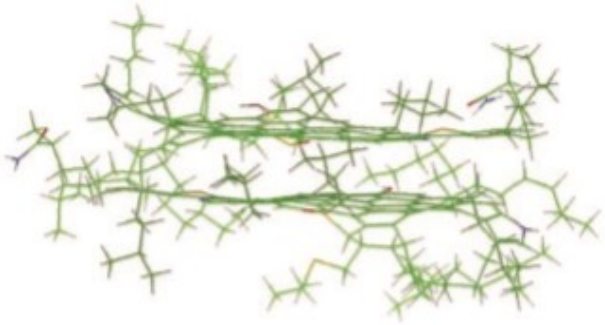

Figure 2-12: In the continental model, stacking of aromatic sheets is an important step of asphaltene self-association, resulting in the formation of primary aggregates (59).

The growth of these aggregates is, however, limited by the presence of steric hindrance and repulsive interactions between substituted alkyl groups (57). Addition of supplementary asphaltene molecules to large aggregates gets more difficult because of the increasing number of alkyl chains attached to the core structure. Asphaltenes that could not approach existing aggregates will nucleate new aggregates with other surrounding molecules.

Stacking of polyaromatic sheets is the primary driving force of the aggregation mechanism, which leads to the formation of structures with the most stable energetic configuration (58). Hydrogen bonding, interactions between functional groups and acido-basic forces are believed to play a secondary role in asphaltene aggregation (60).

- In the archipelago model, interaction forces are more diversified and complex. Aromatic cores are still attracted to each other and can stack through ring-ring interactions. These effects are, however, less important when compared to their presence in the continental model. Other forces such as bridging and hydrogen bonding (59), which are not as predominant in the continental model, become driving forces as well. Murgich *et al.* suggested that the stacking of aromatic regions might leave empty molecular spaces, which are easily filled by small molecules such as water. The ability of water to form H-bonds with basic and acid sites in asphaltenes such as pyrroles, carbonyls, hydroxyls or sulfoxides was verified and appeared to contribute largely to the aggregation process (54). If all the empty spaces in between asphaltene molecules are filled and if all the potential sites for hydrogen bonding are interacting with water molecules, hydrogen bonding might actually be stronger than the other Van Der Waals forces involved in the aggregation process. Water bridges between asphaltene molecules are also observed during the formation of trimer or tetramers (54). The same study also suggested that most of the hydrogen bonds found in asphaltene aggregates occur between molecules of water and atoms of nitrogen. The evidence of hydrogen bonds was also investigated by Merino-Garcia and Andersen who used isothermal titration calorimetry (ITC) to study the behaviour of raw and methylated asphaltenes in dried toluene (61). It was observed that dissociation is made easier when hydrogen bonds are not present in the aggregates, showing that hydrogen bonding definitely influences the association process.

  Interactions in the archipelago model are a combination of stacking, bridging, hydrogen bonding and acid-base interactions (59). Figure 2-13 is an illustration of the different types of interactions which are present in the archipelago configuration.

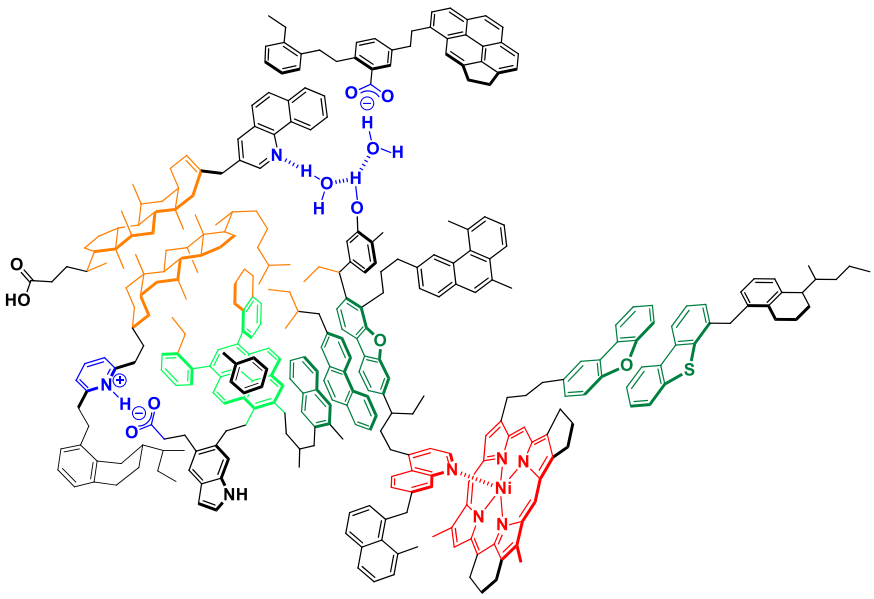

Figure 2-13: Representation of different interactions between archipelago asphaltenes. Acid-base interactions and hydrogen bonding are represented in blue; metal complexes are represented in red; a hydrophobic region is represented in orange and stacking of aromatic sheets is represented in light and dark green (62)

As the macroscopic point of view, the proportion of attractive to repulsive forces gives an understanding of asphaltene solubility in organic solvent. If the attractive interactions were too dominant, asphaltenes would be tightly associated and would not dissolve easily in toluene and if the attractions between asphaltenes were not high enough, they would be loosely associated and would not precipitate by addition of n-alkanes.

2.4.2.3. Critical aggregation concentration of asphaltenes

Molecular-level associations of asphaltenes in apolar media were observed by a variety of techniques and characterized by different mechanisms. Two types of aggregation states, occurring at different concentrations, are reported in the literature. There is, however, still uncertainty concerning the attribution and meaning of these two sets of states.

A low concentration range for the onset of aggregation is reported between 1 mg/L and 150 mg/L. These concentrations were attributed to the early stage of asphaltene self-association, leading to the formation of primary aggregates, often called nanoaggregates. Aggregation observed in the low concentration range is defined as the critical nanoaggregate concentration (CNAC). A different interpretation was proposed by Mullins (47), suggesting that the CNAC measured at low concentration (1-150 mg/L) corresponds to the moment where nanoaggregates stop growing, due to steric hindrance. In this concept, asphaltenes are always associated in toluene, so that no molecular asphaltene exists in such solvent.

Table 2-4 illustrates the variety of different experimental methods and interpretations to characterize asphaltene aggregation in toluene. Due to time constraints, the different experiments are not described in details. The reader is encouraged to read the literature for more specific information.

Table 2-4: Critical concentrations reported in the literature.

asphaltenes	first stage of aggregation	second stage of aggregation	technique	mechanisms and interpretations
Cerro Negro, Hamaca, Furrial asphaltenes (11)	~50 mg/L	n/a	Thermal lens spectroscopy	The formation of solvent-asphaltene complexes at the CNAC decreases the diffusivity of the solvent
Furrial asphaltenes (10)	50 mg/L	n/a	Absorbance/fluorescence spectroscopy	The formation of asphaltene aggregates at the CNAC results in light scattering and quench fluorescence
Hamaca asphaltenes (10)	75 mg/L	n/a	Absorbance/fluorescence spectroscopy	
Asphaltenes from Kuwait (UG8) and California (Cal) (46)	≥60 mg/L	n/a	*Fluorescence spectroscopy*	
Asphaltenes from Tartasan crude oil, Russia	5-15 mg/L	90 mg/L	Near UV/visible absorption spectroscopy	Formation of dimers at 5-15mg/L and dimer pairs at 90 mg/L
Tartasan crude oil, Russia (63)	1-2 mg/L up to 100 mg/L	150-200 mg/L	Light scattering, NMR, dynamic viscosity	
BG5 asphaltenes, Kuwait (9)	48 mg/L		Ultrasonic spectroscopy	The formation of large complexes introduces a modification of elastic properties. Dimer and trimers might be present before the CNAC.
UG8 asphaltenes, Kuwait (9)	164 mg/L	n/a	Ultrasonic spectroscopy	

The CNAC varies from 1 mg/L to 170 mg/L depending on the technique used as well as the nature of the asphaltenes. One study, which did not separate asphaltenes from the rest of the crude oil, leaded to a wider range of values of the CNAC (63). Such results can be explained by the fact that other entities in crude oil influence and participate in asphaltene aggregation. The nature and the role of these connectors is, however, not discussed in this thesis.

A higher set of concentrations in the range 1-10 g/L is also reported in the literature, depending on the solvent and the method used. These concentrations represent the second stage of association, where nanoaggregates coagulate to form clusters and eventually flocs (60). Sharp changes in physical properties, which previously attributed to a CMC, are now identified as the transition between smaller aggregates into bigger clusters. These values, known as CAC, are comparable to the previous CMC values reported in Table 2-3. As an example, a CAC of 3.1 g/L and 3 g/L were reported for C7 and A1 asphaltenes in toluene respectively, both extracted from the Rangely crude oil located in Colorado (64). Additionally, Andersen reported values of 5.7 g/L for KU asphaltenes, 3.4 g/L for KVB asphaltenes and 6.4 g/L for OMV asphaltenes in toluene with 0.01 % of water (44).

2.4.2.4. Example: model of asphaltene aggregation in the continental model

Table 2-5 summarizes the historical evolution of aggregation concentrations proposed by the scientific community during the last ten years (47).

Table 2-5: Evolution of the scientific knowledge about asphaltene aggregation during the last ten years.

Concentrations	Values in 1998	Values in 2009
Concentration at which nanoaggregates start forming (CNAC)	50 mg/L to 5 g/L	50 mg/L to 150 mg/L
Concentration at which bigger clusters are forming	unknown	2 g/L to 5 g/L

As a summary of the previous studies, the aggregation process is mainly composed of two steps, which are illustrated in Figure 2-14. In the first step, primary aggregates composed of three to six asphaltene molecules in average, with an estimated size of 3 nm, are formed at rather low

concentrations, due to the high binding energy between polyaromatic sheets. The formation of such structures is characterized by the CNAC.

The second step of asphaltene aggregation corresponds to the association of nanoaggregates into approximately 8 nm clusters, containing eight to ten asphaltene molecules at the most (45), (47). This second step occurs at much higher concentrations as it less energetic than the formation of nanoaggregates. Combination of short-range attractive and repulsive forces results in the formation of a three-dimension structure (65).

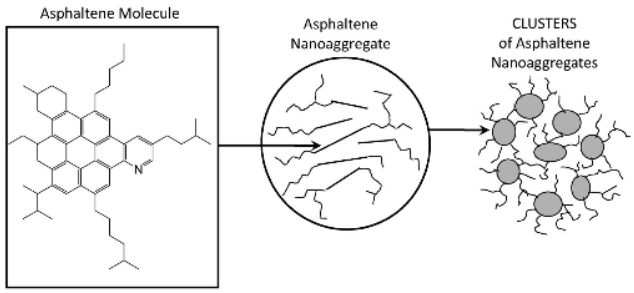

Figure 2-14: Stepwise mechanism for the aggregation of continental asphaltenes (47).

Although the aggregation of asphaltenes is not comparable to micellization, it can be interesting to investigate and compare the influence of both interfacial phenomena on the Raman signal. Additionally, the abundant literature available on surfactant self-association will allow to validate the analytical method developed on these systems with Raman spectroscopy.

3. Instrumentation and Experimental Methodology

3.1. *In-situ* Raman setup design

An *in-situ* Raman setup, which was developed and built by Khalili (12), is used in this project with no major modifications. The next sections give a review of the selected instruments for a basic Raman setup, which includes the following: laser source, sample cell, Raman probe and spectrometer. A brief explanation of how the Raman setup works, from the sample illumination to the collection of the signal, is also provided. Figure 3-1 is an image of the Raman setup with the major components labeled.

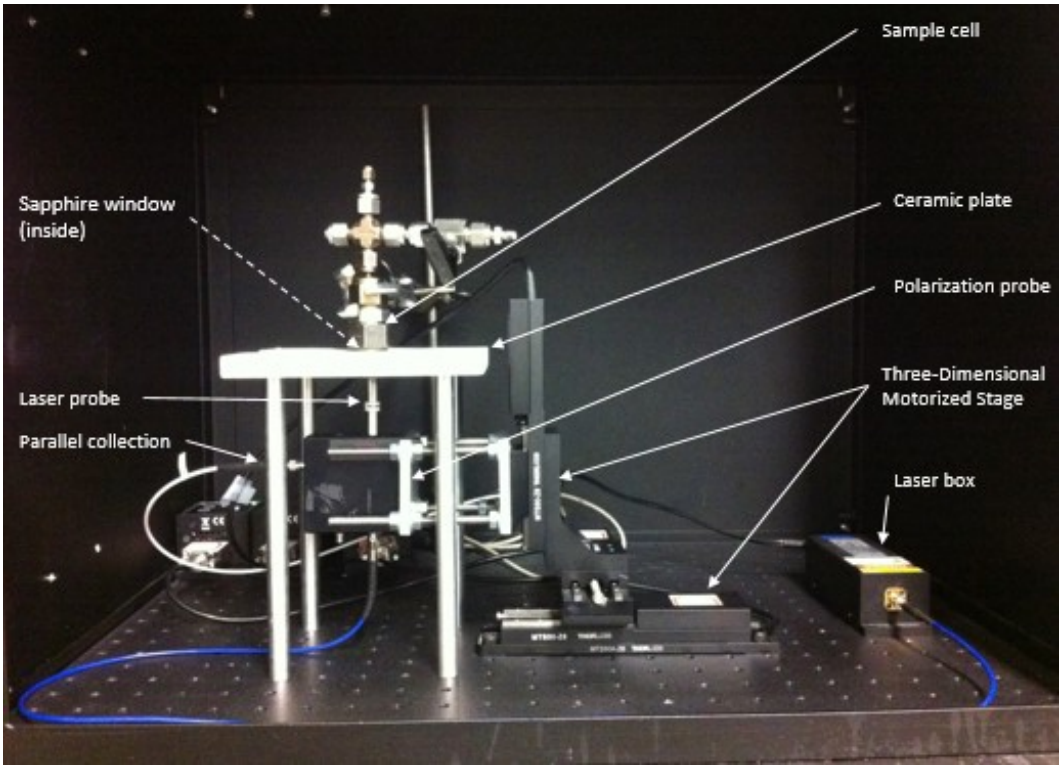

Figure 3-1 : *In-situ* Raman setup.

3.1.1. The laser source

Although Raman spectroscopy is generally independent of the excitation wavelength, it is important to choose a frequency adapted to the sample to be analyzed, the experimental conditions and the results the operator is aiming for. The choice of the laser wavelength was determined based on the following four factors.

- Minimizing the fluorescence produced by polycyclic aromatics or metal-based molecules which can easily overshadows the relatively weak Raman signal.

- Maximizing the intensity of the scattered light, which is inversely proportional to the 4th power of the laser wavelength (66).
- Laser source compatible with the given detectors.
- Minimizing the optical noise.

Photons in the near IR region generally do not have enough energy to excite electrons to the fluorescent levels. Working in this spectral range significantly reduces fluorescence emissions of petroleum compounds (66). Consequently, shorter wavelengths are avoided to decrease the fluorescence phenomenon. As mentioned previously, the intensity of the Raman spectrum decreases as the wavelength of the laser increases. Choosing a large wavelength in the NIR range would result in a very weak signal. A 785 nm laser is, therefore, a good compromise between a 1064 nm or a 632.8 nm laser as it produces a strong enough signal without inducing too much fluorescence. Additionally, the intensity of the Raman spectrum can be improved by using a higher laser power. Consideration of these factors resulted in the selection of a 785 nm diode laser with 500 mW power from RGBLase LLC (12). This type of laser can be fiber-coupled to the rest of the instruments inside the Raman setup.

3.1.2. Sample cell design

The sample cell is mostly comprised of stainless steel Swagelok® parts, with the exception for the base, which is composed of a stainless steel sealing ring, and nut manufactured by Parker®. To allow for *in-situ* Raman spectroscopy, the cell is fitted with a sapphire window, obtained from Meller Optics Inc. The window is made from optical grade sapphire with a 20 mm diameter and 4 mm thickness. Figure 3-2 is a model of the sample cell used in this work. Total volume of the sample cell cavity is measured to be 5.5 mL. The materials and construction were originally selected to allow for high temperature and high-pressure operations at hydroconversion reaction conditions.

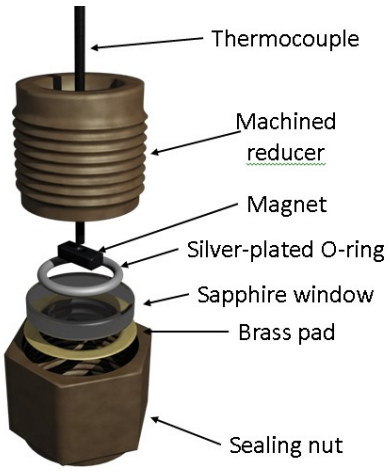

Figure 3-2: Overview of the lower part of the sample cell fitted with a sapphire window at the bottom. Figure courtesy of Cedric Laborde-Boutet (12).

The sapphire window is an excellent candidate for spectroscopic studies as:

- It transmits more than 85% of the incident light when using a 785 nm laser.
- It has a symmetric uniaxial crystal structure which is parallel to the incident light. As such, all the rays propagate at the same rate through the material. These types of crystals are called birefringent retarders because they introduce little phase difference between the incident and transmitted rays (67).
- Sapphire is chemically inert and strong (68).

The sample cell is equipped with a KQXL-type thermocouple from Omega® which had two purposes: Measuring the temperature inside the cell and serving as a shaft for the magnet stirrer. The alnico magnet block from Dura Magnetics Inc. (9.5*4*3 mm) is customized with a 2 mm hole in order to be inserted around the thermocouple inside the sample cell. It is coupled to a larger external magnet, which is attached to a motor with adjustable speeds. The rotational speed of the small internal magnet inside the sample cell can be controlled by the motor *via* the rotation of the external magnet. In order to prevent any leakage in the sample cell, an elastomer sealing ring is inserted in between the reducer and the sapphire window (i.e. Figure 3-2).

3.1.3. Illumination process

The sample illumination system is an arrangement of fiber optical cables, lenses and mirrors which perform three functions: Transporting the incident light into the sample, collecting and fragmenting the backscattered light into particular polarization states and finally delivering the

polarized beam to the spectrometer. In order to build the illumination and collection system, four different elements are present inside the Raman setup:

- A fiber-coupled polarization probe from InPhotonics Inc. containing a sampling lens through which the laser beam illuminates the sample and into which the backscattered light is collected. Figure 3-3 represents a polarization probe. Three separate channels are attached to the polarization probe: an excitation channel that delivers the laser light polarized parallel to the plain of incident and two others which transmit either the perpendicularly (S-polarized) or parallel (P-polarized) backscattered light from the probe. For the parallel component, the incident beam and the backscattered light are aligned 180 ° from each other while for they form a 90 ° angle in the perpendicular configuration.

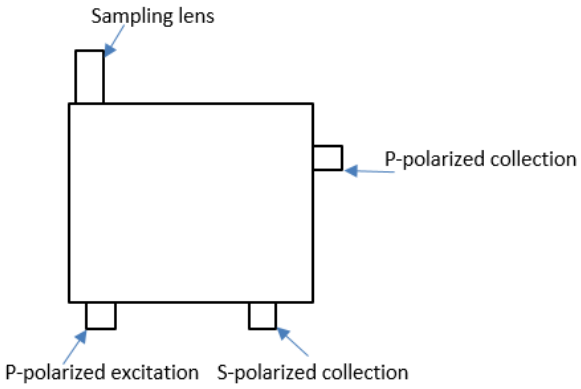

Figure 3-3: Representation of the physical arrangement of the polarization probe

- A 100 µm fiber optic cable which transports the excitation beam from the laser source to the polarization probe and 500 µm cables which collect the backscattered light and deliver it to the spectrometer.
- A three-dimensional motorized stage, model MTS50-Z8, from Thorlabs Inc, which moves the polarization probe in the three Cartesian axis up to 50 mm with 0.29 nm resolution and 0.1 µm minimum displacement. The polarization probe is fixed along the z-axis to control the penetration depth of the laser beam into the sample.
- A ceramic plate with a circular slit placed above the motorized stage. In this project, the bottom of the sample cell was placed perpendicularly on a ceramic plate in a way that the sapphire window faced the circular slit of the plate. In this configuration, the polarization probe was oriented perpendicularly to the window, ensuring a vertical

penetration of the laser beam inside the cell and avoiding absorption of the incident light. The penetration depth is adjustable by changing the position of the polarization probe along the z-axis. The ceramic plate is represented in Figure 3-1 and Figure 3-4.

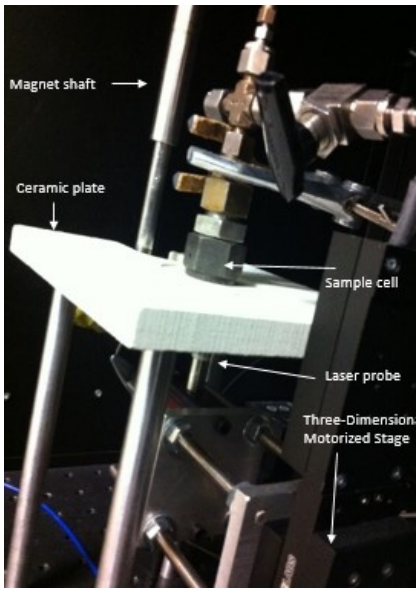

Figure 3-4: *In situ* sample cell and laser probe configuration.

3.1.4. The spectrometer

The scientific grade Raman spectrometer, model QE65 Pro-Raman, from Ocean Optics is a dispersive spectrograph-based device and was selected to study solvent mixtures, micellization, aggregation and microemulsions.

The spectrograph is composed of two apparatuses: First, the light is passed into a spectral analyser composed of a diffraction grating surrounded by two mirrors. One mirror is placed before to direct the light inside the diffraction grating device and the other one is placed after to collect the dispersed light. The second unit of the spectrograph is the detection system, which is the combination of a notch filter and a multichannel detector. Figure 3-5 shows a detailed schematic of the Raman setup.

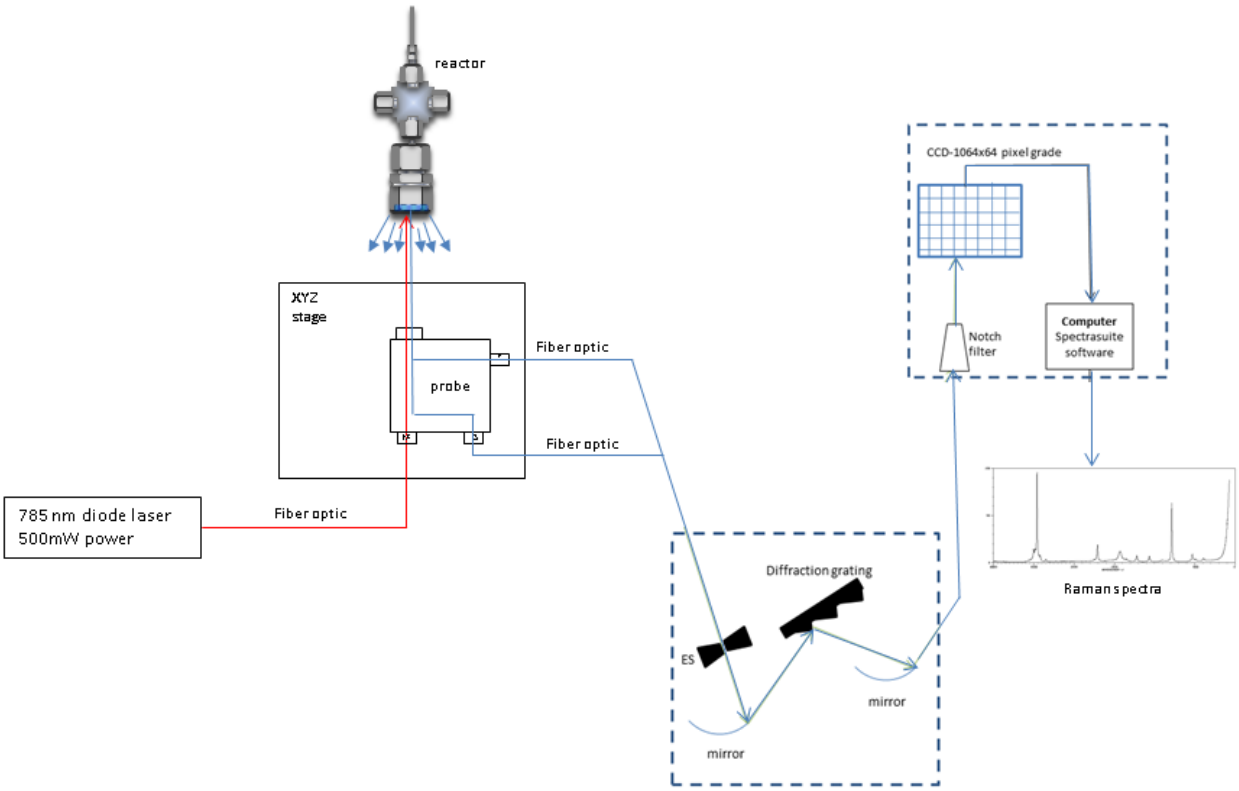

Figure 3-5: Schematic of the Raman setup; ES: entrance slit.

The laser first shines through a cleaning filter, which removes all the undesirable plasma lines and the parasite radiations from the light beam. A set of mirrors and lenses directs the laser light into the sample, which is either contained in a glass cuvette or in the sample cell. The light, which is emitted from the sample, is then collected *via* a sensor and sent to the spectrometer, where a spectral analyser is associated with a filter and a multichannel array detector (CCD) to analyse and collect the Raman scattered light.

The scattered light resulting from the interaction between the sample and the excitation source is directed toward a diffraction grating, model H36, which diffracts the monochromatic beam into individual monochromatic wavelengths. The dispersed light coming from the diffraction grating is then projected onto a two-dimensional CCD detector (charge-coupled device); model S7031-1006 from Hamamatsu. The detector is made of a 1064 x 64 pixel grading system and the photons from the dispersed light beam will contact the photo-sensitive elements (photoactive silicon materials) contained in the grade. The first pixel of the grade interacts with the lowest wavelength, the second will interact with the next wavelength and the process keeps going so that every wavelength of the spectrum interacts with the CCD array. The interactions between

the light and each of the pixels will result in the creation of electrons. The resulting charge is stored and further converted into a digital signal readable by a computer.

This type of detector guarantees low noise and allows for a wide integration time ranging from 8 milliseconds to 15 minutes. A holographic notch filter is associated with the CCD detector to reject the unwanted Rayleigh signal and the non-diffracted scattered light. As such, only the Raman scattered light is processed.

3.2. Vacuum Residue feed and Chemicals

3.2.1. Athabasca Vacuum Residue

Athabasca VR, also noted VR, was the only heavy oil feed used in the study. The asphaltene content of such compounds is reported to vary from 17.3 wt. % to 18.6 wt. % (69), (70).

3.2.2. Chemical reagents

Table 3-1 summarizes the hydrocarbons used in this work.

Table 3-1: cleaning agents, solvents and surfactants used in the project

solvent	manufacture	purity
water	Milli-Q	Double distilled
toluene	Fisher Scientific	99.9 %
acetone	Fisher Scientific	99.7 %
Decahydronaphthalene, mixture of cis+trans[1]	Sigma-Aldrich	99%
pyridine	Sigma-Aldrich	99.9%
hexadecane	Acros Organics	99%
cyclohexane	Fisher Scientific	99.9 %
2,2,4-trimethylpentane[2]	Acros Organics	99.9 %

[1] also referred as decalin
[2] also referred as isooctane

Table 3-2 reports the properties of the two surfactants studied in this project.

Table 3-2: Surfactants used in this project

surfactant	manufacture	purity	physical state
Sodium Dodecyl Sulphate (SDS)	MP Biomedicals	99.5%	white granular powder
Dioctyl Sulfosuccinate Sodium salt (AOT)	Acros Organics	96%	white waxy solid

SDS and AOT were the two anionic surfactants tested in this project. Solution preparation in water using AOT was more difficult relative to SDS, due to their solubility differences. Doubled distilled water was used to prepare aqueous solutions of these surfactants and microemulsions.

Toluene, cyclohexane and isooctane were used as organic solvents to dissolve the AOT wax. Additionally, toluene was used to solvate VR and served as a cleaning agent. Acetone was exclusively used to clean the sample cell, the window and the probe tip.

3.3. Experimental Methodology

3.3.1. Loading and cleaning of the sample cell

The loading procedures used in all experiments were similar: Approximately 2 to 4 mL of each feed solution was poured into the clean sample cell before placing the sealing ring and the sapphire window according to Figure 3-2.

The sample cell and window cleaning procedure was a combination of physical and chemical techniques. Sample cells were always cleaned with sand paper and/or cotton swabs as a mean of mechanical removal. The type of solvents used for cleaning, however, was adapted to suit the nature of the products and the experimental conditions.

- The cell was rinsed with toluene in between each analysis when analysing VR in toluene.
- The cell was first rinsed with distilled water and acetone and then dried with pressured air in all experiments using aqueous solutions of surfactants.
- The cell was only rinsed with acetone before analysing each new sample for the microemulsions experiments.

3.3.2. Preparation of binary and ternary solutions

The binary and ternary solutions were prepared by mixing the chemicals in the same weight proportions. Each chemical represents 50 wt. % for the binary mixture and 33.3 wt. % for the ternary mixture. A total volume of 2 mL was prepared for each solution and poured into the sample cell.

3.3.3. Preparation of micelles and reverse micelles

3.3.3.1. Solutions of SDS and AOT in water

Aqueous stock solutions of SDS and AOT were prepared by dissolving a specific amount of each surfactant in double distilled water and aqueous solutions of chloride sodium respectively.

Solutions with concentrations varying from 0.05 mmol/L to 50 mmol/L were prepared by successive dilutions of the stock solution. The first ten dilutions were prepared by collecting a certain amount of the stock solution with a graduated pipette and diluting the desired amount in distilled water. Equation 3.1 illustrates the relationship between the concentrations and volumes of the stock solution and dilution.

$$F = \frac{C_{stock}}{C_{dilution}} = \frac{V_{dilution}}{V_{stock}} \qquad \text{Eq. 3.1}$$

Where F is the dilution factor, C_{stock} and $C_{dilution}$ are the concentrations of the stock solution and dilution respectively. $V_{dilution}$ and V_{stock} are the volumes of the dilution and stock solution respectively.

As such, knowing the concentrations of the stock solution and dilution, as well as the volume of dilution which is to be prepared, the volume of stock solution needed to obtain can be determined using Equation 3.1. In this project, flasks of 10 mL, 50 mL and 100 mL were used to prepare the dilutions.

As the concentrations of the last two or three dilutions were too low, the equipment available in the laboratory was not adapted to collect small quantities from the stock solution. As such, one of the first ten dilutions previously made was used as a stock solution for the preparation of the most diluted solutions. The volume collected is still defined by Equation 3.1.

As mentioned previously, the addition of electrolytes results in a decrease of the critical micelle concentration. In order to show that the eventual changes observed in the Raman spectra reflect the actual CMC of the surfactant, the influence of salt on SDS solutions was also observed. Different solutions of sodium chloride NaCl in water were prepared prior to dissolving the surfactant. Preparations and dilutions of the stock solutions followed the same procedure as in pure water. The concentrations and amount of surfactants used, as well as the concentrations of the electrolyte in water are resented in Table 3-3.

Table 3-3: Concentrations and quantities of surfactants, solvents and salts used in this project.

surfactant	solvent	observation	stock solution of SDS (mol/L)	volume of stock solution(ml)	quantity in stock solution (g)	number of samples	lowest concentration of SDS (mol/L)	number of observations for each set
SDS	water	1	$3{,}4.10^{-2}$	100	1 g SDS	12	$1{,}7.10^{-4}$	2
		2	5.10^{-2}	100	1.445 g SDS	15	1.10^{-4}	2
SDS	0.02 mol/L NaCl	3	5.10^{-2}	500	1.450 g SDS 0.588 g NaCl	15	5.10^{-5}	3
SDS	0.1 mol/L NaCl	4	5.10^{-2}	500	1.450 g SDS 2.922 g NaCl	15	5.10^{-5}	3
AOT	water	1	2.10^{-2}	100	0.889 g AOT	13	1.10^{-4}	3

3.3.3.2. Solutions of Aerosol OT in cyclohexane

The formation of AOT reverse micelles in organic solvents was investigated in this project. In order to avoid any contamination with water, the solvents and surfactant were dried prior to dissolution. Preparation and storage of the solutions were carried out inside a glove box.

The weighed amount of AOT needed to prepare a 1.10^{-2} mol/L stock solution of 100 mL was 0.445 g. This quantity was dried at 80 °C in a vacuum oven for several hours. The physical aspect of the feed is shown in Figure 3-6 after the drying process. The mass loss was calculated to be only 0.0075 g as the dry sample weighed 0.4375 g. Cyclohexane was dried over spherical microporous zeolites A_3 for 15 to 20 hours. Water removal by zeolites A_3 is a reliable technique which is commonly used for ethanol, air and hydrocarbons. The experimental details are reported in Table 3-4.

Figure 3-6: Dry AOT obtained after being dried in the vacuum oven overnight

The dry solvents and AOT were stored in a glove box and preparations of all solutions were also made inside the chamber in order to avoid any contamination with air and water. The glove box used in this project is a sealed container filled with nitrogen which provides an inert atmosphere. A pair of plastic gloves is attached to the chamber so the products can be manipulated without breaking the atmosphere. Figure 3-7 is a picture of the glove box used in this project.

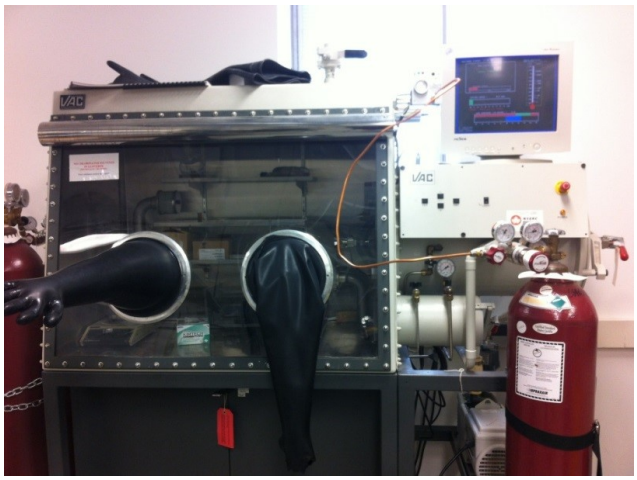

Figure 3-7: Picture of the glove box used in this project. The right glove appeared to have micro holes. A protective door is placed between the right glove and the chamber to prevent any leakage.

3.3.4. AOT/water/isooctane microemulsion

The preparation of water in oil microemulsions also required the use of water-free solvents and surfactants. The drying process of AOT was different from the one used in section 3.3.3.2. A higher amount of salt was needed in this experiment and the quantities were too high to fit inside the glass chamber suited for the vacuum oven. Therefore, another process, presented in Figure 3-8, was used to dry the entire quantity of AOT at once. An air gas flow of 200 mL/min was continuously blown over the wax for 12 to 20 hours. This process removed the water contained inside the sample and progressively dried the sample.

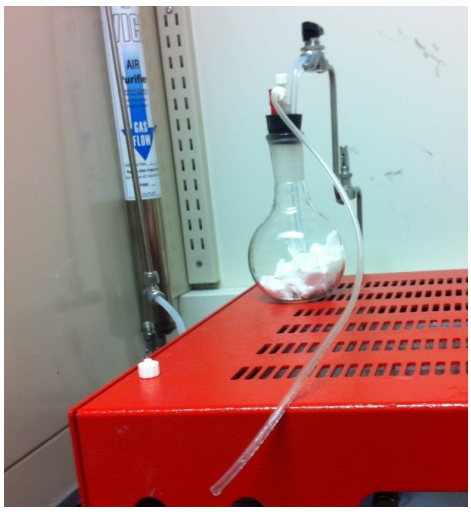

Figure 3-8: Picture of the system used to dry a great quantity of AOT.

Drying of the solvent was achieved according to the same procedure described in section 3.3.3.2. After drying the salt and the solvent, a 0.5 mol/L solution of AOT in isooctane was prepared at 25°C by dissolving 22.3 g of the dry product in the solvent. Milli-Q double distilled water was successively added via a syringe to prepare the water/AOT/isooctane ternary solutions corresponding to a water-to-surfactant molar ratio w_o of 0.1, 3.5, 10, 12, 15, 18, 20, 30 and 40.

Table 3-4 reports the quantity of AOT, the concentration ranges of the dilutions and the number of observations for AOT/cyclohexane solutions and AOT/water/isooctane microemulsions.

Table 3-4: Concentrations and quantities of AOT and solvents used in this project.

solvent	stock solution of AOT(mol/L)	volume of stock solution(mL)	quantity in stock solution (g)	number of samples	lowest concentration of AOT (mol/L)	number of observation dates
Cyclohexane	1.10^{-2}	100	0.4375	11	5.10^{-5}	3
Isooctane/water/AOT	5.10^{-1}	100	22.3	10	5.10^{-1} *	3

*For the microemulsions of water in isooctane/AOT systems, the concentration of AOT in isooctane remained constant throughout the experiment but the amount of water added to the system varied from sample to sample.

3.3.5. Athabasca Vacuum Residue/toluene solution experiments

A stock solution of 0.1 wt. % VR in toluene was prepared and successively diluted to obtain a concentration range from 0.1 wt. % to 0.00005 wt. %. Figure 3-9 shows the different concentrated solutions with the stock solution on the left and the most diluted solution on the right.

Figure 3-9: Picture of the different solutions of VR in toluene analysed in this project.

Approximately 5 mL of each sample was poured into the sample cell previously described in section 3.1.2. Stirring of the mixture was provided by the rotation of a small magnet inside the cell, whose movement is induced by the rotation of a bigger one attached to a motor and located on the outside of the sample cell.

3.3.6. VR/water/toluene microemulsions

The preparation of VR/water/toluene microemulsions was different from that of AOT/water/isooctane microemulsions. As VR and asphaltenes contained water, which is intimately interacting with other functional groups, water removal is a delicate task. As such, only the solvent was dried over Zeolite A_3 and the preparation of microemulsions was carried out under the fume hood. Table 3-5 reports the details of the experiment.

Unlike AOT/water/toluene microemulsions, the molar ratio, w_o, could not be calculated. Only the volumes of water added are presented in Table 3-5.

Table 3-5: Concentrations of VR used for the microemulsions and volumes of water added into the stock solution

stock solution of VR(wt. %)	volume of stock solution(mL)	volume of water added	number of observation dates
0.001	100	V_o=0 to V_o= 1.5 mL	1
0.0025	100	V_o=0 to V_o= 1.5 mL	1
0.005	100	V_o=0 to V_o= 1.5 mL	1

3.3.7. Pre-acquisition procedures

Once the sample cell was filled and positioned perpendicularly on the ceramic plate, three preliminary steps were followed before starting the acquisition. These steps are necessary in order to obtain the finest Raman signal possible.

3.3.7.1. Laser focal point optimization

Probe alignment was configured so that the laser is perpendicular to the sapphire window. This is achieved by using a ceramic plate that positions the sample cell in the correct orientation. Good alignment is necessary in order to avoid absorption of the incident light and weakening of the Raman signal. Distance between the probe tip and the cell however, was adjusted for each experiment. The probe was moved upward until contact was made between the tip and the sapphire window. During this step, a piece of tissue was used to cover the tip in order to prevent damage such as scratches. The tip was then moved 10 to 20 mm below this initial spot, corresponding to where the optimum position range is located. This position was further adjusted upon activation of the laser in order to maximize the intensity of the Raman signal.

3.3.7.2. Acquisition parameters

Integration time, scan per average and boxcar width were fixed before collecting the signal. The amount of exposure time during which the backscattered light interacts with the CCD detector is controlled by the integration time. Exposure times are proportional to the amount of charge accumulated in the detector, and a longer integration time allows for more light to interact with the CCD detector and results in a stronger signal (68). For samples that do not fluoresce, it is usually recommended to choose an integration time which gives a signal close to 75% of the detector limit. For compounds that are unstable and highly fluorescent, it is recommended to select a lower integration time which gives a signal closer to 50 to 60% of the detector limit.

The scan per average is defined as the number of discrete acquisitions, which are averaged in one single acquisition. Increasing the scan per average results in a longer acquisition time but a better signal-to-noise ratio and signal quality.

The boxcar width measures the smoothness of the Raman spectrum. It improves the signal-to-noise ratio but lowers the resolution of the signal. It might be helpful when working with weak Raman signals but some precautions need to be taken as some information can be lost if the boxcar width is set too high.

3.3.7.3. Dark spectra baseline subtraction

The dark spectrum is the signal coming from the pixels accumulated by the CCD detector when no light is interacting with it. The dark spectrum was acquired by focusing the laser beam on a dark surface, or covering the probe by an opaque material. This spectrum served as a baseline and was subtracted from the Raman spectrum before starting the acquisition. The subtraction was usually made after aligning the probe and fixing the acquisition parameters.

With the completion of the probe alignment, selection of the acquisition parameters and determination of the baseline spectra, the system is ready for operation.

3.3.8. Pre-processing spectra method

3.3.8.1. Fluorescence removal

Fluorescence has the tendency to saturate Raman signals and, as a result, masks peaks that should be otherwise apparent. This means that signals generated from fluorescence should be removed prior to analysis. Different algorithms can be implemented to correct the baseline of the signal, leading to fluorescence removal and a better signal-to-noise ratio. The reweighed penalized least squares regression (airPLS) algorithm was chosen as it is easy to tune, fast and reliable (71), (12). The algorithm, adapted from Zhang *et al.*, is presented in the Appendix A (72), (73). This method consists in fitting the baseline only of the peak-free parts of the spectrum and leaves the peak areas without correction. Distinction between the two regions is achieved by using a weight vector of fidelity (73), (72), (74). The degree smoothing for the background fitting can be fixed by changing the value of the smoothing parameter lambda, λ, in the algorithm. Some precautions have to be taken when choosing λ because smoothing the signal too much would result in loss of information and a less accurate signal. Although this algorithm was validated in the previous project (12), the analyses were conducted on both raw and airPLS processed spectra. A value of $\lambda = 10^7$, that was used previously to process spectra collected on the same experimental apparatus, was chosen and used for the correction of most of the Raman spectra collected in this project.

3.3.8.2. Normalisation

Due to the high fluctuations in the signal of fluorescent samples, the intensity scales in the raw Raman spectra of different mixtures containing the same entity can significantly change. In order to compare the spectra of different concentrated solutions of the same chemical, it is important to adjust the scale of each spectrum and make them similar. This can be achieved by normalising the spectra to the same frequency. Usually, the frequency corresponding to the

highest peak common to all the spectra was chosen. The intensity of each spectrum was then divided by the intensity of this particular peak. Once normalized, the intensities of all the spectra are at unity for that designated frequency while the remainder has a frequency below 1.0. Other normalization methods are presented in Annexe B.

3.3.9. Acquisition

Raman spectra of all solutions were collected in triplicate or quadruplet. Table 3-6 represents the experimental conditions for the observation of solvents, mixtures of solvents, and surfactants.

Table 3-6: Experimental conditions for the observations of solvents and mixtures of solvents

solvent	number of observations	number of spectra/sample/obs*	temperature (°C)	acquisition time (sec)	scan/ average	stirring
toluene, cyclohexane, isooctane, binary and ternary mixtures	3	10	25	10	2	no
SDS	4	10-12	25	10	7	no
AOT	3	10-12	25	10	7	no

*Number of spectra/sample/obs. is the number of spectra acquired for each concentration at one specific observation date.

An average spectrum over the 10-12 acquisitions was then calculated for each concentration and each observation date.

The experimental conditions for solutions of VR in toluene are summarized in the Table 3-7.

Table 3-7: Experimental conditions for the observation of different solutions of VR in toluene.

set	number of spectra/sample/set*	age (days)	temperature (°C)	acquisition time (sec)	scan/average	stirring
1	20	0	25	7	1	always
2	20	7	25	7	1	always
3	20	20	30	7	1	Stopped before each acquisition

*Number of spectra/sample/set is the number of spectra acquired for each concentration of VR in toluene during one specific observation date (set)

An average spectrum over the 20 acquisitions was then calculated for each concentration of VR and each set.

4. Results and Discussion

Chapter 4 reports the experimental results and data analysis. The first section, 4.1, presents the Raman spectra of common solvents, accompanied with basic interpretations. The second section, 4.2, deals with intermolecular forces in weakly associating mixtures of hydrocarbons and their impact on the Raman signal. Section 4.3 illustrates examples of strongly associating model compounds such as surfactants and develops analytical tools for the observation of self-association. Section 4.4 gives an overview of VR, which is a complex mixture of strongly associated compounds. Due to the numerous interactions present in this sample and the experimental equipment available for this project, peak assignment and determination of the chemical nature of VR were not conducted. Such samples, however, exhibit surface phenomena, which can be observable through Raman spectroscopy. The same section applies the surfactant model developed in section 4.3 to study the aggregation of asphaltenes in toluene and water/VR/toluene microemulsions.

4.1. Raman spectra of individual common solvents

The experimental setup was validated by measuring the Raman spectra of water and three hydrocarbon solvents: toluene, isooctane and cyclohexane. For Raman spectra collected using backscattering techniques, the amount of solution poured inside the sample cell is not a relevant factor. As such, small quantities of samples were used in this project.

4.1.1. Sapphire window

The sample cell was used for the observation of all samples. In this configuration, the laser shines through a sapphire window prior to interact with the sample. Figure 4-1 shows the Raman spectrum of the sapphire window placed on a ceramic plate.

Figure 4-1: Raman spectrum of the sapphire window. The baseline of the signal can change throughout time.

As illustrated in Figure 4-1, the irregular baseline and weak intensity of the sapphire signal makes the interpretation of the spectrum more difficult. Peaks at 1300, 1185, 760, 424 cm^{-1} are, however, observable. Raman studies of synthetic sapphire shows three characteristic bands at 1150, 724 and 414 cm^{-1} as presented in Figure 4-2 (68), (67). The sapphire window used in this project might not have the same purity as the one in the literature, accounting for such frequency differences.

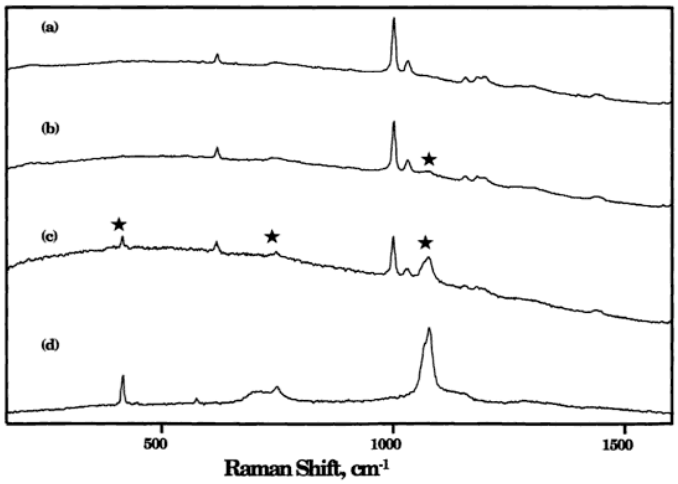

Figure 4-2: Illustration of the influence of the sapphire window on the Raman signal. (a) Raman spectrum of the latex sample; (b) Raman spectrum of the sample focused close to the window; (c) Raman spectrum focused in the sample and (d) Raman spectrum of the sapphire window. The stars represent the sapphire peaks (68).

As observable in Figure 4-2, characteristic signals of the sapphire window are noticeable during the observation of compounds with weak Raman signals. These peaks are assumed to remain stable in frequency and intensity throughout the acquisition of the different samples.

4.1.2. Water

As the Raman signal of water is weak, peaks characteristic of the sapphire glass were also observed. As such, the signal of sapphire was first acquired and then subtracted. Figure 4-3 illustrates the Raman spectrum of double-distilled water after subtraction of the sapphire signal.

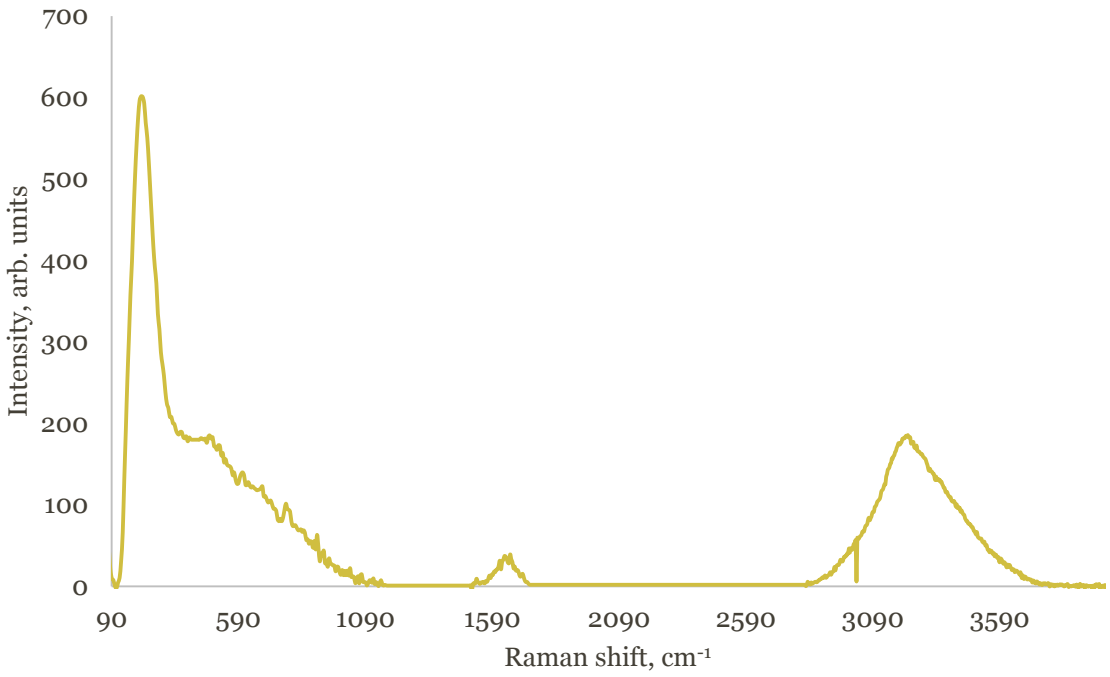

Figure 4-3: Raman spectrum of double distilled water acquired with the experimental setup.

Water is a polar molecule with a weak Raman signal. Although three main peaks at 218 cm^{-1}, 1629 cm^{-1} and 3225 cm^{-1} are observable in Figure 4-3, other bands are reported in the literature. The main Raman active bands of water are listed in Table 4-1.

Table 4-1 : Raman vibrational frequencies of water

vibrational mode	frequency (cm^{-1}) (75)	experimental frequency (cm^{-1})
Hindered translation	200	218
Hindered rotation	470-480	-
O-H bending (w)	1594	-
O-H stretching	1656 ±2	1629
O-H bending	1885	-
O-H stretching	3230	3225
O-H asymmetric stretching	3440	-
O-H sym. stretching	3654	-

* (w) stands for weak

The spectrometer used in this project is not as precise as a scientific grade spectrometer and does not detect all the small intensity peaks. This explains why only three peaks are observed on the experimental Raman signal of water compared to the eight bands observed with a more sensitive device.

Three hydrocarbon solvents were mainly used in this study. The Raman spectra of these solvents were acquired to verify the accuracy of the experimental setup. Prior to acquire the signals, all solvents were transferred into the sample cell. Figure 4-4, Figure 4-5 and Figure 4-6 compare the experimental Raman signals of these solvents with the Raman spectra published in the Spectral Database for Organic Compounds (SDBS). This database was created and is updated by the National Institute of Advanced Industrial Science and Technology in Japan (AIST).

4.1.3. Toluene

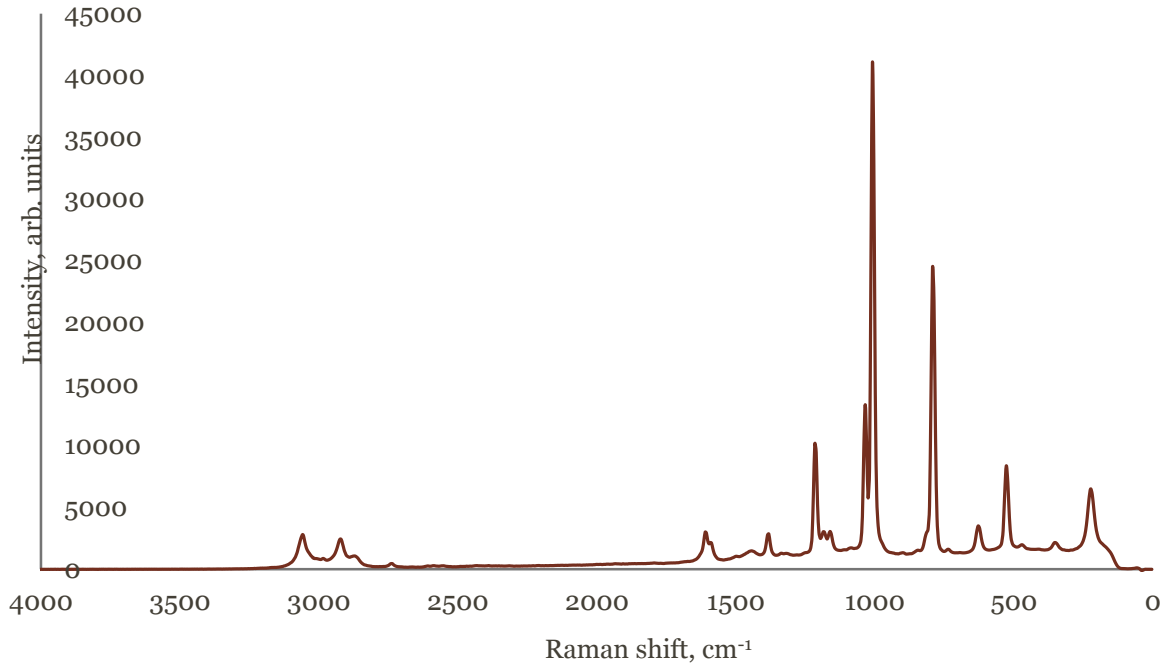

(a)

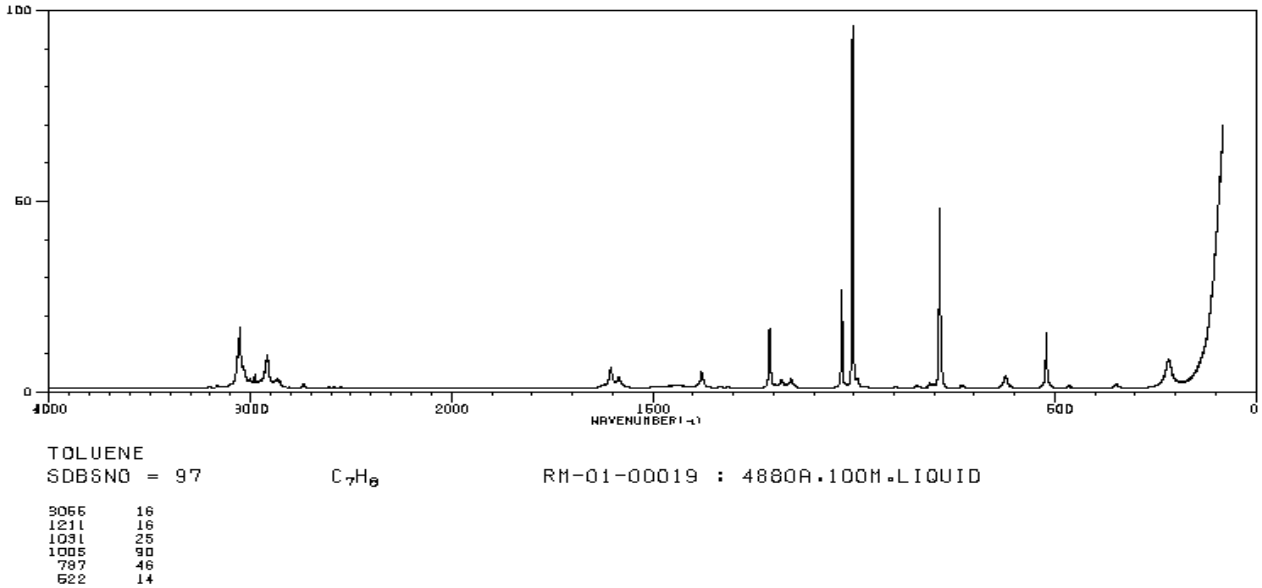

(b)

Figure 4-4: (a) Raman spectrum of toluene acquired with the system; (b) Raman spectrum of toluene published on the SDBS website (76)

4.1.4. Isooctane

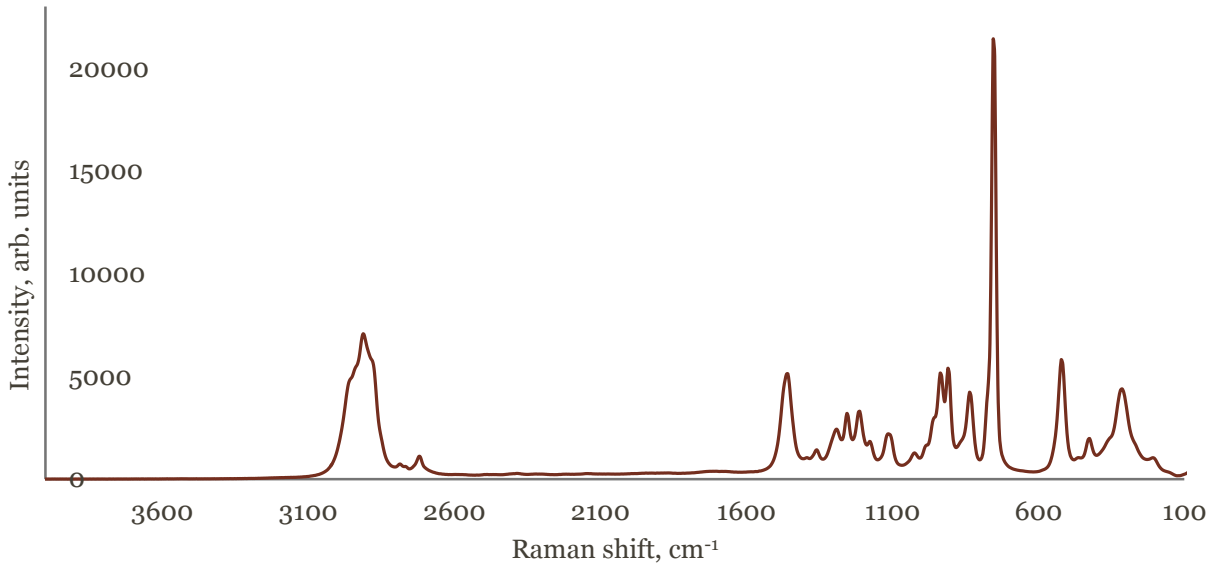

(a)

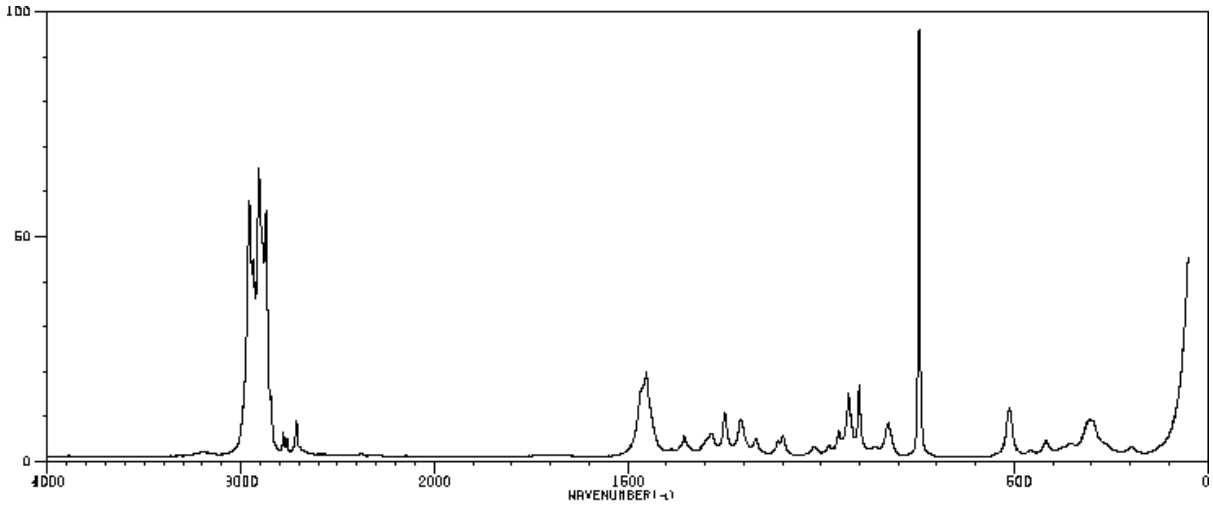

2,2,4-TRIMETHYLPENTANE
SDBSNO = 2353 C_8H_{18} RM-01-00042 : 4880A.150M.LIQUID

2957	56
2937	44
2906	64
2871	55
1463	19
1260	10
930	14
903	16
747	96
614	11

(b)

Figure 4-5: (a) Raman spectrum of isooctane; (b) Raman spectrum of isooctane published on the SDBS website (76)

4.1.5. Cyclohexane

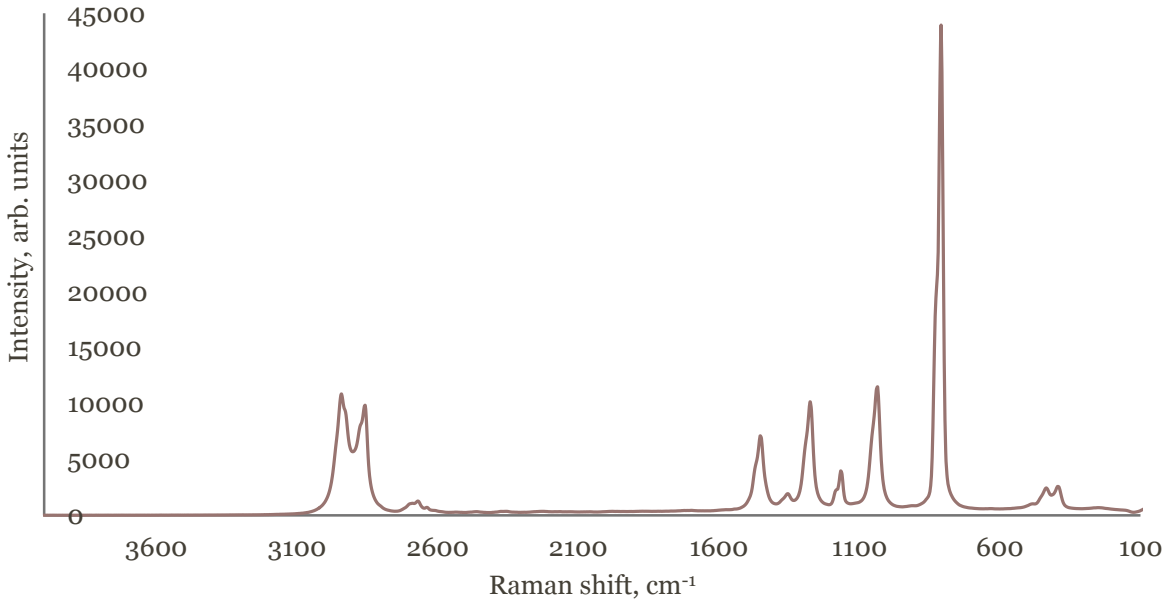

(a)

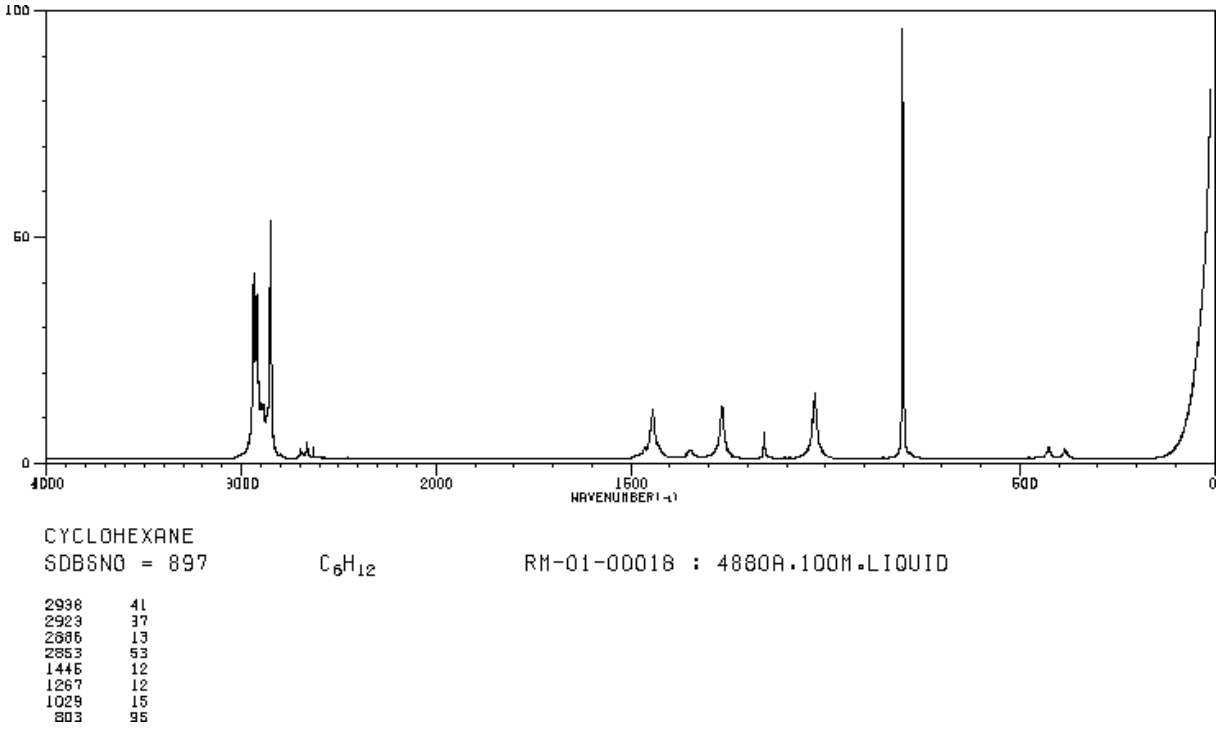

(b)

Figure 4-6: (a) Raman spectrum of cyclohexane; (b) Raman spectrum of cyclohexane published on the SDBS website (76)

As illustrated in Figure 4-4, Figure 4-5 and Figure 4-6, hydrocarbon solvents exhibit strong Raman signals and the characteristic bands of sapphire are not observable in the Raman spectra of such compounds.

Composition of the Raman signal for such basic solvents is a combination of C-C and C-H vibrations. Table 4-2 reports some characteristic molecular vibrations involving carbon and hydrogen atoms.

Table 4-2: Principal vibrational modes of toluene, isooctane, cyclohexane and comparison with the literature.

vibrational mode	toluene		isooctane		cyclohexane	
	(77)	Exp.	(78)	Exp.	(79)	Exp.
C-C stretching	-	-	-	-	426	435
C-C twisting	521-523	527	521	521	521	527
C-C twisting	623	628	-	-	630	634
C-CH_3 stretching	787-784	792	747	754	-	-
C-C stretching	-		-	-	803	809
C-C stretching	1005	1009	-	-	-	-
C-H twisting	1032	1034	-	-	1029-1026	1034
C-CH_3 stretching	1211	1216	1211	1211	-	-
C-H bending/C-C stretching	1154	1151	1154	1160	1157	1166
C-H twisting	-		-	-	1270-1265	1275
CH_3 symmetric twisting/bending	1381	1386	1385-1365	1391	-	-
C-C stretching	1443	1443	1453	1457	1447-1443	1453
C-C stretching	1606	1610	-	-	-	-
CH_2 symmetrical stretching	2853	-	-	-	2853	2857
CH_3 symmetrical stretching	2872	2874	2870	-	-	-
CH_3 stretching	2921-2926	2925	2901	2912	2923	-
Overtone 1465 cm^{-1}	-	-	-	-	2937	2943
C-H stretching	3063	3062	-	-	-	-

As all four examples show, there is a good spectral matching in the range ±9 cm^{-1} between the experimental data and the literature. This validates the collected Raman spectra and demonstrates that the implemented Raman setup produces reliable and trustable results.

The interpretation of the Raman spectra for basic solvents is widely described in the literature. As illustrated in Table 4-2, the frequency of some vibrations such as C-C twisting and methylene stretching vary depending on the surrounding environment. The presence of branching or ring strain can be responsible for such variation, as explained in section 2.1.8. The analysis of the Raman signal can become more delicate when superposition, disappearance and enhancement of certain bands occur, as mentioned in section 2.1.4. When mixing different solvents together, intermolecular forces increase and can modify the Raman signal. Section 4.2 investigates the impact of such forces on the Raman spectra of three weakly associating hydrocarbon systems.

4.2.Raman spectroscopy of hydrocarbon mixtures

When mixing two or more chemicals together, a variety of forces can take place depending on the nature of the compounds. Van der Waals forces are always present in solutions whereas hydrogen bonding or coulombic forces occur when electronegative atoms such as oxygen, nitrogen or ionic species are present in solution. In order to observe changes due to intermolecular forces, the Raman spectra of three weakly associating solutions were acquired and compared with the Raman spectra of each individually compound. This section reports the wavelength shifts for three mixtures and gives interpretations of such results.

4.2.1. Toluene/pyridine system: an associative system

Toluene and pyridine are both mono-aromatic compounds with different polarity properties. When mixed together, these two compounds associate together, in either parallel or T-shape ways. Table 4-3, Figure 4-7, Figure 4-8 and Figure 4-9 compare the Raman signal of the mixture with that of pure compounds.

Table 4-3: Example of same frequency shifts, in cm^{-1}, between pure toluene, pure pyridine and the binary system.

vibrational mode (80), (81)	toluene	pyridine	50 wt. % pyridine/toluene	frequency shift/toluene*	frequency shift/pyridine*
C-H twisting	-	1156	-	-	n/a
C-H twisting	1166	-	-	n/a	-
C-H twisting	1186	-	-	n/a	-
C-CH_3 stretch.	1216	-	1221	5	-
C-N stretch.	-	1226	1221	-	5
C-H bend.	1387	-	1391	4	-
C-C ring stretch.	-	1592 (s)	1592 (m)	-	0
C-C-ring stretch.	1611 (s)	1602 (w)	1611 (m)	0	9

*(s) stands for strong, (m) for medium and (w) for weak : frequency shift/toluene is the frequency difference between the bands in the Raman signals of the mixture and pure toluene. frequency shift/pyridine is the frequency difference between the bands in the Raman signals of the mixture and pure pyridine.

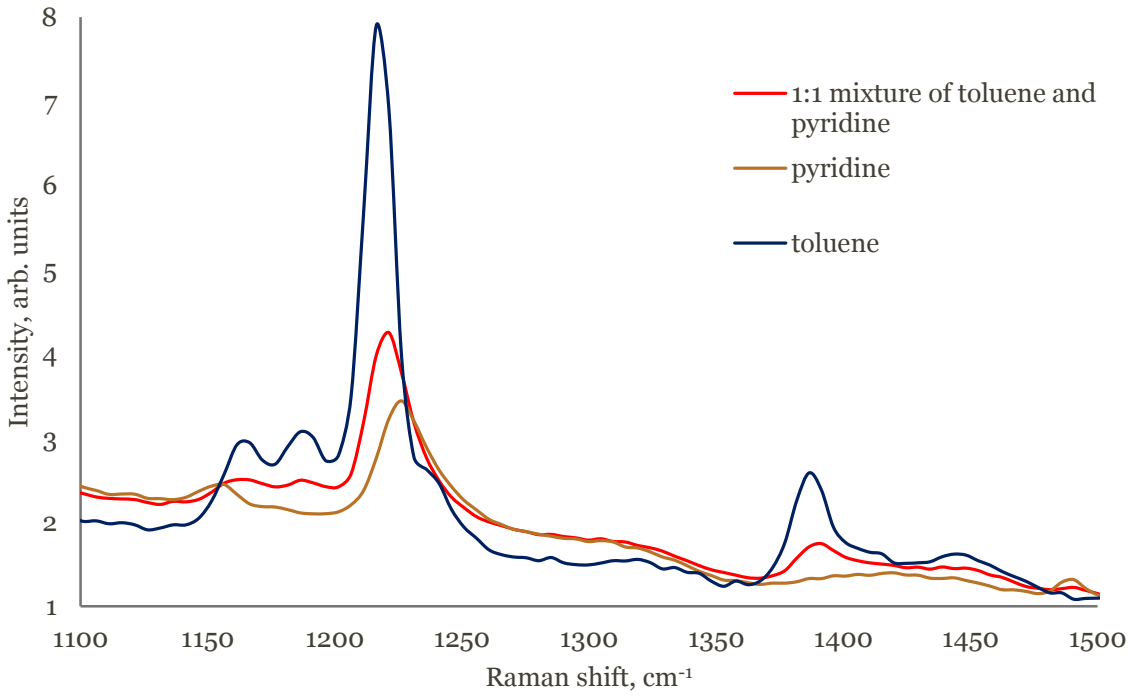

Figure 4-7: Raman spectra of toluene, pyridine and a solution of 50 wt. %/ 50wt. % toluene-pyridine in the 1500-1100 cm^{-1} region

As illustrated in Figure 4-7, the Raman signal of the 1:1 mixture presents a band localised at 1221 cm^{-1}, which is the combination of methyl stretching of toluene and C-N stretching of pyridine. The frequency of this combination band is localised halfway between the frequencies relative to each pure compounds. Additionally, toluene and pyridine peaks located in the 1190-1150 cm^{-1} are not observable in the Raman spectrum of the 1:1 mixture.

An average Raman signal of toluene and pyridine was calculated and compared with the experimental signal. Figure 4-8 illustrates the frequency difference between the theoretical and experimental signals, obtained for the C-N stretching band of pyridine.

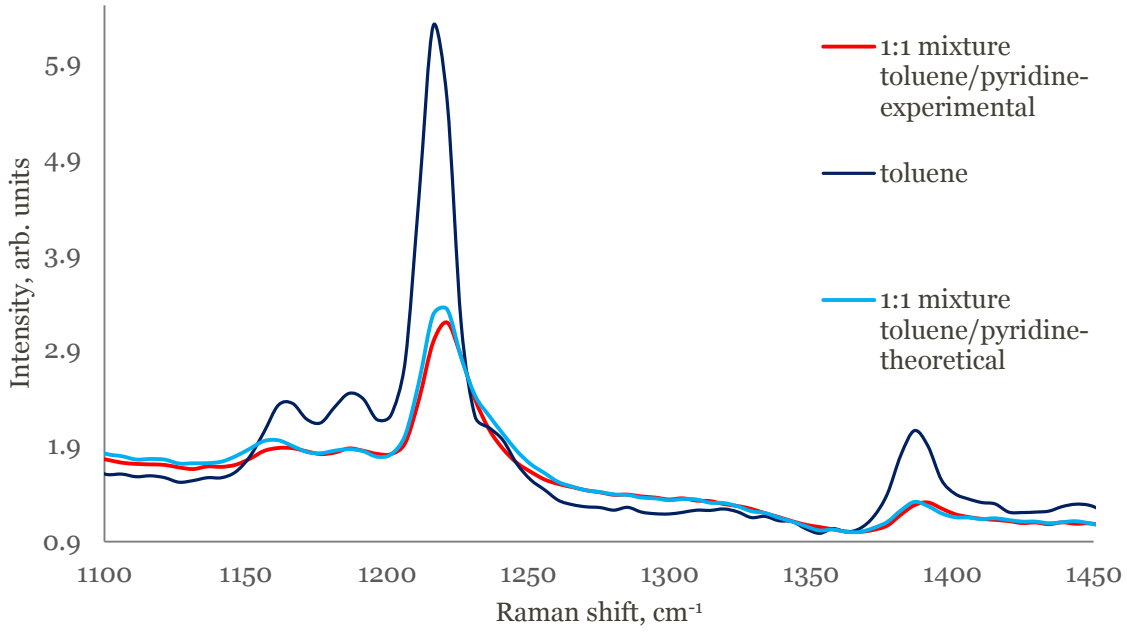

Figure 4-8: Comparison between the experimental spectrum of 1:1 toluene/pyridine, the average spectrum of toluene and pyridine and the Raman signal of pure toluene in the region 1450-1110 cm^{-1}.

The C—N stretching vibration is located at 1226 cm^{-1} in the Raman spectrum of pure pyridine, at 1221 cm^{-1} in the experimental Raman spectrum of the 1:1 binary mixture and at 1216 cm^{-1} in the Raman spectrum of the theoretical 1:1 binary system. Additionally, intensity ratios between the C-N stretching and C-H bending vibrations, calculated from the Raman signals of the mixture, pure toluene and theoretical model, have different values. Table 4-4 reports the values of the three intensity ratios, which all represent the same vibrational study.

Table 4-4: Intensity ratio calculated for pure toluene, experimental 1:1 mixture and theoretical 1:1 mixture.

solution	intensity ratio	value
toluene	I(1386.5)/I(1216)	0.33
1:1 mixture experimental	I(1391)/I(1221)	0.41
1:1 mixture model	I(1386.5)/I(1221)	0.30

The value of the intensity ratio calculated from the experimental Raman signal of the 1:1 mixture has a higher value than the two other ones. Intensity variations, resulting from the interactions between the two solvents, cannot always be predicted and adds another level of complexity to the interpretation of the Raman signal. Figure 4-9 illustrates another example of frequency and intensity shift in the 1800-1350 cm^{-1} region.

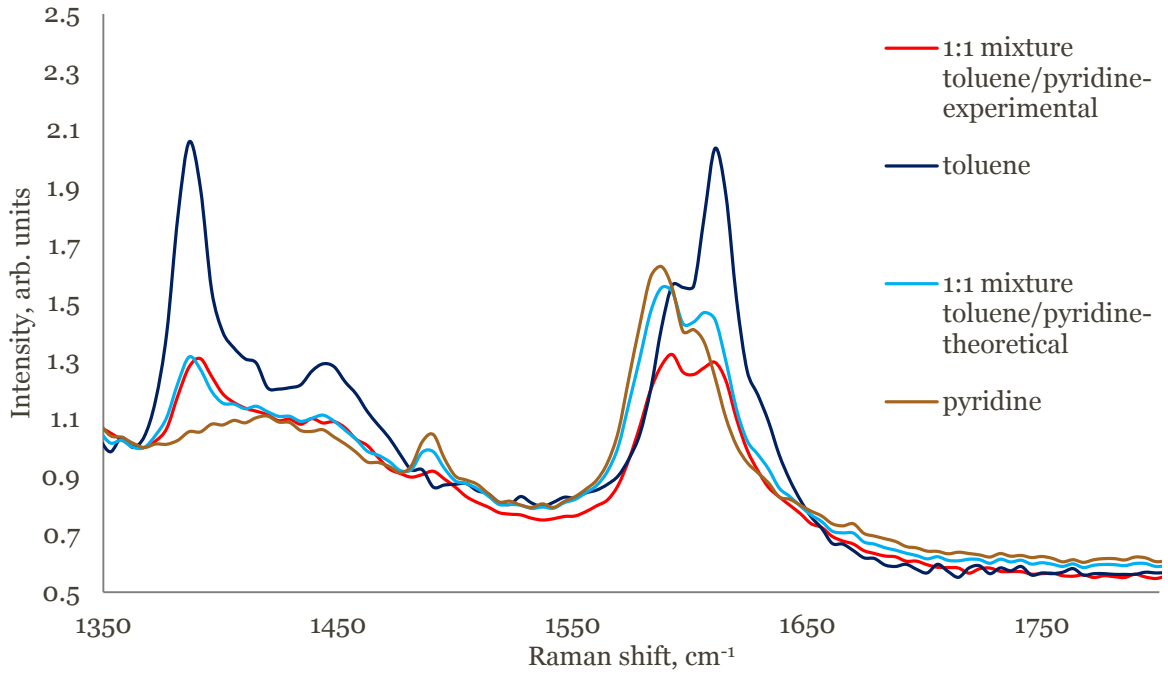

Figure 4-9: Raman spectra of toluene, pyridine, experimental 1:1 toluene/pyridine mixture and theoretical 1:1 toluene/pyridine mixture in the 1900-1400 cm^{-1} region

Pyridine exhibits a strong peak at 1592 cm^{-1} and a shoulder at 1601 cm^{-1}, both corresponding to the aromatic C-C stretching. The Raman signal of toluene shows an inverse trend for the peaks at 1592 cm^{-1} and 1611 cm^{-1}. Both strong peaks are still present in the 1:1 binary mixture but the shoulders are no longer observed. Frequency shifts of almost 10 cm^{-1} between the peaks of pure compounds and the peaks of the experimental 1:1 mixture were observed and are reported in Table 4-3. Additionally, bands at 1490 cm^{-1} and 1448 cm^{-1}, which are present in the Raman

signals of pure compounds and in the Raman spectrum of the theoretical 1:1 toluene/pyridine mixture, are not discernable in the Raman spectrum of the experimental 1:1 mixture.

Frequency and intensity changes might be the result of aromatic stacking. Association of pyridine and toluene molecules affects different vibrations such as methyl stretching, methylene bending and nitrogen bending. Table 4-3 reports 5 cm^{-1} shifts from the signal of pure compounds for such vibrations. Moreover, the nitrogen atom in pyridine creates a dipolar moment, which can have an influence on the surrounding toluene molecules, as described in section 2.1.8. This can be another reason why frequency shifts are observed.

4.2.2. Toluene/decalin system: a dissociative system

Decalin and toluene are two apolar solvents commonly used in the oil industry. The first one is a symmetric cycloalkane and the second one is an aromatic. Unlike pyridine and toluene, they do not associate when mixed together. Table 4-5 and Figure 4-10 illustrate the frequency shifts between the pure chemicals and the binary solution.

Table 4-5 : Examples of frequency shifts between pure toluene, pure decalin and binary mixture

vibrational mode (82), (80)	toluene	decalin	50 wt. % decalin/toluene	frequency shift/toluene	frequency shift/decalin
CH bend.	1186	-	-	n/a	-
CH stretch.	-	2858	2864	-	6
CH_3 stretch.	2926	-	2933	7	-
CH stretch.	-	2936	2933	-	3

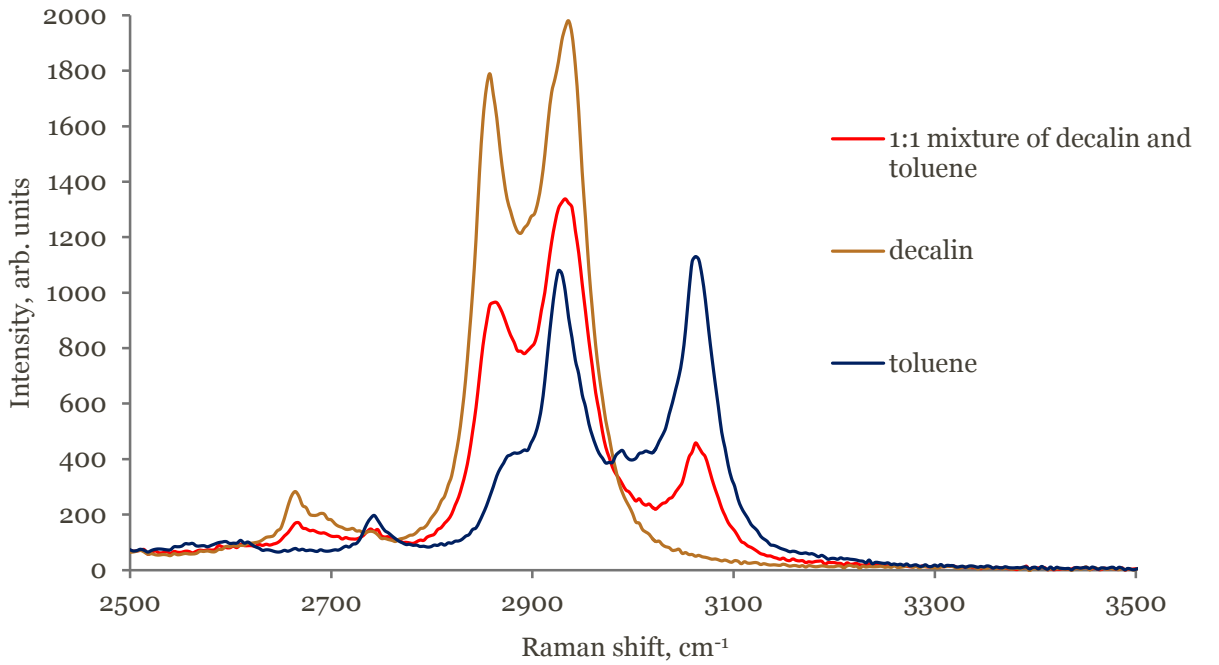

Figure 4-10: Raman spectra of toluene, decalin and the binary mixture in the 3500-2500 cm^{-1} region

In pure toluene, the aromatic molecules associate with each other due to the presence of electrostatic and dispersive forces. Such attractive interactions are weakened when adding decalin. The electrostatic forces are broken down, resulting in the dissociation of toluene aggregates. Such phenomenon leads to frequency shifts, as illustrated in Table 4-5. For example, the frequency of the CH_3 stretching vibration of toluene and C-H stretching vibration of decalin are increased by approximatively 7 cm^{-1} in the mixture.

4.2.3. Toluene/cyclohexane/hexadecane ternary system

Interactions are greater as the number of compounds increases. Band shifts were observed in a weakly associating system composed of one paraffin, one cycloalkane and one aromatic compound. Frequency shifts between the Raman signals of the 1:1:1 ternary mixture and the three pure hydrocarbons are noticeable. Figure 4-11 and Figure 4-12 show two different regions of the Raman spectra where shifts are observable. Table 4-6 reports the main frequency shifts in the high frequency region.

Table 4-6: Frequency shifts reported between the 1:1:1 ternary solution and the pure compounds in the C-H stretching region

vibrational mode (14), (83)	toluene	cyclohexane	hexadecane	1:1:1 mixture	freq. shift
CH_3 stretch.	-	2858	-	2861	3
CH_3 stretch.	2881	-	-	-	n/a
CH_3 stretch.	-	-	2882	-	n/a
CH_3 stretch.	2926	-	-	2929	3
CH_2 stretch.	-	-	2922	2929	7
CH_3 stretch.	-	2943	-	2943	0
CH_2 stretch.	-	-	2939	2943	4
CH stretch.	3062	-	-	3065	3

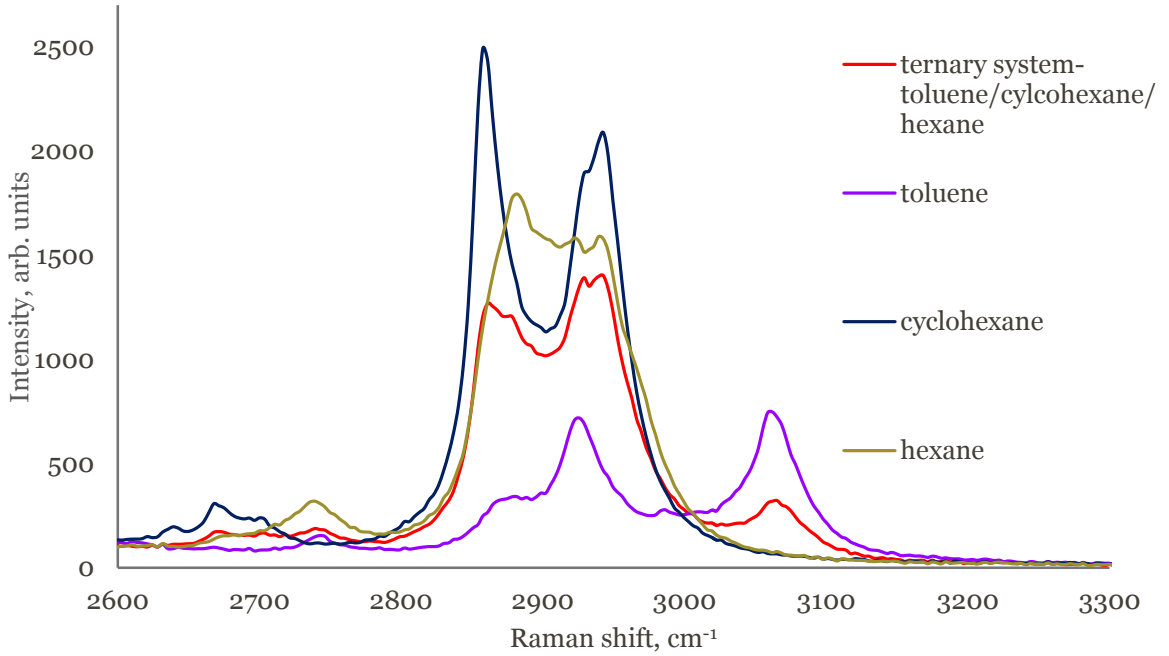

Figure 4-11 : Raman spectra of toluene, cyclohexane, hexadecane and the 1:1:1 ternary mixture in the 3900-2500 cm^{-1} region

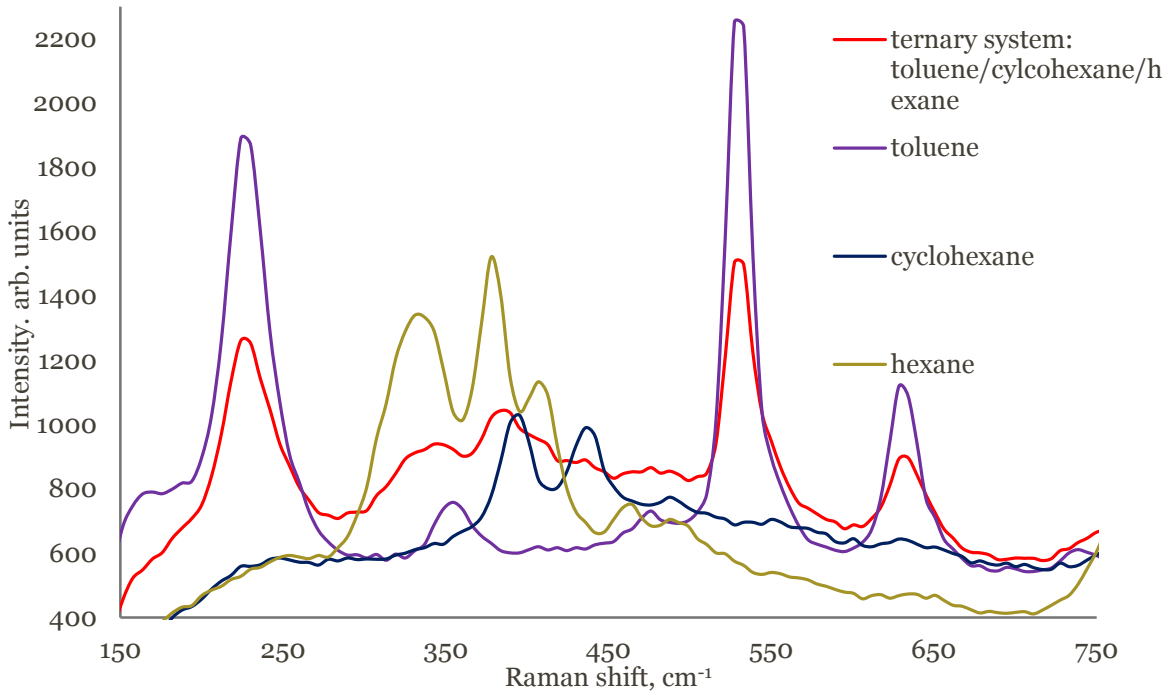

Figure 4-12: Raman spectra of toluene, cyclohexane, hexadecane and the 1:1:1 ternary system in the 750-100 cm^{-1} region

Hexadecane, cyclohexane and toluene account for three different chemical classes: n-alkanes, cycloalkanes and aromatics respectively. Their similar hydrocarbon nature and apolar properties make them miscible. As none of these compounds have a dipolar moment or contain any heteroatoms, interactions such as hydrogen bonding, coulombic forces, as well as Keesom or Debye interactions are unlikely to occur. As mentioned previously, dissociation of toluene dimers occurs when adding non-polar hydrocarbons such as cyclohexane and hexane. This process, along with other weak interactions between the three types of molecules, results in band shifts.

Understanding bands overlapping and frequency shifts for a weakly associating system is not an easy task. Raman signals of mixtures will lose its fine structure as more compounds are added into the system and consequently become more difficult to interpret. Section 4.4 illustrates the challenge when working with petroleum mixtures, which contain thousands of strongly associating compounds. Before investigating the influence of complex associations on the Raman spectra, it is recommended to study well-known associating systems. Section 4.3 illustrates a Raman spectroscopic study of two surfactants.

4.3. Raman spectroscopy of well-defined strongly associating compounds

Spectroscopic studies, carried out on associative and dissociative systems, were presented in section 4.2 and demonstrated the impact of weak molecular associations on intensity and frequency shifts. This section investigates the association behaviour of two anionic surfactants, sodium dodecyl sulphate (SDS) and Dioctyl Sulfosuccinate Sodium salt (AOT) in water and organic solvent respectively. The abundant literature available for the self-association of both surfactants in water will be used as a point of comparison with the experimental results. In section 4.4, these well-defined and strongly associating systems will be used as physical models to investigate the aggregation of VR in toluene.

4.3.1. Aqueous solutions of SDS

One of the main difficulties when working with highly diluted concentrations of surfactants is the weak intensity of the Raman signal. The first step of the analysis is to investigate which peaks belong to the surfactant, to water and the surrounding devices. Figure 4-13 illustrates the Raman spectrum of SDS as received after correction of the baseline with the airPLS algorithm. The Raman spectrum of SDS was observed through the sapphire glass. As mentioned before, the baseline is subject to change and was not the same as the one presented in Figure 4-1. Appendix D gives an illustration of the baseline shape observed during the acquisitions of aqueous solutions of SDS.

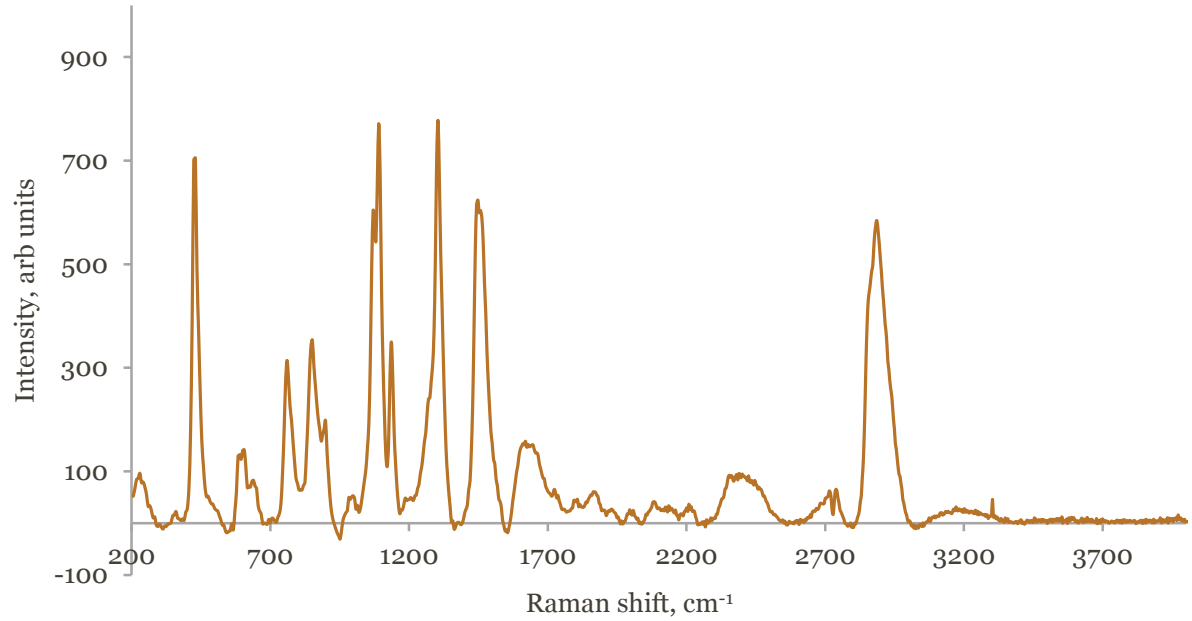

Figure 4-13: Raman spectrum of SDS powder after baseline correction

Peaks at 424 and 760 cm^{-1}, characteristic of the sapphire glass, are noticeable in Figure 4-13. This is, once again, due to the weak Raman signal of the SDS powder. Table 4-7 reports the different bands of SDS illustrated in Figure 4-13 as well as the frequencies reported for solid SDS in the literature.

Table 4-7: Vibrational frequencies of the SDS powder

vibrational mode	solid SDS (84), (35)	experimental vibrational frequency (cm^{-1})
SO_3^- -not specified	425	430
SO_3^- - not specified	573	-
SO_3^- - not specified	600/598	600
SO_3^- - not specified	635	639
S-OC-not specified	841	851
CH_3 rocking	891	899
S-OC- not specified	1000	998
C-C asymmetric stretching	1065	1070
C-C stretching-in gauche conf.	1087/1088	1090
C-C symmetric stretching in trans conf.	1130/1131	1136
CH_2 twisting	1295/1298	1298
CH_2 wagging	1373	1372
CH_2 bending	1436 and 1456	1448
Fermi resonance	2860	-
CH_2 asymmetric stretching	2881	2885
Fermi resonance	2900	-
Fermi resonance	2935	-
CH_3 asymmetric stretching	961	-

Most peaks have a good spectral matching with the literature. Some bands such as Fermi resonances, however, are not observed on the experimental Raman signal of the SDS powder. Once again, the Raman spectrometer is not a scientific grade device and the signals generated might not be of high quality.

Figure 4-14 illustrates the average spectra corresponding to a range of SDS concentrations in water from 0 to 34.6 mmol/L. The CMC of the SDS in water at these conditions ranges roughly from 6 to 8 mmol/L.

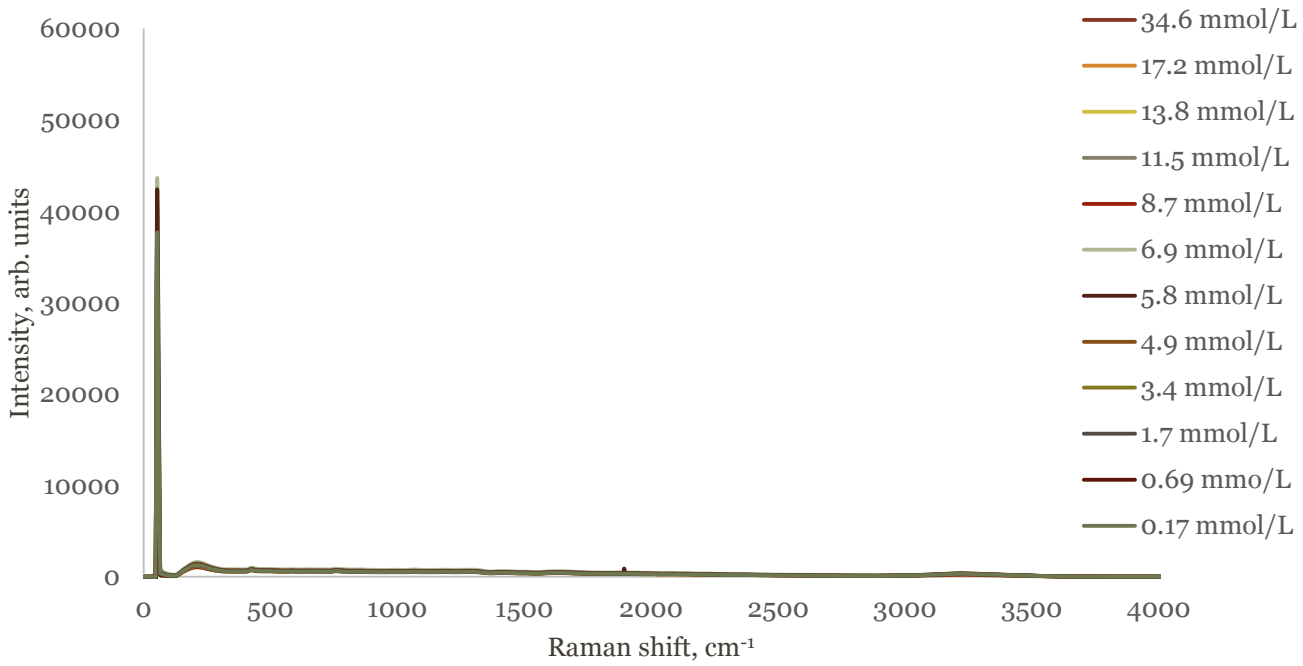

Figure 4-14: Raman spectra of the different dilutions of SDS in water.

As illustrated in Figure 4-14, the Raman signals of the SDS dilutions are weak and the initial intensity scale does not allow a good visualisation of the spectra. This plot does show, however, that fluorescence is not an issue with SDS solutions in water. Peak enhancement and normalisation to the frequency at 424 cm^{-1} were applied in order to adjust the intensity scale. Another possibility for normalization is to calculate the total area of a Raman spectrum, but this procedure took longer to implement and did not yield better results than normalisation to the same frequency. Consequently, this method is not presented in this thesis. Figure 4-15 illustrates five of the spectra presented previously in Figure 4-14 after scale adjustment.

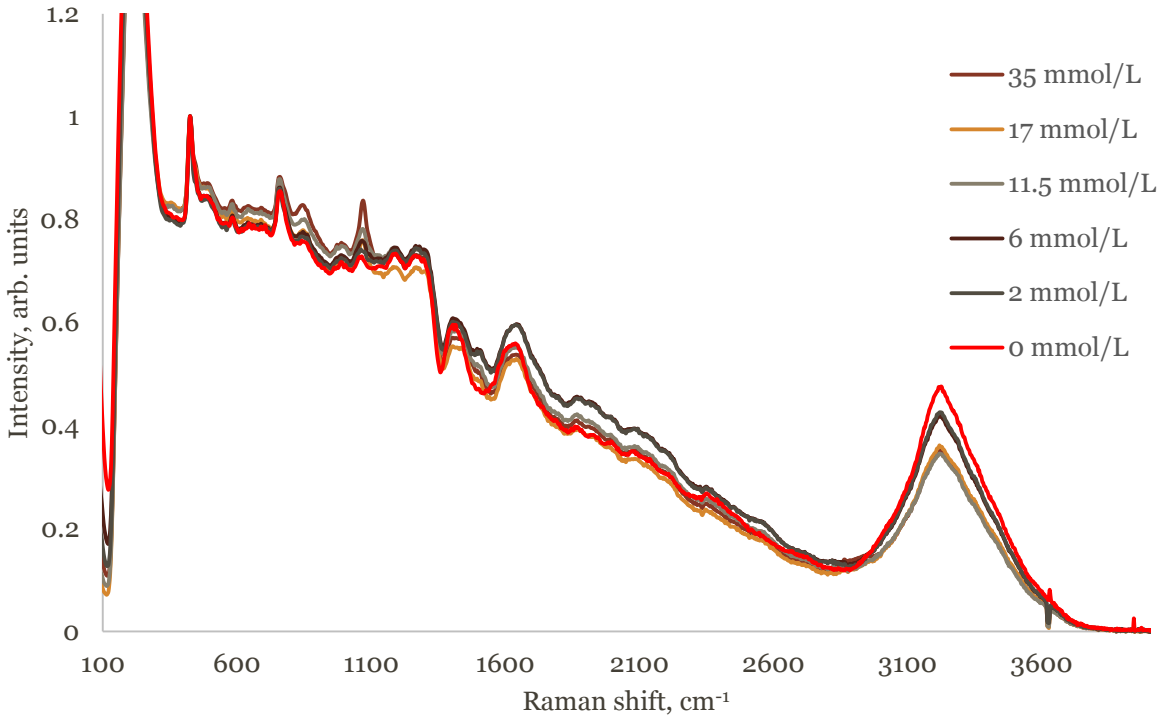

Figure 4-15: Average spectra for five concentrations of SDS in water.

All these spectra were acquired at one specific date. Three more sets of spectra were recorded at different observation dates and were consistent with the data presented in Figure 4-15. These data are presented in the appendix D.

As seen in Figure 4-15, the signals present a baseline drift. As mentioned earlier, the Raman spectra of SDS dilutions in water do not exhibit fluorescence. Such an irregular baseline can be corrected using the airPLS algorithm described in section 3.3.8.1. Figure 4-16 illustrates the Raman signals of the aqueous solutions of SDS after baseline correction.

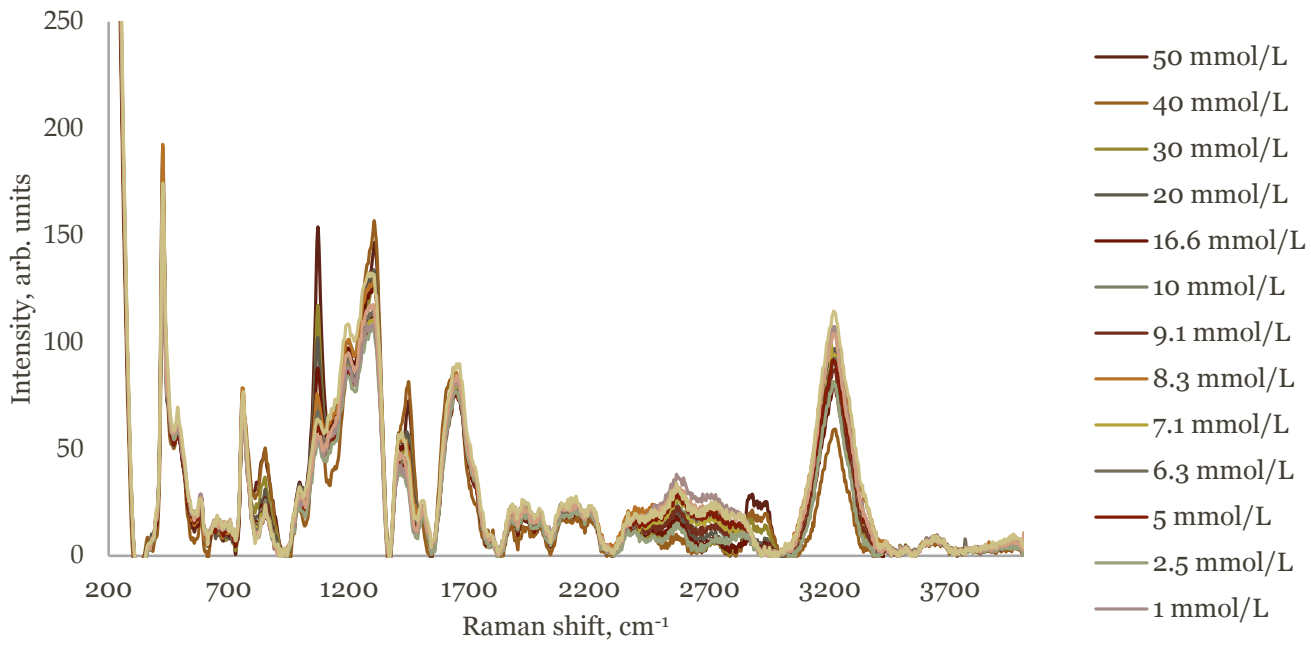

Figure 4-16: Raman spectra of aqueous solutions of SDS after baseline correction

As it illustrated in Figure 4-16, the airPLS algorithm corrects the baseline of the Raman spectra. At this stage, it is, however, unknown if the peak fluctuations are fingerprints of the SDS dilutions or if they are uncertainties coming from the algorithm. As such, this study will focus on interpreting raw spectra.

Working with highly diluted solutions of SDS is difficult because the peak intensities are weak. A significant number of peaks in these spectra can be attributed to either the sapphire glass or water. As described earlier, three main bands at 1185, 760 and 424 cm^{-1} in these spectra are attributed to the presence of the sapphire window. Characteristic peaks of water are also present in the Raman spectra of such highly diluted solutions, at 1504 cm^{-1}, 1652 cm^{-1} and 3225 cm^{-1}. A detailed assignment of the observed peaks is outlined in Table 4-8. All samples studied in this experiment contained low amounts of SDS in order to get data below and above the CMC.

Table 4-8: Characteristic bands of aqueous solutions of SDS

frequency (cm^{-1})	assignment for the aqueous solutions of SDS (35)
424	sapphire window
487-493	sapphire window
583	SO_3^- vibration-not specified
760	sapphire window
841	SOC vibration- not specified
988	SOC vibration-not specified
1060-1070	Superposition of asymmetric C-C stretching and symmetric SO_3^- stretching (85) / sapphire window
1185	sapphire window
1265	unassigned
1295	CH_2 twisting-sapphire window
1410	unassigned
1504	unassigned
1652	water- O-H stretching
286-	Symmetric CH_2 stretching
2939-2942	Symmetric CH_3 stretching
3225	water- O-H stretching

When looking at Figure 4-15, the Raman spectra of all dilutions seem to be similar to that of distilled water except in the 1300-1000 cm^{-1} region where the peak at 1060 cm^{-1} enlarges significantly as the concentration of SDS increases. As mentioned before, both the hydrocarbon chain and sulfonate head-group have Raman active stretching vibrations around 1060 cm^{-1}. There is still some controversy concerning the attribution of this band to a specific group. One study assigned the peak at 1062 cm^{-1} to the C-C stretching and the peak at 1082 cm^{-1} to the stretching of SO_3^- (86). A different paper assigned the band at 1062 cm^{-1} to the stretching of the sulfonate stretching. Another interpretation, which will be retained in the rest of this thesis, suggests that band at 1062 cm^{-1} is a combination and superposition of the skeletal C-C and SO_3^- stretching (35), (85). Sections 4.3.1.1 and 4.3.1.2 report intensity and frequency studies of this band and aim to approximate the CMC of SDS.

4.3.1.1. Determination of the CMC with Raman peak intensity

One study has been found in the literature describing the determination of the CMC of SDS solutions in water (33). This study correlated the intensity ratio of strongly bonded hydroxyl groups to weakly bonded hydroxyl groups with SDS concentration. Using this correlation, the

study estimated the early stages of micellization. The proportion of hydrogen bonding is affected around the spherical micelles, accounting for a sudden decrease of the intensity ratio around the CMC. As mentioned before, the Raman signal of water acquired with the experimental setup is not as precise as in the literature and the intensity ratio of strongly to weakly bonded hydroxyl group, localised in the high frequency region, could not be observed and calculated. This study focuses on a different region of the Raman spectrum, more precisely the 1300-950 cm^{-1} region, which shows great variation with the concentration of SDS. Figure 4-17 shows the spectral region where the intensity variations are noticeable.

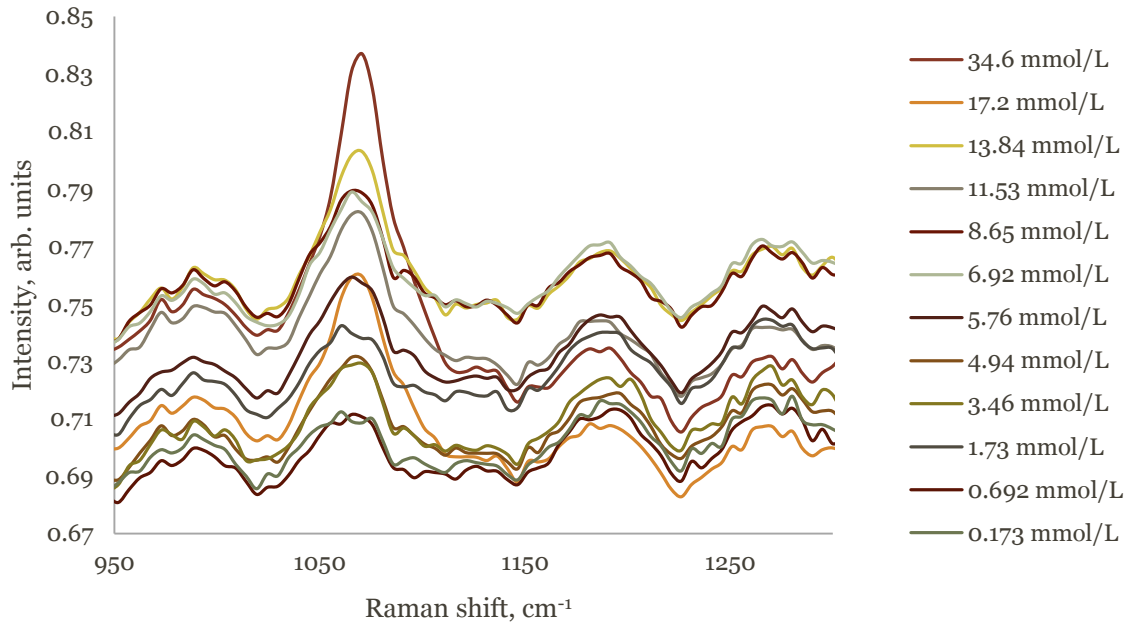

Figure 4-17: Raman spectra of different concentrated solutions of SDS in the 1300-950 cm^{-1} region, with a particular emphasis on the evolution of the 1062 cm^{-1} band, which is attributed to the C-C stretching of the hydrocarbon tail and SO_3^- stretching.

The normalisation at 424 cm^{-1} does not provide the best scale to observe the intensity variations of the 1062 cm^{-1} band. Figure 4-18 represents two possible ways of normalising these Raman spectra.

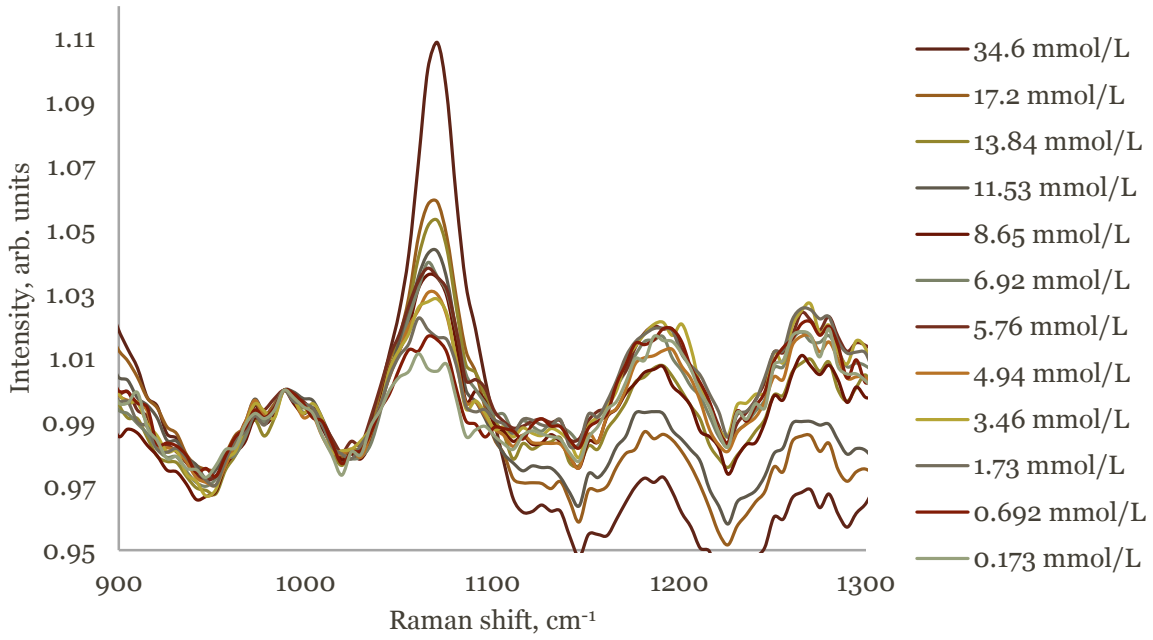

(a)

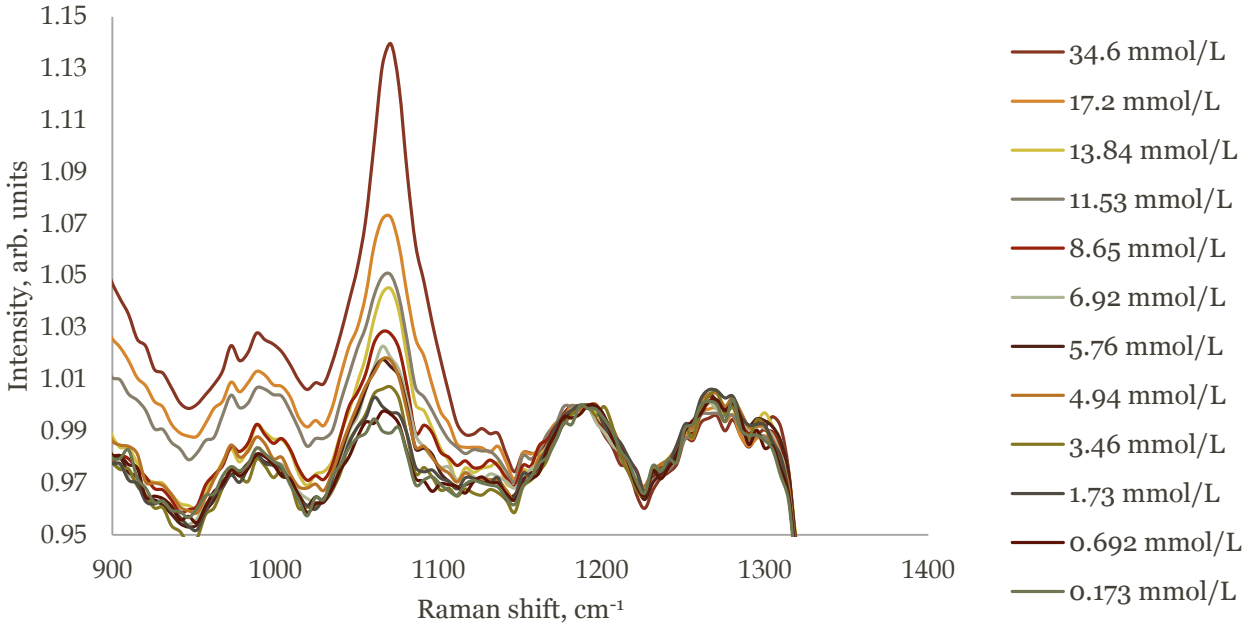

(b)

Figure 4-18: Evolution of the 1062 cm^{-1} band with the concentration of the SDS. (a) Spectra normalised to the 988 cm^{-1} frequency; (b) Spectra normalised to the frequency at 1185 cm^{-1}.

Normalisation of all spectra to frequencies at 1185 cm^{-1} and 988 cm^{-1} were applied in order to get a better visualisation of the 1062 cm^{-1} band. Normalising to a different frequency can lead to differences. Figure 4-19 represents the intensity difference between the bands at 1062 cm^{-1} and 1185 cm^{-1} and the bands at 1062 cm^{-1} and 988 cm^{-1}. Both normalisations show an overall increase of the C-C stretching intensity at 1062 cm^{-1} with the concentration of SDS. The rate at which the 1062 cm^{-1} band grows is, however, not the same depending on the frequency used to normalise.

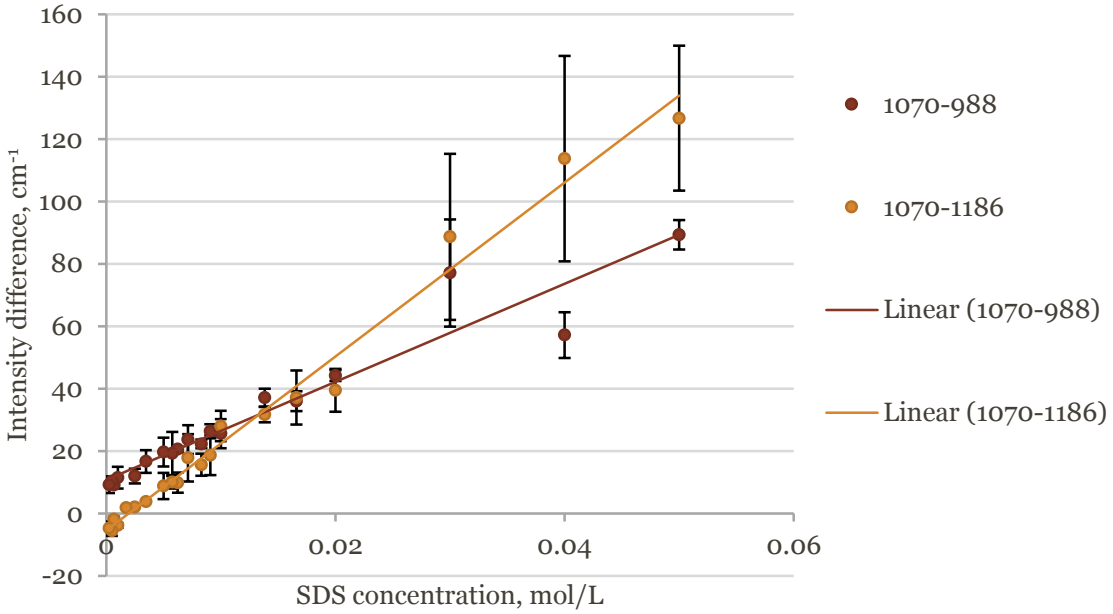

Figure 4-19: Evolution of the subtracted intensities with the concentration of SDS

Independently of the frequency used to normalise the spectra, the amplitude of the 1062 cm^{-1} band increases significantly with the concentration of SDS. Although the band at 1062 cm^{-1} is a combination of the asymmetric C-C stretching and sulfonate stretching vibrations, the intensity increase can be interpreted in terms of the asymmetric C-C vibration. The contribution of the SO_3^- stretching vibration to the intensity of the 1062 cm^{-1} band is not discussed because of the lack of information concerning its influence.

As mentioned before, self-association of surfactant can introduce configuration changes. The methyl and methylene vibrations, which are located in the 1300-1000 cm^{-1} and 3000-2800 cm^{-1} regions of the Raman spectrum, are good indicators of the trans/gauche conformational equilibrium of the hydrocarbon tails and are reliable measure of the intra-chain disorders (86), (87). Packing of alkyl chains inside the core of micelles pushes the carbon atoms to rotate and

adopt different configurations. The transition from a well-ordered trans-structure of free molecules to a gauche configuration, dominant in aggregates, is illustrated in Figure 4-20.

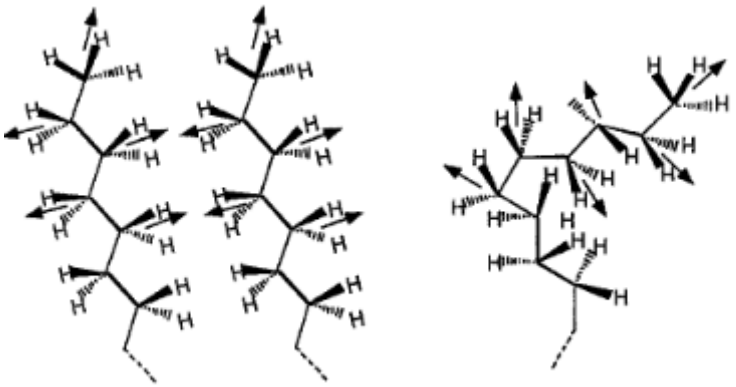

All-trans conformation Gauche conformation

Figure 4-20: Transition from an all-trans conformation to a gauche conformation (88)

Below the CMC, the chain-chain Van der Waals forces keep the alkyl chains at the water/air interface well-ordered, accounting for the all-trans configuration of the skeletal hydrocarbon chain (89). The rule of mutual exclusion, mentioned in section 2.1.6.2, predicts that asymmetric vibrations contribute little to the Raman spectrum of well-ordered and symmetric alkyl chains. The low intensity of the 1062 cm^{-1} band for low concentrations of SDS, as illustrated in Figure 4-19, suggests that the alkyl chains are mostly in an all-trans configuration.

Confinement and packing of alkyl tails inside the micelle core disrupts the symmetry and lead to chain distortion and disorder. The portion of the alkyl chain, which is oriented towards the water, is partially hydrated and adopts a trans-configuration characteristic of crystalline SDS (86). The rest of the hydrocarbon tail, which is localised at the center of the core, is bended and shows fluid-like properties, as very little water is present. As such, this part adopts the same gauche-like configuration as in liquid hydrocarbons. The fact that gauche conformers are indicators of disorder is a well-known fact. Picquart studied the differences between crystalline SDS and liquid SDS and observed that increasing disorder by melting the surfactant is accompanied by an increase of gauche conformers (35). The sudden increase of the intensity of the 1062 cm^{-1} band, observed around 7 mmol/L, and mainly due to the increase of the C-C asymmetric vibration, is indicative of the formation of micelles. The intensity increase of the asymmetric vibration suggests that a hydrocarbon phase is formed inside the core of a micelle, allowing previously hindered C-C transitions and disrupting the symmetry of the hydrocarbon backbone.

In order to quantify the increase of the 1062 cm^{-1} band, intensity ratios involving this band were calculated for all concentrations of SDS and observation dates. Most of the frequencies present in the Raman signals of the dilution were used in the calculation of the intensity ratios. Only three intensity ratios are illustrated in this thesis because of their repeatable trends over the four observations:

- I(1062)/I(1300) cm^{-1} intensity ratio. The band around 1300 cm^{-1} is characteristic of methylene. Previous studies stated that this vibration is conformer and temperature independent, making it a good candidate to study intensity changes in other part of the Raman spectrum (90), (91).
- I(1185)/I(1062) cm^{-1} intensity ratio. The band at 1185 cm^{-1}, although unassigned, shows the same evolution as the band at 1300 cm^{-1} throughout the different concentrations of SDS. The similarity between both bands is illustrated in Figure 4-18 (b).
- I(988)/I(1062) cm^{-1} intensity ratio. The band at 988 cm^{-1} is reported to be characteristic of the S-O-C stretching. The low error bars relative to this band, as illustrated in Figure 4-19, make it an interesting candidate for the intensity study.

The intensity ratios were plotted *versus* the SDS concentration in distilled water. In a second step, an average over the four observations was calculated. Working with dimensionless parameters such as intensity ratios enables to eliminate the uncertainties due to laser fluctuations and environmental noises, giving more precise and reliable data. Figures 4-21, 4-22 and 4-23 represent the evolution of these three intensity ratios averaged over the four observations.

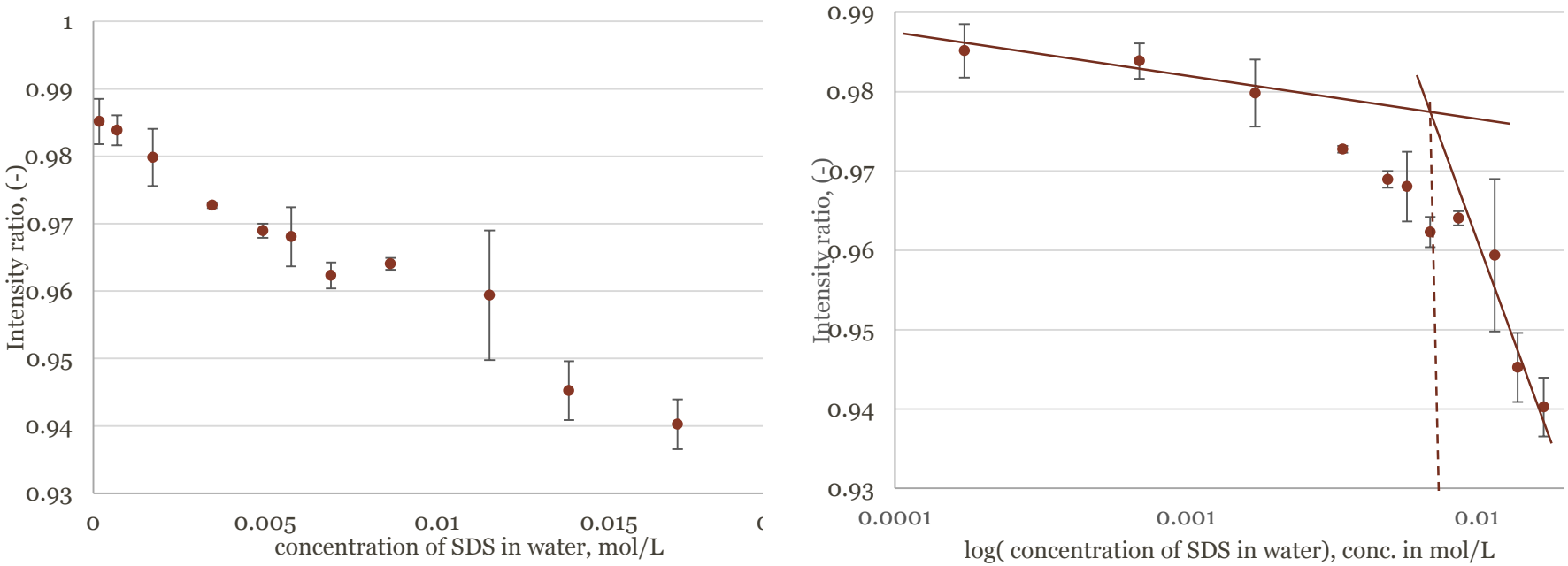

Figure 4-21: Evolution of the I(988)/(1062) cm^{-1} intensity ratio with the SDS concentration in water. The error bars account for the standard deviation

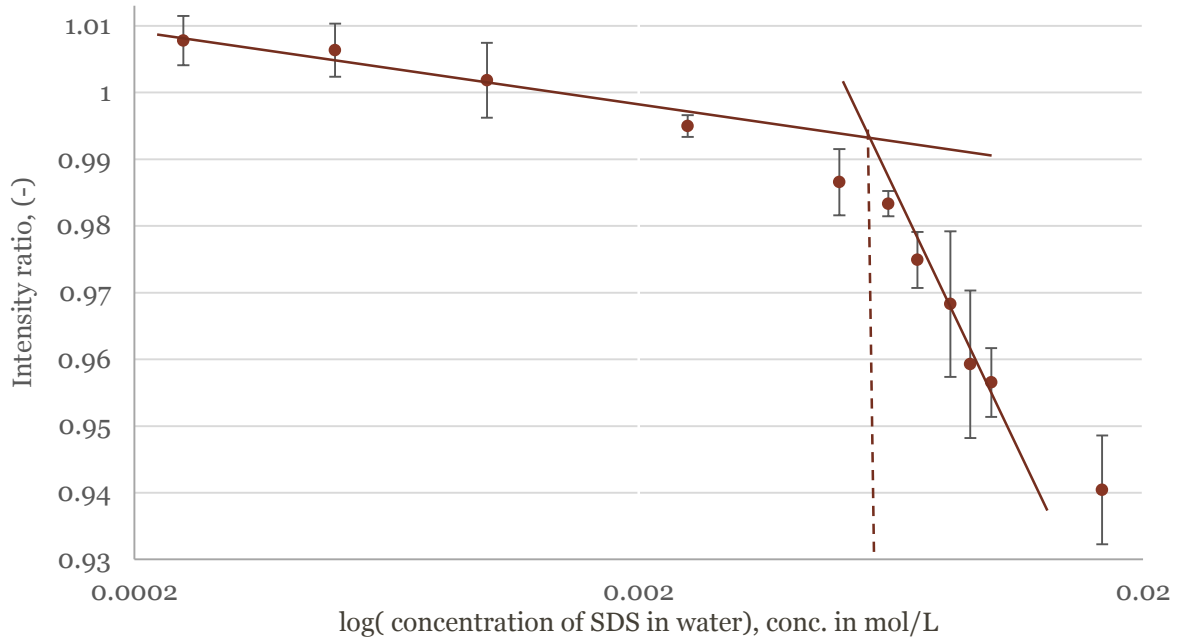

Figure 4-22: Evolution of the I(1185)/(1062) cm^{-1} intensity ratio with the SDS concentration in water. The error bars represent for the standard deviation.

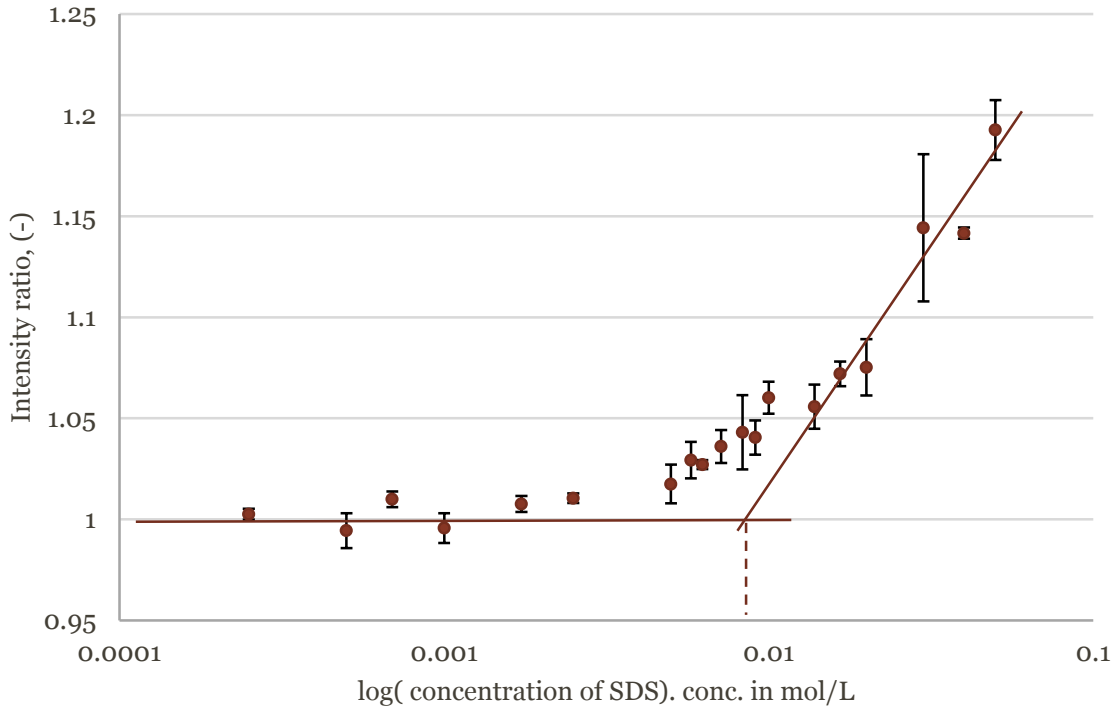

Figure 4-23: Evolution of the I(1062)/I(1300) cm^{-1} intensity ratio with the concentration of SDS in water. The error bars represent for the standard deviation

The logarithmic scale is a nonlinear scale which enables to obtain a better visualisation over the wide range of concentration. This scale adjustment enables to observe breakpoints on both Figure 4-21, Figure 4-22 and Figure 4-23. Error bars relative to the deviation from the average value are also represented. The horizontal error bars describing the relative deviation from the concentrations on the axis are, however, not indicated in these graphs. The preparation of the dilutions is described in section 3.3.3.1. Experimental errors coming from dilution of the stock solution and preparation of the dilutions can be a reason explaining deviation. Additionally, the most diluted solutions were prepared by measuring volumes of previous dilutions. Such a practice multiply the errors related to the previous dilution with the error when preparing the dilution in question.

The value corresponding to the intersection between the two lines drawn from the points forming the straightest sections below and above the breakpoint were calculated and compared with the CMC of SDS reported in the literature. Values of 7 mmol/L, 6 mmol/L and 9 mmol/L were calculated from the three intensity ratio curves. These three values are in the CMC range reported in the literature (30), (31), (32), (33).

As observed in Figure 4-21, Figure 4-22 and Figure 4-23, the transition to the CMC is progressive and is not defined by a sharp shift. Recalling Figure 2-9, the CMC is not defined by a specific value. The values of all physical properties plotted *versus* the concentration of SDS, as presented in Figure 2-9, show breakpoints over a limited range of concentrations. The data collected from surface tension, conductivity or detergency experiments are measurement dependent, accounting for different CMC values. Spectroscopic methods, however, are extremely sensitive to conformational changes that are associated with the early stages of self-association. Gradual transitions to the CMC reported by the Raman study suggest that the CMC is not defined by a precise breakpoint but rather by a concentration range.

4.3.1.2. Validation of the intensity study

In order to verify that the breakpoints observed previously are actually an accurate and reliable measure of the CMC, decrease of the CMC by addition of ionic salts was investigated using the same technique. Aqueous solution of sodium chloride at 0.02 mol/L and 0.1 mol/L were prepared and used as the solvent for the dissolutions of SDS.

Effect of ionic salts addition on the CMC of surfactants has been investigated (31). It was observed that the addition of salt result in the decrease of the CMC value. The magnitude of the decrease depends on the valence and concentration of the cation. The ionic strength of the salt

also influences the hydrodynamic radius of the micelles but it was found that this change is negligible in the case of sodium chloride. The presence of ionic salts reduces the electrostatic interactions between the ionic head-groups of the surfactant molecules, making it easier for them to coexist in micellar aggregates. Adding salt lowers the surface tension and therefore the CMC. As such, the value of the breakpoint is expected to shift towards lower values as well. This section investigates these changes by reporting the concentration breakpoints for different concentrations of salt. Figures 4-24 to 4-29 illustrates the variation of the three intensity ratios for different concentrations of NaCl.

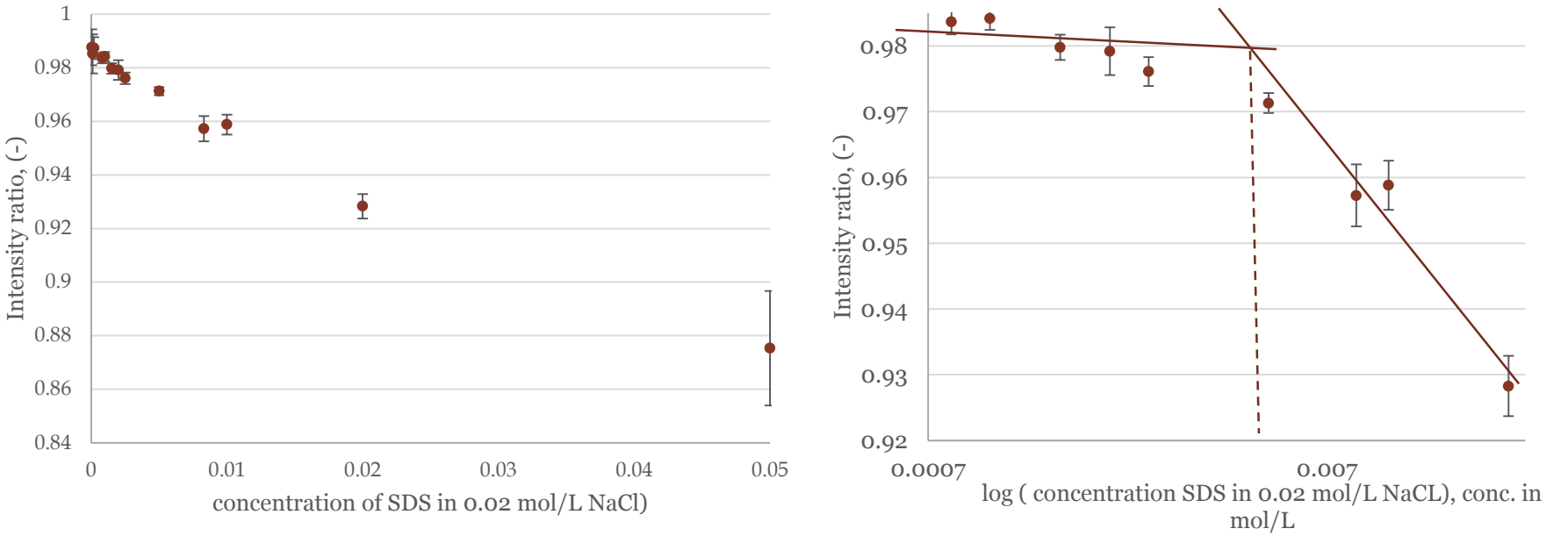

Figure 4-24: Evolution of the I(988)/(1062) cm^{-1} intensity ratio with the concentration of SDS in 0.02 mol/L NaCl. The error bars represent for the standard deviation

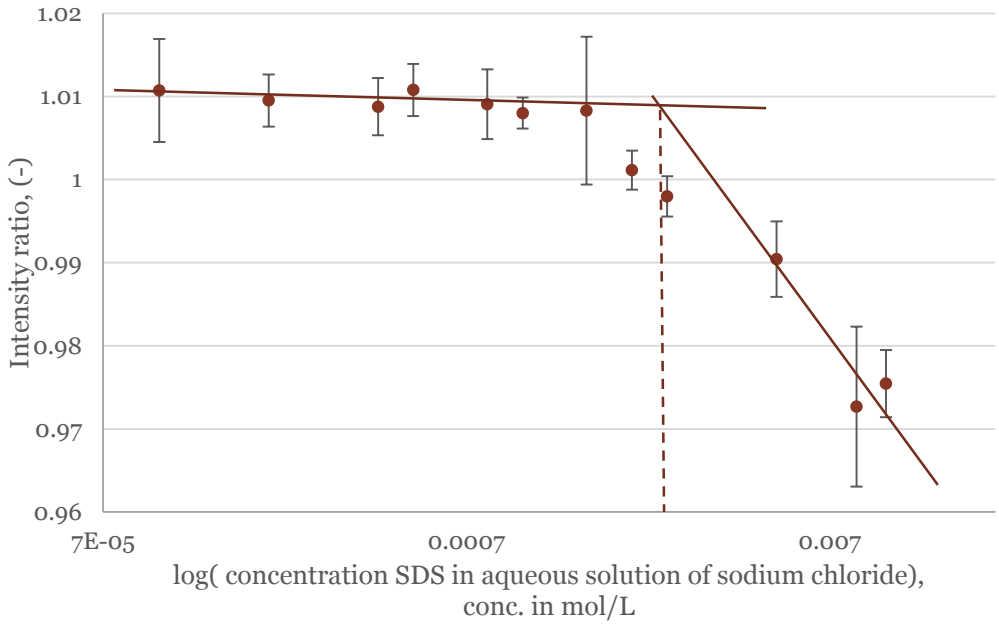

Figure 4-25: Evolution of the I(1185)/(1062) cm⁻¹ intensity ratio with the concentration of SDS in 0.02 mol/l NaCl. The error bars represent for the standard deviation

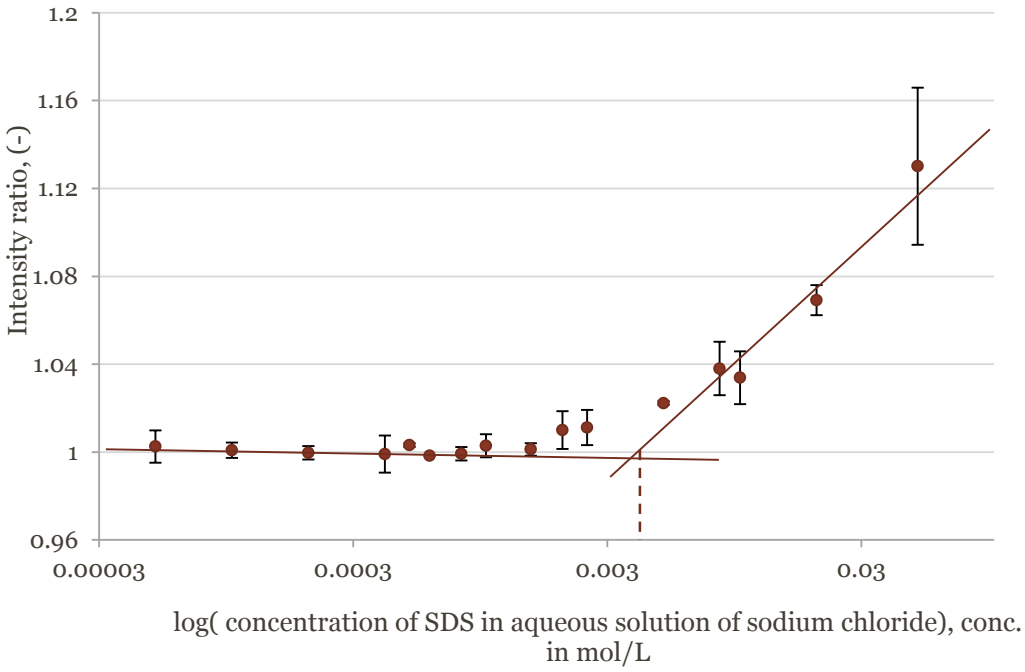

Figure 4-26: Evolution of the I(1062)/(1300) cm⁻¹ intensity ratio with the concentration of SDS in 0.02 mol/l NaCl. The error bars represent for the standard deviation

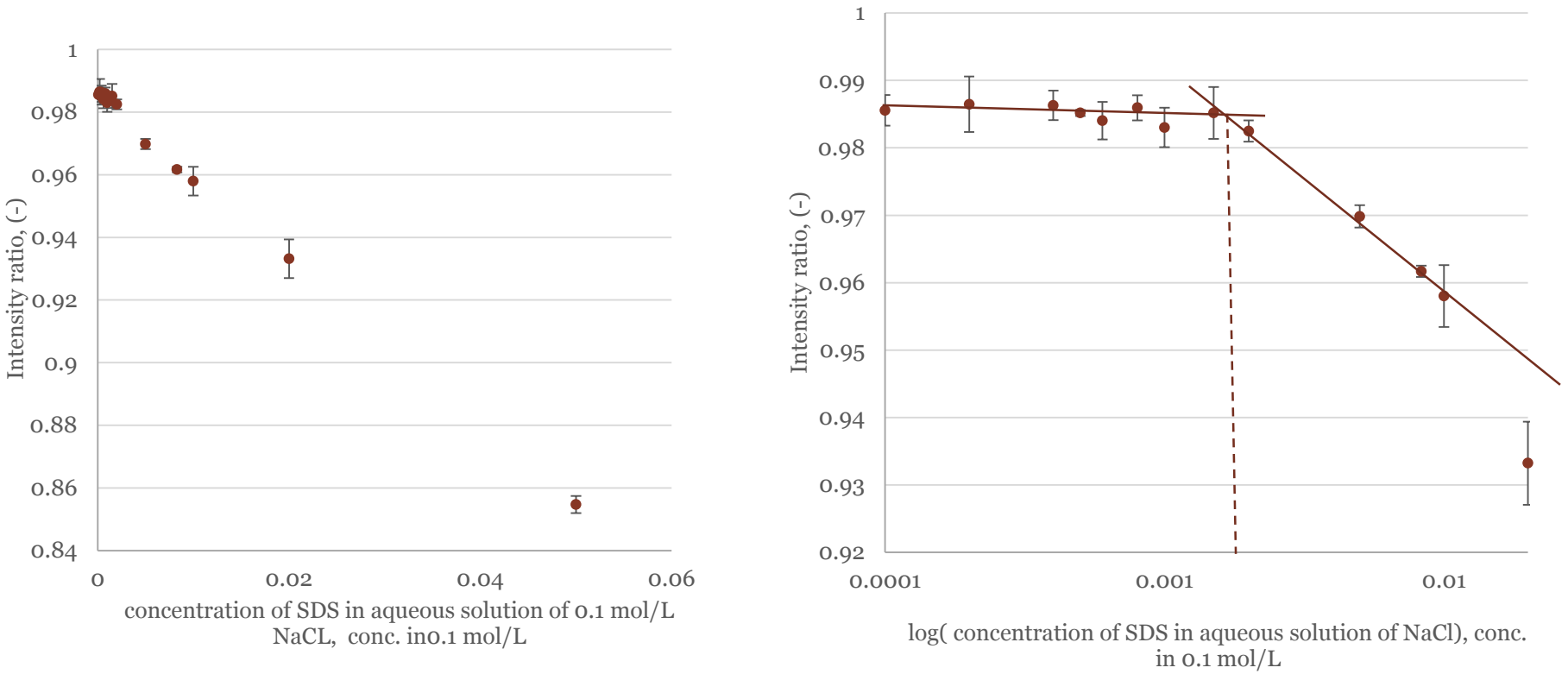

Figure 4-27: Evolution of the I(988)/(1062) cm^{-1} intensity ratio with the concentration of SDS in 0.1 mol/L NaCL. The error bars represent for the standard deviation

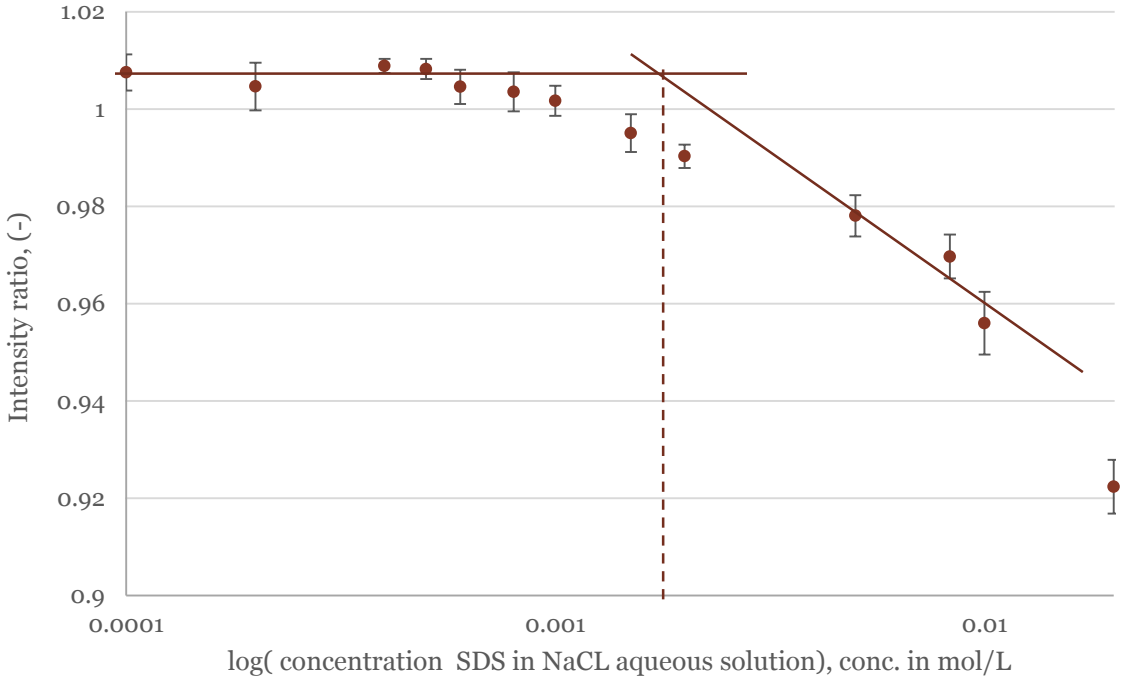

Figure 4-28: Evolution of the I(1185)/(1062) cm⁻¹ intensity ratio with the concentration of SDS in 0.1 mol/L NaCl. The error bars represent for the standard deviation.

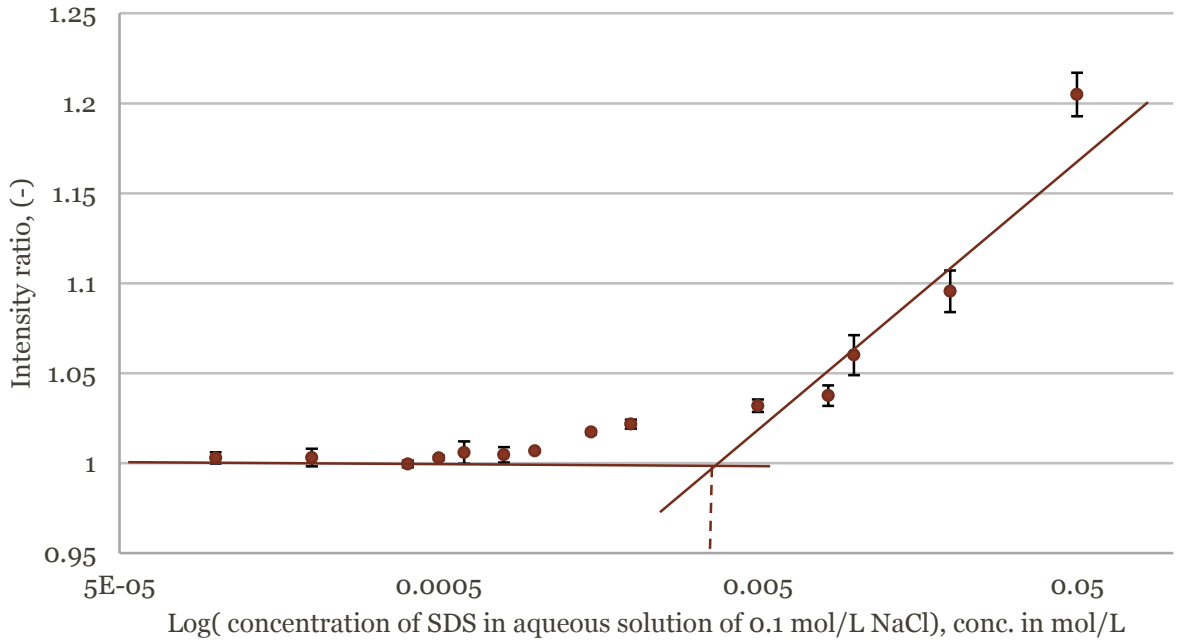

Figure 4-29: Evolution of the I(1062)/(1300) cm⁻¹ intensity ratio with the concentration of SDS in 0.1 mol/L NaCl. The error bars represent for the standard deviation

Table 4-9 reports the experimental values of the CMC in water, in 0.02 mol/L NaCl and in 0.01 mol/L NaCl. The CMC values from the literature are also reported in Table 4-9.

Table 4-9: Values of the CMC of sodium dodecyl sulphate (SDS) for different concentrations of sodium chloride at room temperature obtained in this project and comparison with the literature.

conc. of NaCl	**Raman study**				**conductimetry**	**fluorescence**	
	I(988)/I(1062)	I(1185)/I(1062)	I(1062)/I(1300)	I(3400)/I(3200) (33)	(31)	(32)	(30)
0	0.007	0.006	0.008	0.006	0.0078	0.0082	0.0073
0.02	0.0045	0.0025	0.003		0.0033		
0.1	0.0017	0.0012	0.003		0.0017		

The CMC values obtained with the intensity method fall within the concentration range reported in the literature. As mentioned earlier, the transition in the intensity ratio plots are gradual and not as sharp as other measuring methods. Additionally, the breakpoint values vary depending on the intensity ratio studied. Such differences are observable because each band intensity corresponds to a certain region of the molecule and a different environment, which are not affected the same way by self-association. A slow transition and the variety of CMC values obtained for different intensity ratio suggest that the CMC occurs over a range of concentrations.

4.3.1.3. Determination of the CMC with Raman peak frequency shifts

As mentioned previously, Raman intensities and frequencies are sensitive to structural arrangement. Conformational changes such as folding and stretching of the hydrocarbon chain can be introduced by geometrical rearrangement and result in a variation of electronic states and a modification of the polarizability tensor (92), (91). Figure 4-30 illustrates the frequency shifts of the 1062 cm^{-1} band as the concentration in SDS increases.

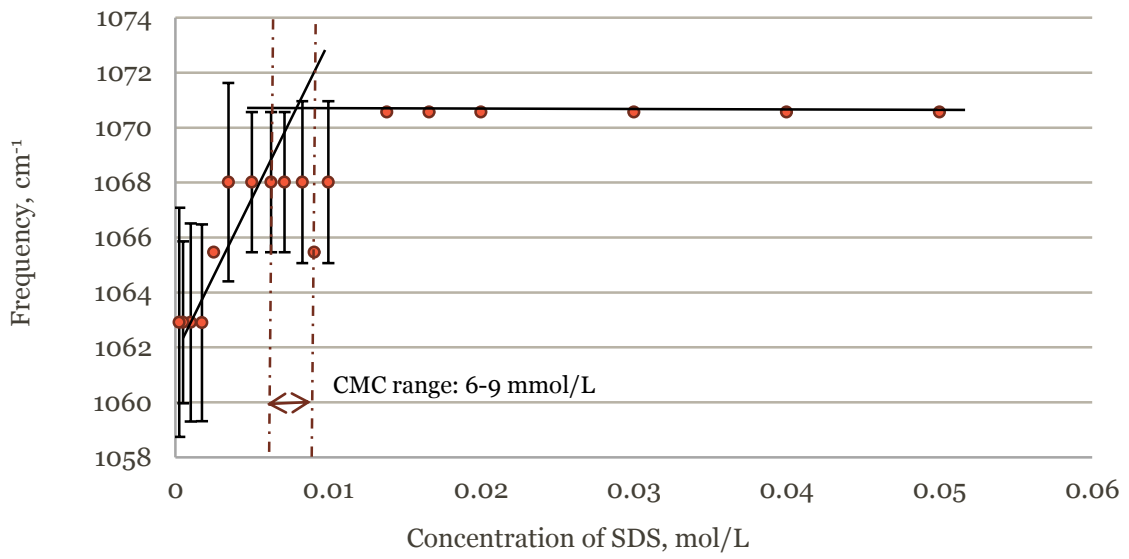

Figure 4-30: Frequency dependence of the combination band of C-C and SO_3^- stretching vibrations. The average values were calculated over the four observations.

As mentioned before, The C-C stretching vibration of gauche bonds, which is specific to amorphous hydrocarbons, is localised at 1080 cm^{-1} and gets more intense when the gauche contribution increases. The out-of-phase symmetric stretching C-C vibration at 1060 cm^{-1} is characteristic of a trans structure found in trans-alkanes and crystalline SDS (91), (93), (94). Considering this, Figure 4-30 might be an illustration of the trans/gauche equilibrium shift that occurs when micelles start to form. For concentrations of SDS below the CMC, the alkyl chains at the air-water interface have an all-trans configuration, as indicated by the C-C stretch located at 1062 cm^{-1}. As micelles are forming and growing, the number of surfactant molecules inside the aggregate increases, forcing the hydrocarbon tails to fold and adopt more gauche conformations. This is illustrated by a shift of the C-C stretching frequency towards 1080 cm^{-1}. No frequency shifts between pre and sub-micellar solutions would be expected for the sulfonate head-group as it remains globally hydrated before and after micellization. As illustrated in Figure 4-30, two straight lines can be drawn from the intensity plot. The first line represents the increase of gauche conformers and the second one illustrates the equilibrium between trans/gauche conformers. Considering that a trans/gauche equilibrium is reached when micelles are formed, the CMC can be roughly estimated from Figure 4-30. The intersection of the two lines corresponds to the 8 mmol/L, which is within the CMC range reported in Table 4-9. This method, however, leads to important uncertainties and does not seem to be as robust as the intensity method illustrated in 4.3.1.1 and 4.3.1.2. The next section uses the intensity ratio method on a different surfactant, AOT.

4.3.2. Aqueous solution of AOT

Bis(2-Ethylhexyl)sulfosuccinate (Aerosol OT or AOT) is an anionic surfactant, containing a sulfonate head-group, as in SDS. Its structure, as presented in Figure 4-31, is however, slightly different than SDS, with two ester groups, both associated with a long hydrocarbon tail.

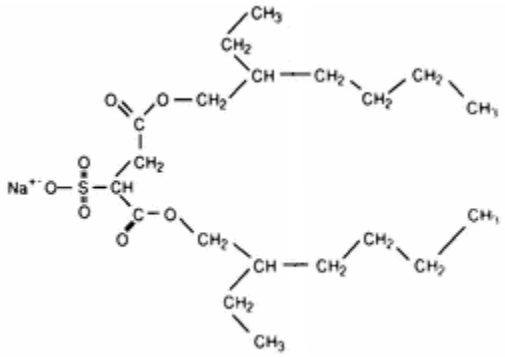

Figure 4-31: Chemical structure of Bis(2-Ethylhexyl)sulfosuccinate (95)

Figure 4-32 represents the Raman spectrum of solid AOT, averaged over four acquisitions. As the waxy structure of AOT is easier to handle than the SDS powder, the solid was placed directly on the ceramic plate, without the use of a sapphire window.

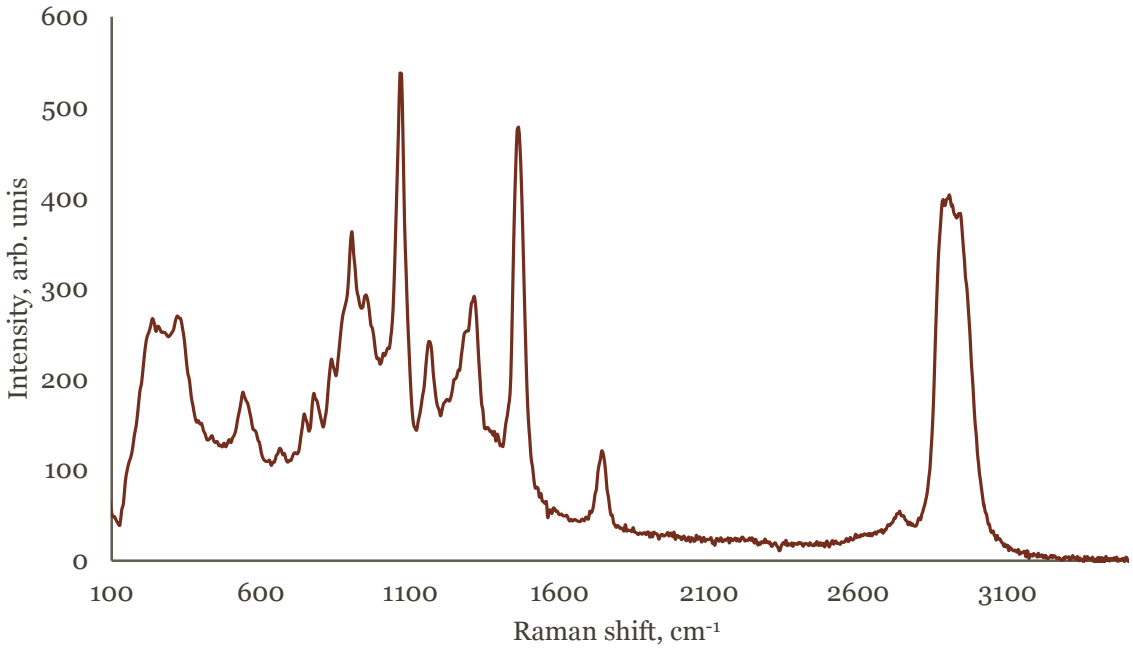

Figure 4-32: Raman spectrum of solid AOT

The Raman spectra of different aqueous solutions of AOT were acquired at three different times. Figure 4-33 shows the signals of the solutions in the 1300-900 cm^{-1} region for one specific date. The three experiments are presented in Appendix E.

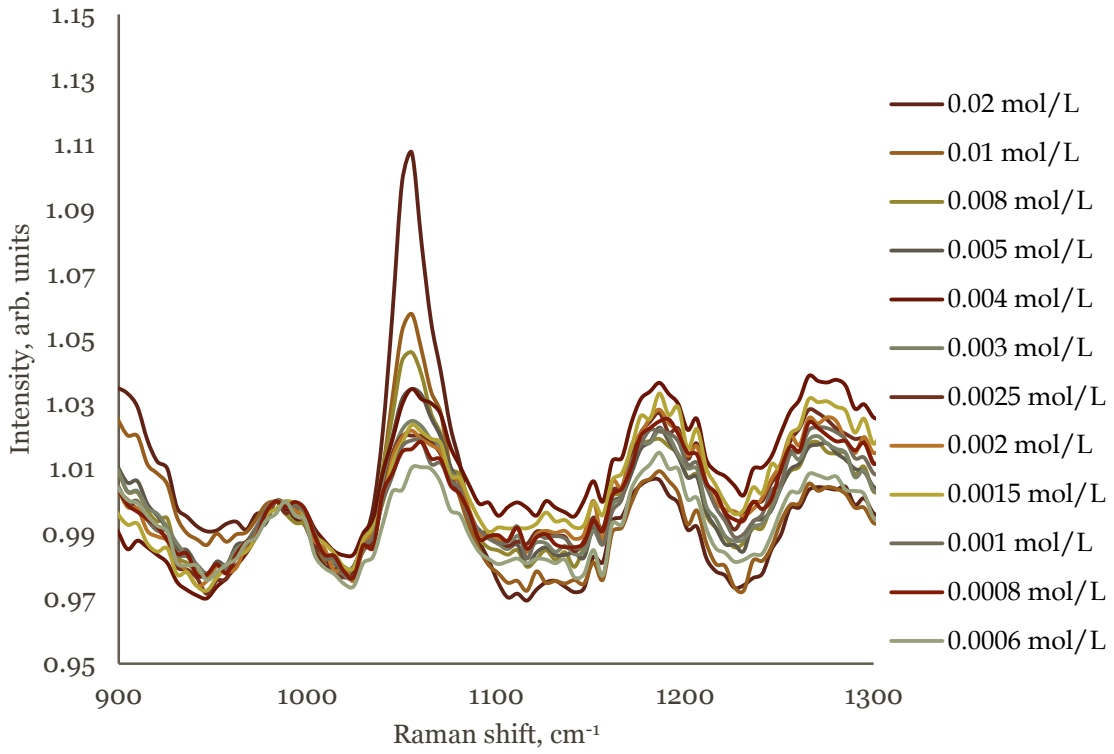

Figure 4-33: Raman spectra of aqueous solutions of AOT in water

The band localised at 1055 cm^{-1} is the only one showing a significant change with an increase in the AOT concentration. This band was attributed in previous work to either the stretching of the SO_3^- head-group (39) or the skeletal vibrations (34). Similar to SDS, this band is assumed to be the combination of both vibrations.

This band, located at 1065 cm^{-1} in the Raman spectrum of solid AOT, as illustrated in Figure 4-32, is localised at 1055 cm^{-1} in the Raman signals of aqueous solutions of AOT. This shift can be explained by the tendency of the sulfonate head-group to generate hydrogen bonds with molecules of water. Such solute-solvent interactions decrease the vibrational frequencies of the S=O bond in aqueous solutions.

Moreover, the band, which is assigned to the same vibrations as in the SDS study, is located at 1055 cm^{-1} in the Raman spectra of aqueous AOT instead of 1062 cm^{-1} in the Raman spectra of aqueous solutions of SDS (39). Such a difference can be explained by considering two factors:

- The local environment of a bond can influence its frequency. Figure 4-34 illustrates the difference between the head-groups of SDS and AOT. The presence of an oxygen atom near the sulfate head-group in SDS strengthens the S-O bond. The inductive effect, caused by the extra oxygen atom, tends to make the sulfur atoms more electron-deficient. As a result, the S-O bond is strengthened and its vibrational frequency increases. This can be one reason why the combination band is localised at 1065 cm^{-1} in SDS and 1055 cm^{-1} in AOT.

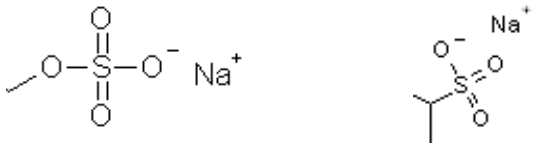

(a) (b)

Figure 4-34: Picture of the (a) SDS head-group and (b) AOT head-group

- The lower frequency at 1055 cm^{-1} can also be explained by assuming a bigger contribution from the head-group compared to that of the hydrocarbon chain in AOT molecules. Considering that the sulfonate head-group, in contrast to the skeletal hydrocarbon chain, can be involved in hydrogen bonds with water, the frequency observed for this band in aqueous solutions of AOT would be shifted toward lowers values.

Bands at 988 cm^{-1}, 1185 cm^{-1} and 1300 cm^{-1} are not present in the Raman spectrum of solid AOT but are observed in the Raman spectra of aqueous solutions of AOT. The band at 1300 cm^{-1}, which is attributed to the methylene twisting vibration, is assumed to be independent of the surfactant concentration (90), (91). No significant changes in frequency with the concentration of AOT were reported for this vibration. The intensity ratios were measured, averaged and plotted the same way as in the SDS experiments. The intensity ratios for AOT in water are presented in Figures 4-35, 4-36 and 4-37.

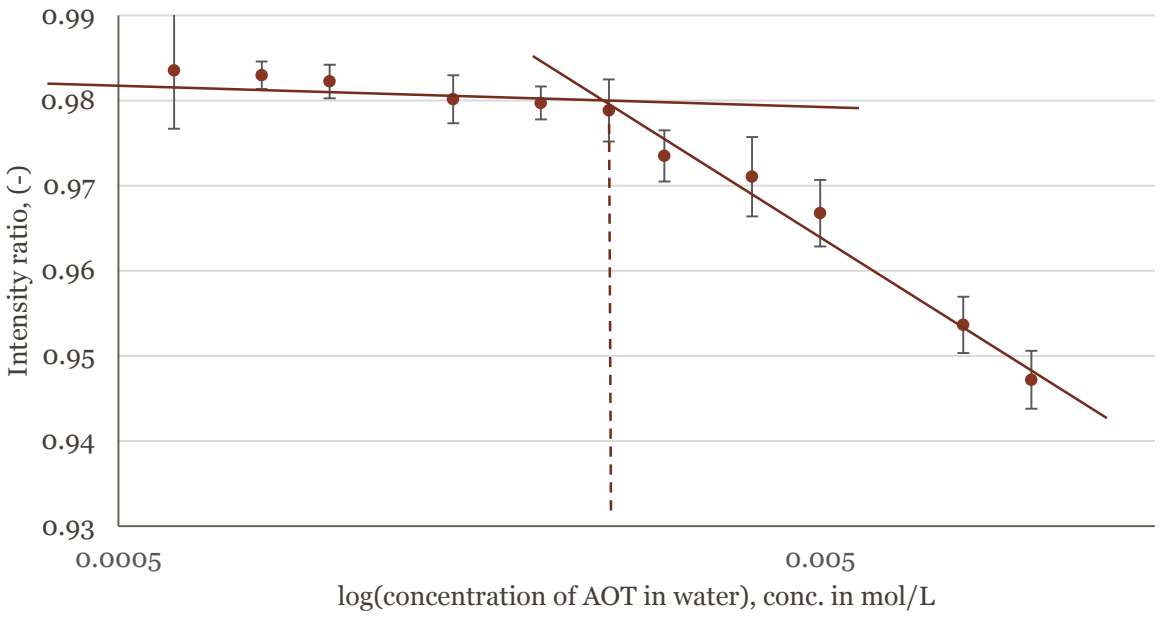

Figure 4-35: Evolution of the I(988)/(1055) cm-1 intensity ratio for aqueous solutions of AOT.

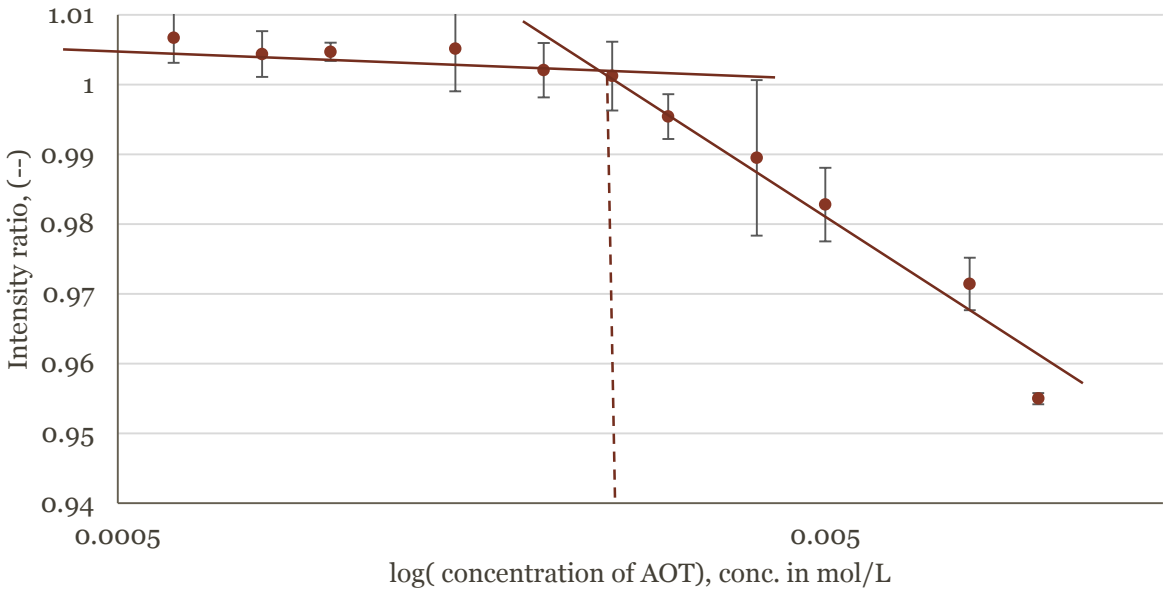

Figure 4-36: Evolution of the I(1185)/(1055) cm-1 intensity ratio for aqueous solutions of AOT.

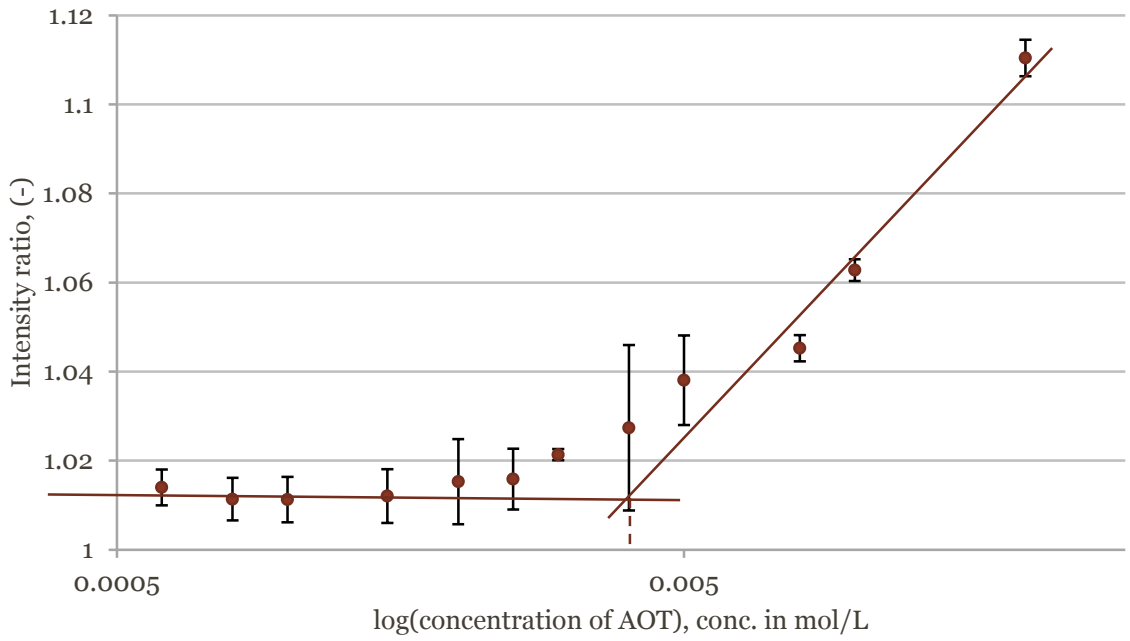

Figure 4-37: Evolution of the I(1055)/(1300) cm^{-1} intensity ratio as a function of the AOT concentration in water.

The three intensity ratios follow the similar trends for aqueous solution of SDS and AOT. The band at 1055 cm^{-1} slowly increases as the concentration of AOT increases. The breakpoint concentrations were measured for the three intensity ratios and are reported in Table 4-10.

Table 4-10 Values of the CMC calculated from the intensity ratio study

	Raman spectroscopy			**literature**
	I(988)/I(1055)	I(1190)/I(1055)	I(1055)/I(1300)	
Breakpoint conc.	2.6	2.5	4	2.9 (36), 2.45 (95) 2.56 (96)

All three experimental values are in good agreement with the CMC calculated in previous work. The CMC of two anionic surfactants in water were measured by studying the evolution of three different intensity ratios and the experimental values of CMC are in good agreement with the CMC range reported in the literature. The same method confirms that the CMC of SDS is decreased when adding electrolyte. As such, studying intensity ratios is an accurate way of measuring the CMC of anionic surfactants in water. The same technique applied to the formation of AOT reversed micelles in hydrocarbon solvent is presented in section 4.3.3.

4.3.3. Solutions of AOT in apolar organic solvent

Solutions of AOT in cyclohexane and toluene respectively were prepared and successively diluted in order to obtain concentrations above and below the CMC. Considering the low concentrations of AOT in these solutions ($2{,}5.10^{-5}$- 9.10^{-3} mol/L) and the strong signals of solvents, little changes were observed between the different solutions. More precisely, no significant and repeatable variation were identified among the different spectra of aqueous solutions of AOT. It is believed that the signal of the solvent completely overlaps the peaks of the surfactants and that the variations, observed previously in water, are not observable in these cases. Using a solvent with a lower dielectric constant and therefore a weaker Raman signal could lead to the observation of AOT peaks. The solvent with the lowest polarizability is pentane, with a short hydrocarbon chain, containing only five atoms of carbons. The Raman spectrum of this solvent was acquired and the intensity of the signal was found to be comparable to the signal of toluene or cyclohexane. Additionally, the interactions responsible for the formation of AOT reverse micelles in organic solvents might be too weak to cause any changes in the Raman signals of the dilutions.

It is also interesting to note that there is a considerable disagreement in the literature concerning the CMC of AOT in organic solvents. As illustrated in Table 2-2, the CMC of AOT in cyclohexane varies from 0.2 mmol/L to 1.8 mmol/L, depending on the measurement technique. Such uncertainties might come from the fact that the formations of reverse micelles are harder to identify. Unlike the experiments in water, the hydrocarbon tails of the surfactants are not as affected by the formation of reverse micelles because their environment is unchanged throughout the aggregation process.

Moreover, considering that variations in water were observed, as illustrated in section 4.3.2, but that no fluctuations were reported in hydrocarbon solvents, the question of the influence of water on surfactant self-association arises. Is there significant association without the presence of water? Section 4.3.4 studies the impact of water addition on AOT- isooctane systems.

4.3.4. Water-in-oil microemulsions- Study of the AOT/water/isooctane ternary system

As mentioned in section 2.3.4, IR and Raman spectroscopic studies of w/o microemulsions using AOT as a surfactant and isooctane as the organic solvent were conducted (39). Unlike section 4.3.1 and 4.3.2, this study focuses on frequency shifts because of the abundant literature treating this subject.

4.3.4.1. Frequency study

Moran *et al.* observed that the frequency of the sulfonate (SO_3^-) stretching vibration is affected when water is added into the system (39). Such variations were attributed to a change of the interactions between water molecules and sulfonate head-groups. Other studies confirmed that the presence of water modifies the local environment around the sulfonate head group SO_3^- and therefore affects its symmetric stretching vibration band (97), (98).

A similar Raman spectroscopy study was carried out in this thesis and the results were compared with the literature. Figure 4-38 illustrates the evolution of the sulfonate stretching frequency as the amount of solubilized water inside the micelles (w_o) increases. This graph represents the average over three different observation dates. The same stock solution of AOT in isooctane was used for the three experiments but water was freshly added before each acquisition.

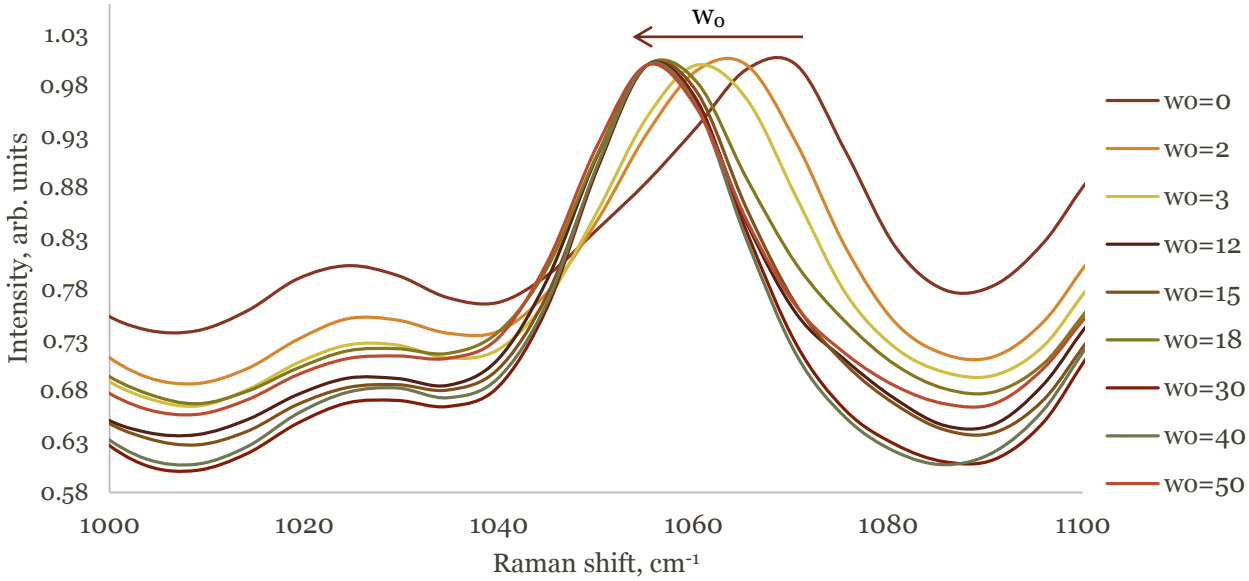

Figure 4-38: Evolution of the sulfonate stretching mode with the molar ratio of water to surfactant, w_o.

As soon as water is introduced inside the AOT/isooctane system, molecules of AOT start to self-assemble around the molecules of water, with the sulfonate head group located inside the water pool and the hydrocarbon tails pointing towards the organic solvent. Because of its amphiphilic nature and geometrical properties, AOT has the ability to solubilize a great amount of water inside these reversed micellar structures. Figure 4-38 shows that the frequency of the sulfonate head-group is 1062 cm^{-1} when no water is present. This observation is in agreement with the

vibrational frequencies of pure AOT, as illustrated in Figure 4-32 and reported by the literature (39). A frequency shift of the SO_3^- stretching mode towards lower values is observed as the amount of water inside the system increases. This decrease in frequency can be explained by a reduction in strength of the cation-anion interactions and the presence of hydrogen bonds.

Because of its important electro-attractive effect, the counterion Na^+ forms a strong dipole with the sulfonate group. This association results in an increase of the polarity around the sulfonate head group, and therefore accentuates the polarization of the S-O bond. The introduction of water inhibits the formation of such structures and results in a change of polarizability. Molecules of water disconnect the sodium cation from the sulfonate group by getting in between the two entities. The hydration process shields the sulfonate group SO_3^- away from the electrostatic force of Na^+. The spatial separation grows bigger and the interaction between the two entities becomes weaker as more water is added. This ionic so

.03lvation results in a depolarisation of the S-O bond and therefore a decrease of the vibrational frequency.

Additionally, the hydrogen bonds between the water molecules and the sulphur atoms of the sulfonate head group, represented in Figure 4-39, also decrease the strength of the S-O bond, accentuating the frequency shift.

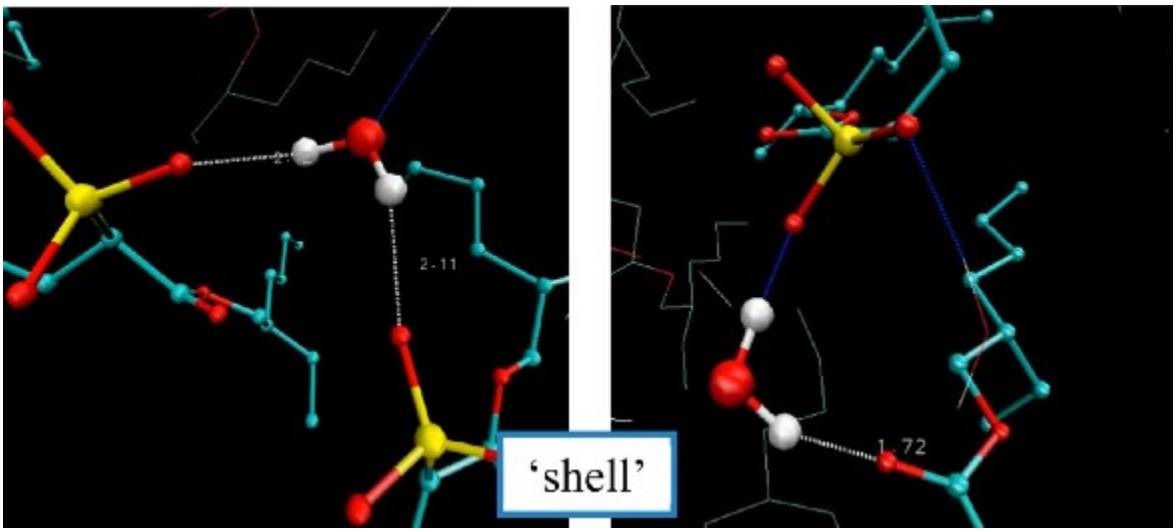

Figure 4-39: Schematic of the interactions taking place at the internal frontier of the reverse micelle. The system studied is a water pool surrounded by AOT molecule in isooctane. Oxygen is red, hydrogen is white, sulphur is yellow and carbon is blue (99).

Figure 4-40 shows the frequency shift of the sulfonate stretching mode as water is added inside the system:

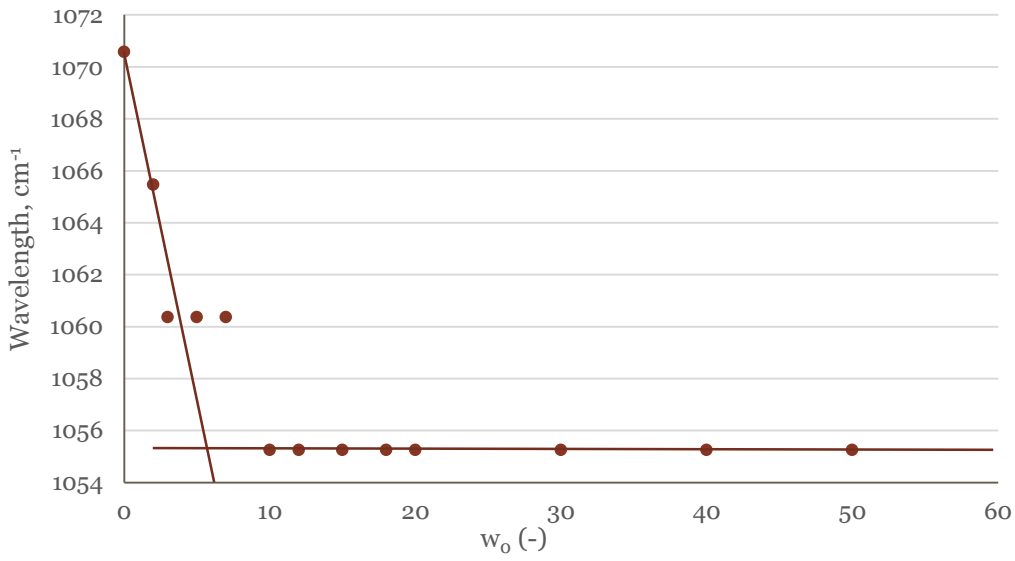

Figure 4-40: Shift of the sulfonate vibrational frequency with the molar ratio of water to surfactant (w_0)

Similar to the experiment described in the literature, three pieces of information can be obtained from this graph (39):

- The greatest variation occurs for $w_0 \leq 3$, which means that the vibration of the sulfonate head group is highly affected by the presence of the first three molecules of water. Hydration of the head group by the first three molecules of water is illustrated in Figure 4-41.

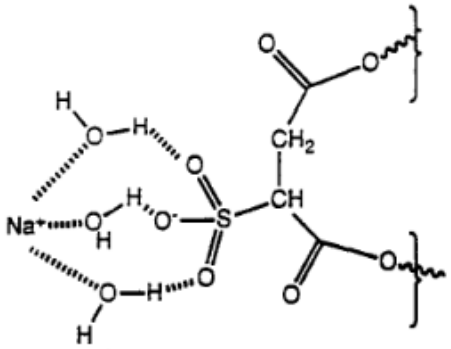

Figure 4-41: Representation of the hydrogen bonds between the sulfonate head group and the first three molecules of water (98).

- The intersection of the two slopes representing the two main trends is located at $w_0 \approx 5\text{-}6$. It means that the next three other molecules of water will also interact with the sulfonate

head-group, but not as strongly as the first three ones. A maximum of five to six molecules of water are bounded to the head-group and this number corresponds to the hydration number of the sodium cation (98), (39).

- No noticeable change of wavelength happens after w_o =10-12. This point defines the transition between the terms of reverse micelles and water-in-oil microemulsions. The water inside the core have similar properties as bulk water and are not affected by the presence of the sulfonate head-group.

The experimental results are in very good agreement with the results from Moran *et al.* As such, the frequency shift method is a viable analytical tool to study microemulsions of surfactants.

This section studied surfactant models, developed and validated two analytical methods, an intensity method and a frequency method, to study micelles and microemulsions respectively. Section 4.4 applies the models and methods studied in section 4.3 to study the aggregation of asphaltene in organic solvents.

4.4.Raman spectroscopy of Athabasca vacuum residue

4.4.1. Observation of VR with Raman spectroscopy

Asphaltenes, alike a wide range of chemicals, are also characterised by their surface activity. Association of such compounds is responsible for plugging and fouling of pipelines, as well as damaging chemical reactors. As other compounds such as resins play an important role in asphaltene self-association, the use of VR in this study, instead of extracted asphaltenes, is therefore more pertinent. Moreover, VR contains a significant amount of asphaltenes, which are the most polar and less soluble components in the crude oil. As such, studying solutions of VR in toluene gives a better understanding of what potentially happens during the aggregation process in crude oil. First, Figure 4-43 represents the Raman spectrum of Athabasca VR at room temperature.

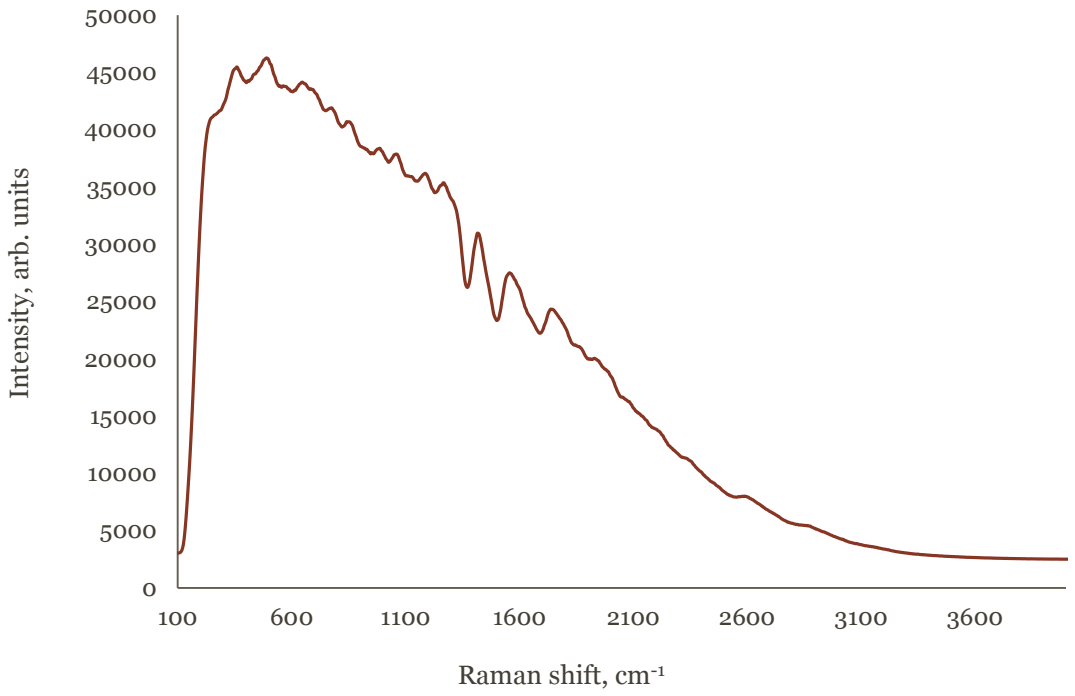

Figure 4-42: Raman spectrum of VR at room temperature and pressure.

As previously mentioned in section 4.2, Raman spectra of weakly associating systems present intensity and band shifts. The Raman signal of complex and highly interacting systems such as VR is unachievable without the use of analytical tools. Peak assignment is not possible when working with the raw spectrum of VR because of the following reasons:

- VR is made of thousands of different molecules and is characterised by a variety of different functional groups.

- Heavy atoms like metals or sulphur are commonly found in VR. Bonds which are made of these atoms involve a higher amount of electrons, and therefore have a more diffuse electron clouds which can undergo distortion more easily. As a result, the effects of the Van der Waals forces are even more important in molecules containing these kinds of atoms.
- Hydrogen bonding will also occurs in VR as nitrogen and metals are relatively electronegative atoms. This other intermolecular phenomenon has dramatic effects on the Raman spectra in terms of intensities and frequencies. The electronegative atoms attract the electron clouds of the atoms linked to the hydrogen and therefore induce a polar moment. These specific bonds involved in hydrogen bonding will stretch at a lower frequency and bend at higher wavelengths.
- Fermi resonance is also another environmental phenomenon which modifies the intensities and frequencies of the peaks.
- VR is a highly fluorescent compound, which makes the analysis even more difficult. Additionally, high intensity fluctuations of more than 20,000 units and signal saturation are common when working with VR. Such fluctuations represent a third of the spectrometer saturation intensity.

Elimination of fluorescence can be achieved using mathematical algorithms. Previous work identified and tested the airPLS algorithm on common solvents (12), (71). The same technique was used to eliminate background noise in the VR signal. Figure 4-44 presents the Raman spectrum of VR after removing the fluorescence.

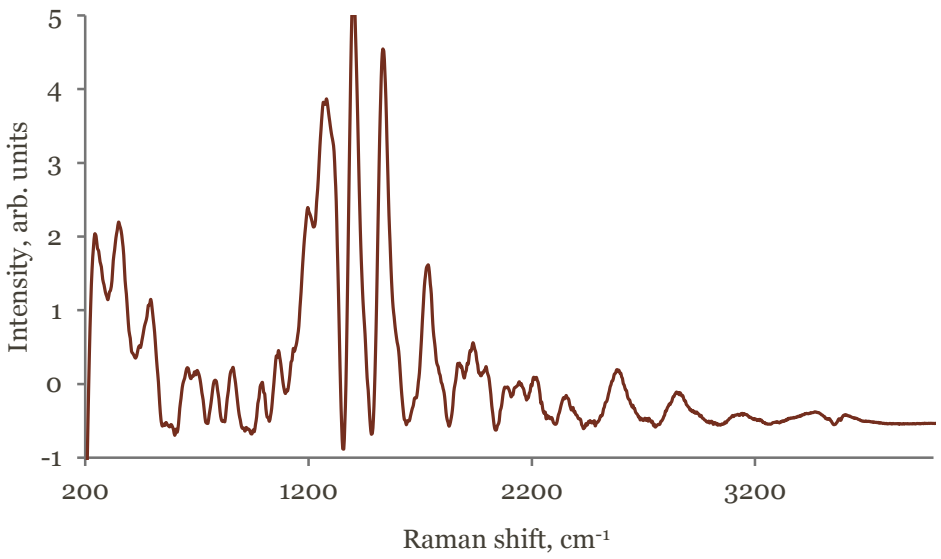

Figure 4-43: Raman spectrum of Athabasca VR after removing the fluorescence with the airPLS algorithm.

The presence of numerous, wide and large peaks, which result from the overlapping and interactions of many vibrational modes, testifies the complexity of VR. Although not carried out in this project, identification and assignments of these bands is possible with the use of PCA techniques. As mentioned previously, such methods were not used in this project due to time constraints.

The noticeable bands in the raw Raman spectrum presented in Figure 4-42 are still observable in the processed spectrum shown in Figure 4-43, with a spectral matching of ± 5cm^{-1}. Although such proximity verifies the accuracy and reliability of the airPLS algorithm, the rest of this study will use raw Raman spectra for the purpose of authenticity.

The Raman signals of diluted solutions of VR in toluene are easier to study than the Raman spectrum of pure VR. Section 4.4.2 uses the intensity ratio method on diluted solutions of VR in toluene.

4.4.2. Raman spectra of the dilutions and tentative of peak assignment

As mentioned in the introduction, crude oil can be diluted in naphtha in order to be shipped to another location. In order to extract information from raw signals of such complex systems, the implementation of analytical tools for the observation of interface phenomena was previously carried out by working with well-defined systems. This section describes the use of the intensity ratio study method applied to solutions of VR in toluene.

Figure 4-44 shows nine averaged spectra corresponding to different concentrations of VR in toluene. These spectra were acquired during the first observation date and are averaged over 20 spectra. The spectra corresponding to the second and third observation dates are presented in the annexe E.

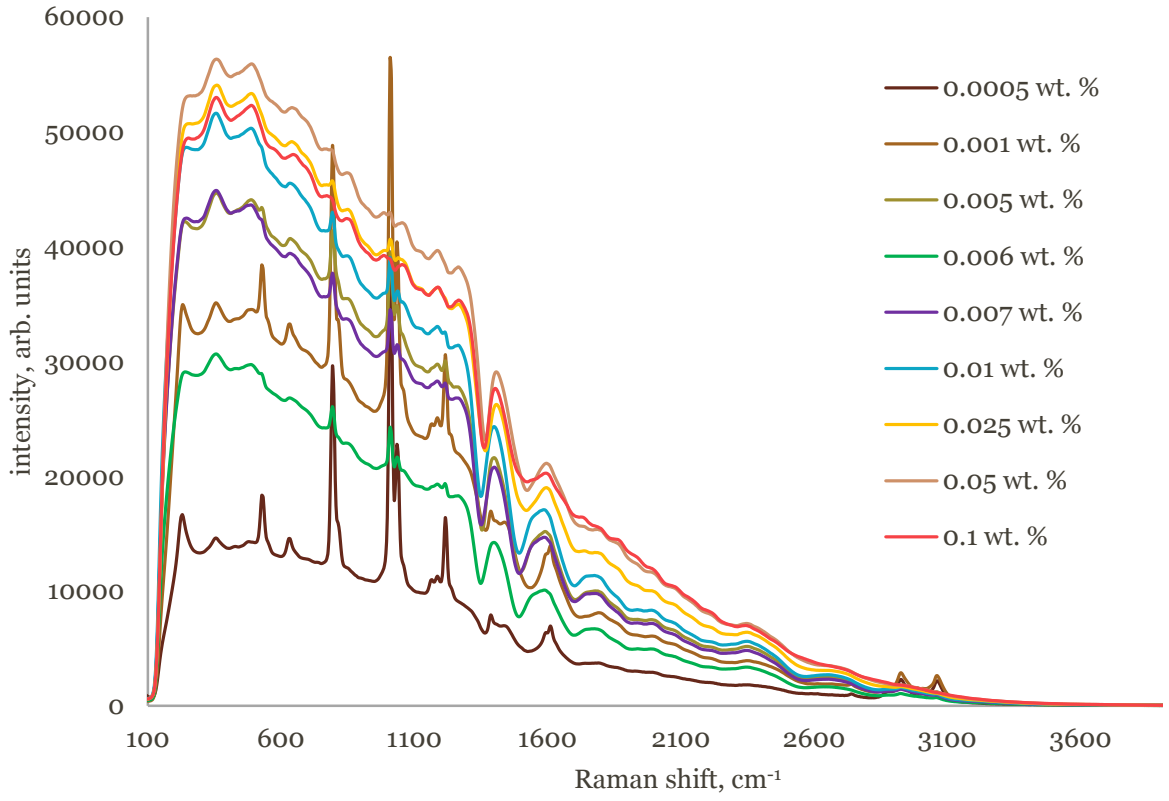

Figure 4-44: Average spectra for each concentration of VR in toluene obtained in the third set

Low concentrated solutions of VR in toluene (below 0.006 wt. %) present some features characteristic of pure toluene. Frequencies at 527 cm^{-1}, 793 cm^{-1}, 1009 cm^{-1}, 1035 cm^{-1} and 1216 cm^{-1}, which are observable for low concentrations of VR in toluene are likely to reflect the

vibrational modes of toluene as the frequency difference with the solvent are lower than 5 cm^{-1}. Table 4-11 reports the frequencies of these bands for each solution of VR in toluene and compares them with the vibrational frequencies of pure toluene.

Table 4-11: Raman frequencies of toluene-related bands in solutions of VR in toluene and comparison with the Raman frequencies of pure toluene

Solutions of VR in toluene							***pure toluene***				***Assignment***
0.0005-0.005 wt.%	***0.006 wt. %***	***0.007 wt.%***	***0.01 wt. %***	***0.025 wt.%***	***0.05 wt. %***	***0.1 wt.%***	***This work***	(80)	(100)	(77)	
527	*527*	-	-	-	-	-	*527*	*521*	*521*	*520*	*Ring deformation*
792.77	*793*	*793*	*793*	*793*	-	-	*792.77*	*786*	*786*	*784*	*Ring deformation*
1009	*1009*	*1009*	*1009*	*1009*	*1009*	-	*1009*	*1004*	*1004*	*1003*	*Ring breathing- C-C stretch*
1035	*1035*	*1035*	*1040*	*1040*	*1050-1055*	*1055*	*1035*	*1030*	*1030*	*1030*	*C-C stretch*
1216	*1216*	*1216*	*1216-1211*	-	-	-	*1216*	*1208*	*1212*	*1210*	*C-methyl stretch*
1386.5	*1396*	*1401*	*1401*	*1410.4*	*1410.4-1406*	*1406*	*1386.5*				*CH_3 bending*
1434	-	-	-	-	-	-	*1434*	*1436*		*1460*	*Methyl deformation*
1611	-	-	-	-	-	-	*1611*	*1585*		*1605*	*C-C valence*
2878-2882	*2878-2882*	*2878-2882*	*2871-2882*	-	-	-	*2878*	*2870*			*CH_3 stretching*
2926	*2922.46-2926*	*2926-2929*	*2926*	*2926-2929*	*2926-2929*	-	*2926*	*2920*		*2921*	*Methyl valence*
							3062	*3056*		*3055*	*CH stretching*

At concentrations of VR higher or equal to 0.006 wt. %, some bands characteristic of toluene start to fade away and new bands at 354.5 cm^{-1}, 487 cm^{-1}, 1186 cm^{-1}, 1260 cm^{-1}, 1410 cm^{-1} and 1596 cm^{-1} arise and get more intense as the concentration of VR increases. The absence of these bands in the Raman spectrum of pure toluene suggests that they probably result from the overlapping of both toluene and VR modes. Comparing the intensity of these new frequencies with the ones of toluene might give information about the physical behaviour of VR in toluene.

4.4.3. Intensity study

As shown in Figure 4-44, the background intensity increases as the concentration of VR in toluene increases, except for solutions around 0.005- 0.01 wt. %, which have a lower intensity. The intensities were plotted *versus* the concentration of VR and the three different graphs corresponding to three different dates were analysed. Although they are not represented in this section, no major differences were observed between the three observation dates, except some intensity variations, which are to be expected when working with such complex samples. As such, the age of the dilution does not seem to play a major role and the averages over the three dates for the band at 354.5 cm^{-1} and 487 cm^{-1} were calculated and plotted in Figure 4-45.

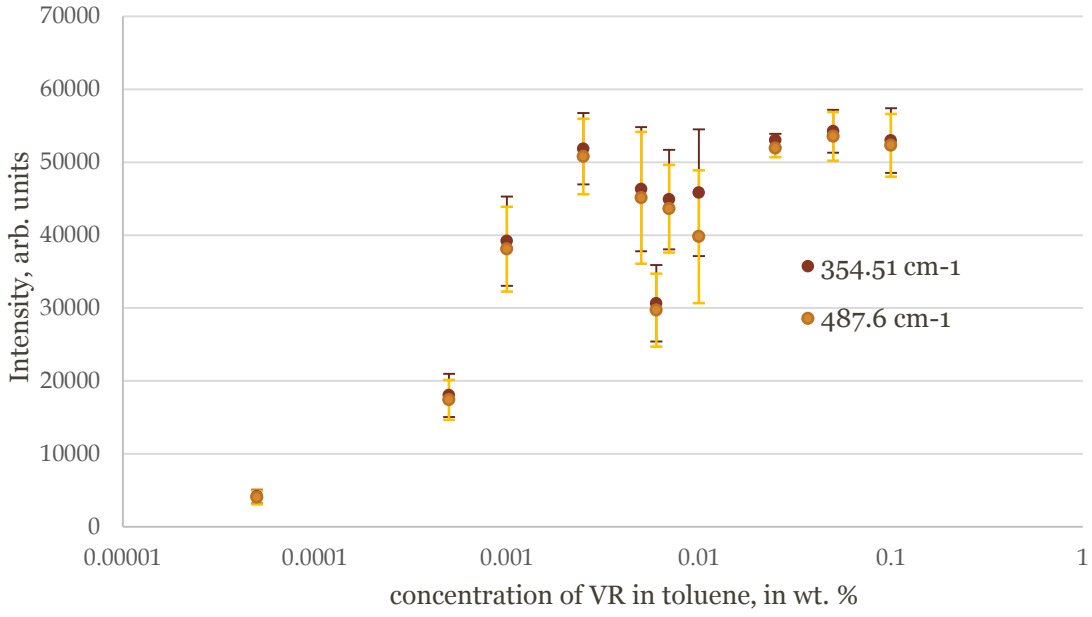

Figure 4-45: Intensity of the bands at 354.51 cm^{-1} and 487 cm^{-1} *versus* the concentration of VR in toluene. The error bars represent the standard deviation

4.4.4. Intensity ratio study

The intensities of different peaks were measured and plotted *versus* the concentration of VR in toluene. Figures 4-46 and 4-47 illustrate the evolution of four intensity ratios, three of them representing the contribution of VR to the spectrum of toluene. Since the age of the dilutions or temperature tested do not have a noticeable influence on the Raman spectrum, the acquisitions over the three observation dates were averaged for each concentration. Figures 4-46 and 4-47 represent the evolution of four intensity ratios average over nearly 60 spectra.

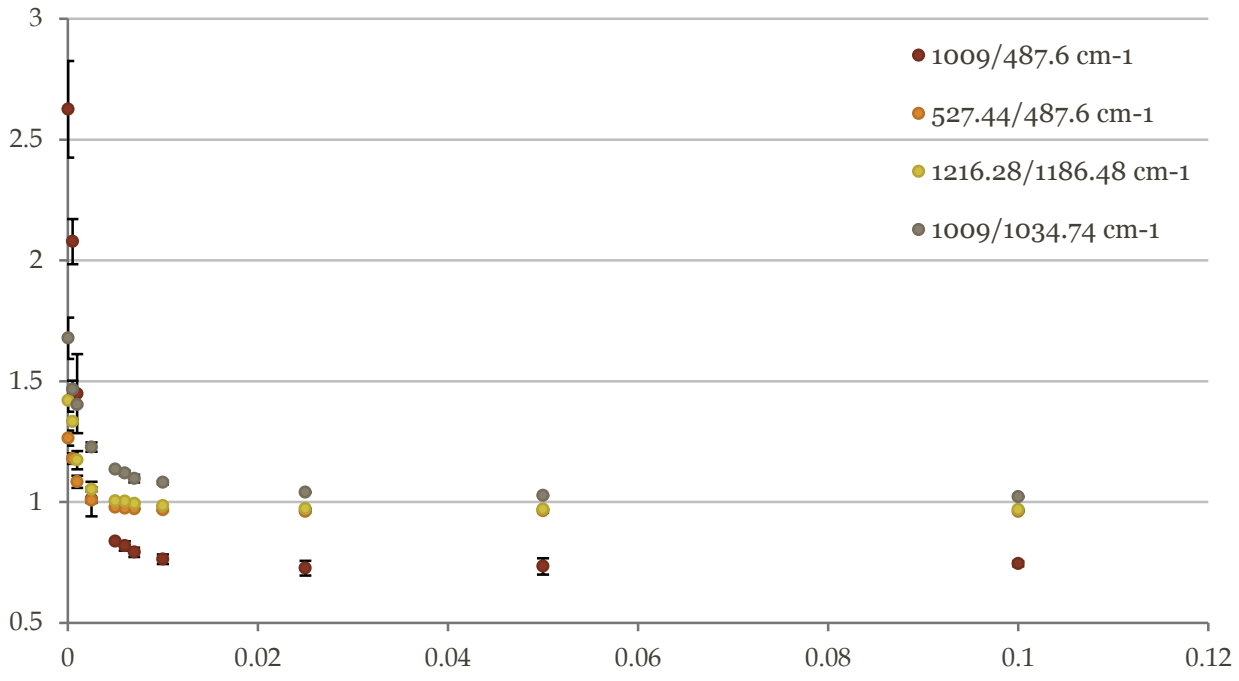

Figure 4-46: Intensity ratios as a function of the VR concentration in toluene. The data represents the average over the three observation dates (over 60 spectra) and the error bars represent the standard deviation over 60 acquisitions.

Figure 4-47 represents the same ratios as in Figure 4-46 but on a logarithmic scale.

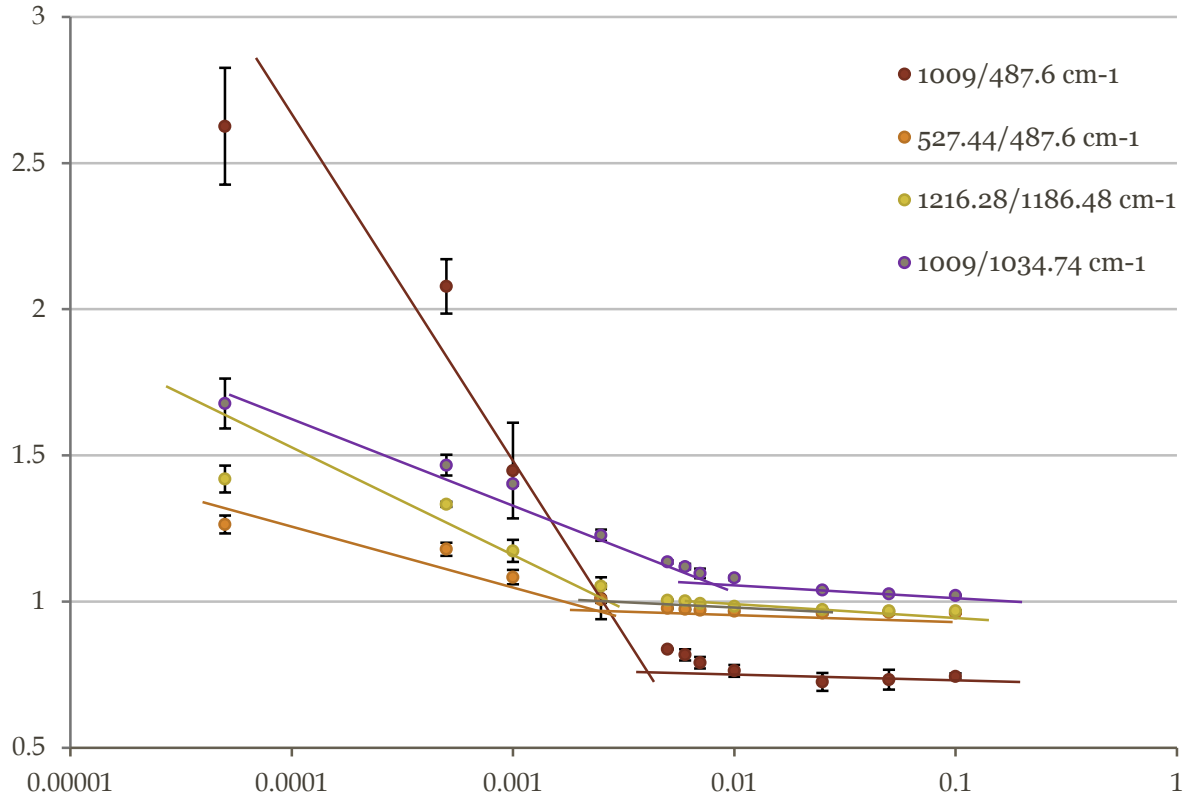

Figure 4-47: Intensity ratios as functions of the VR concentration in toluene observed with a logarithmic scale. The error bars represent the standard deviation over the 60 acquisitions

All four intensity ratios show a net decrease around 0.0025-0.008 wt. %, before reaching a constant value at higher concentration of VR. The breakpoints are observable in Figure 4-47 and reported in Table 4-12:

Table 4-12: Critical aggregation concentrations for asphaltenes in toluene calculated from the intensity ratio method

intensity ratio (cm^{-1})	I(1009)/I(1035)	I(1216)/I(1186)	I(527)/I(487)	I(1009)/I(487)
Breakpoint conc. (wt. %)	~0.008	~0.0025	~0.0025	~0.005
Breakpoint conc. (mg/L)	~69	~22	~22	~43

The breakpoint concentrations reported in Table 4-12 for four of the intensity ratios are in the range 22-70 mg/L, which is in good agreement with the CNAC provided in the literature and reported in Table 2-4. Since the four intensity ratios illustrate different regions of the asphaltene

molecules, the breakpoints do not correspond to the same concentrations. I(1009)/I(487), I(527)/I(487) and I(1216)/I(1186) represent the intensity fraction of toluene to VR whereas I(1009)/I(1035) is the fraction of two toluene intensity bands. During the early stage of asphaltene aggregation, the porosity of asphaltene is high enough to enable solvent access. By being trapped inside the complex structure, the solvent molecules are not able to move as easily and some vibrations such as ring breathing at 1009 cm^{-1} or ring deformation at 527 cm^{-1} are hindered, accounting for the decrease of I(1009)/I(487) and I(527)/I(487) at low concentrated solutions of VR in toluene. According to Figures 4-46 and 4-47, the intensity ratios remain relatively constant at concentrations of VR higher than 0.025 wt. %. Considering this, it can be suggested that the intensity of the ring breathing or stretching vibrations become constant at high concentrations of VR in toluene. This is in agreement with the idea of a step-wise mechanism for asphaltene aggregation, where the size of the asphaltene aggregates, and the size of the channels, become constant after a certain point.

4.4.5. Microemulsions of water in oil: water/asphaltenes /toluene ternary system

VR/water/toluene microemulsions were prepared and their Raman spectra were acquired, similarly to AOT/water/isooctane microemulsions. Only three concentrations of VR in toluene, 0.001 wt. %, 0.0025 wt. %, 0.005 wt. %, were prepared in this experiment. Higher concentrations of VR exhibit too much fluorescence and the high intensity peaks of VR cover toluene peaks. Figure 4-48 illustrates the different Raman spectra of VR/water/toluene microemulsions for a concentration in VR of 0.001 wt. %. The spectra corresponding to concentrations of 0.0025 wt. % and 0.005 wt. % are presented in the annexe F.

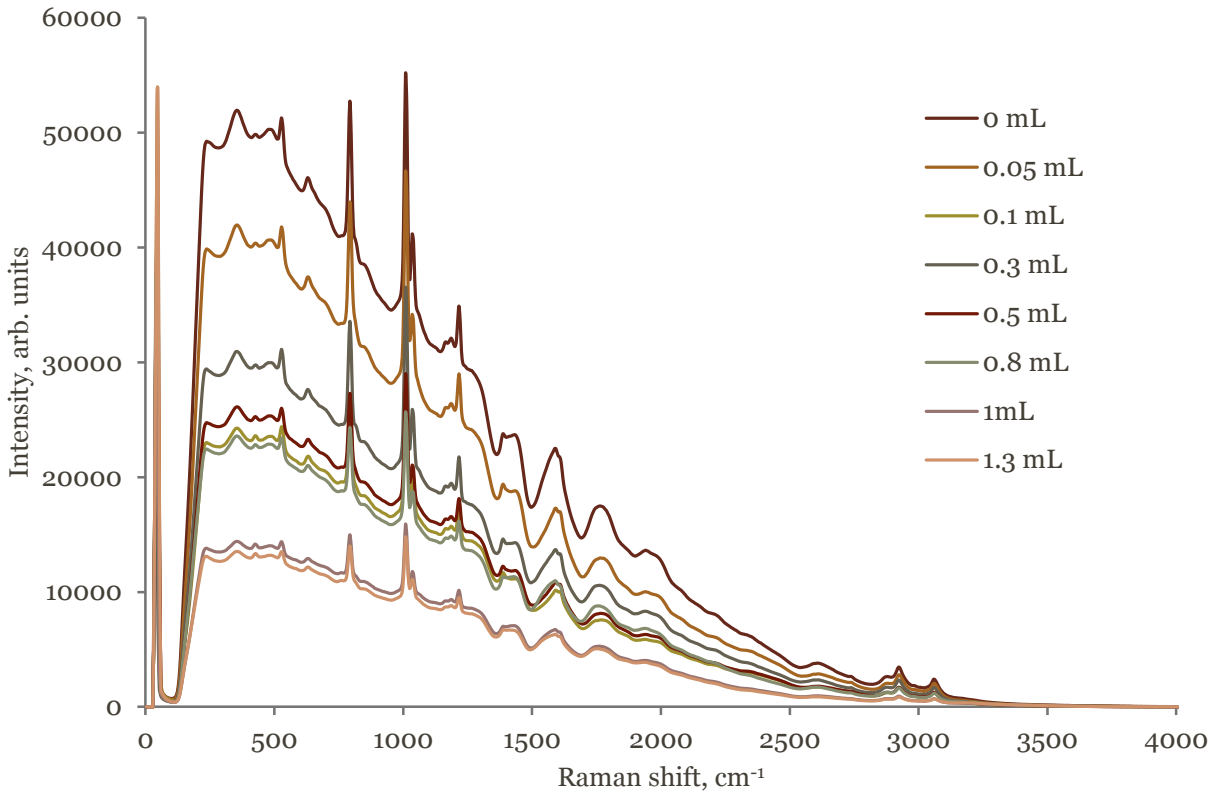

Figure 4-48: Raman spectra of the VR/water/toluene for different volume of water added. The microemulsions were prepared from a 0.001 wt. % solution of VR in toluene.

As illustrated in Figure 4-48, the overall intensity of the spectrum decreases as the amount of water inside the system increases. Normalisation to certain frequencies were applied to adjust the intensity scale and investigate changes between the different spectra. Figure 4-49 and Figure 4-50 illustrate specific regions of the Raman spectra presented in Figure 4-48, after normalisation.

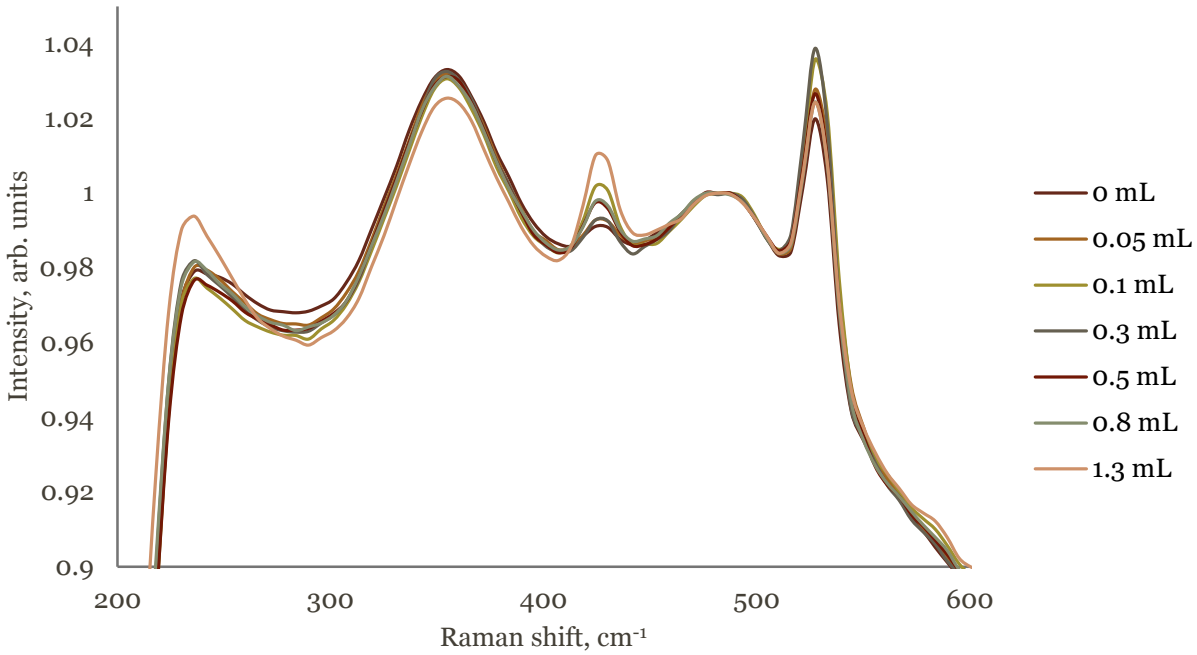

Figure 4-49: Raman spectra of VR/water/toluene microemulsions in the 600-200 cm^{-1} region. The microemulsions were prepared in a solution of 0.001 wt. % VR in toluene.

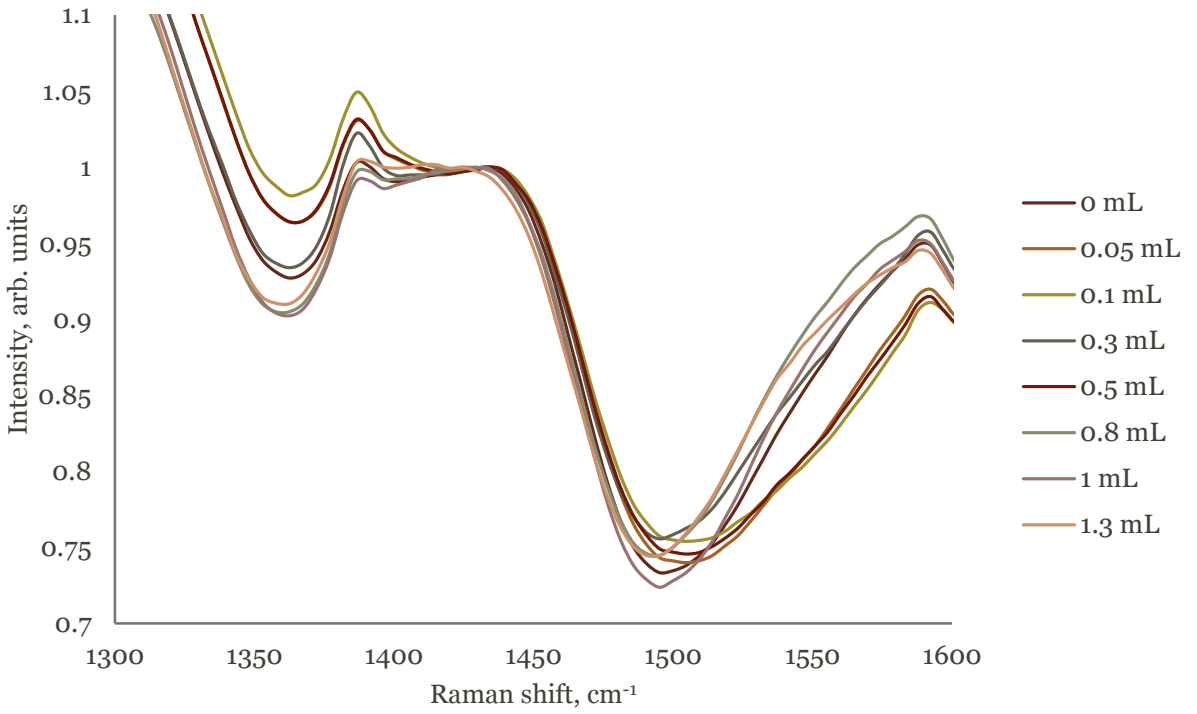

Figure 4-50: Raman spectra of VR/water/toluene microemulsions in the 1600-1300 cm^{-1} region. The microemulsions were prepared in a solution of 0.001 wt. % VR in toluene.

Microemulsions prepared from a solution of 0.0025 wt. % VR in toluene show similar trends as in Figure 4-49 and Figure 4-50 but microemulsions with 0.005 wt. % VR in toluene do not show significant variations after normalisation. Although peak intensity changes are noticeable in the Raman signals of 0.001 wt. % and 0.0025 wt. % microemulsions, no conclusion could be made because the variations do not have repeatable trends and peak assignment was challenging. Nevertheless, it is apparent that microemulsions of VR/water/toluene do not behave as surfactants microemulsions, as described in section 4.3.4. Asphaltenes are composed of many sites, different in nature and structure, as illustrated by Figure 2-13. The interactions modes are therefore higher and more complex than in the surfactant model. The model of surfactant microemulsions is not adapted to represent the interactions of asphaltenes in microemuslions and as such, will be discarded.

5. Conclusions and Recommendations

5.1. Conclusions

This project sets out to study the self-association of surfactants in water and heavy oil components in organic solvents with the *in-situ* analytical tools. Intensity and frequency studies were carried out to determine the micellization onset of surfactant compounds. Only the intensity ratio method was selected for the study of VR as it resulted in less errors and uncertainties than the frequency study. Additionally, the robustness of the intensity ratio method was verified by adding salt to aqueous solutions of SDS. Shifts of the breakpoints towards lower values of SDS concentrations were observed as the concentration of salt increased, which is in agreement with the literature. The same intensity method was then applied to more complex associating systems. The evolution of certain VR to toluene intensity ratios showed similar evolutions as in the surfactant studies and the breakpoints were attributed to the early stages of asphaltenes aggregation in toluene, also noted CNAC. As the intensity ratios studied represent different parts of the molecules and different environments, they illustrate different stages of the aggregation process, explaining why the breakpoints are not sharp transitions and why they correspond to different concentrations. Although the surfactant model worked well to study the early stages of VR aggregation in toluene, it was incomplete and not accurate enough to understand the VR microemulsions.

The analytical tools developed in this project can be applied to various scientific fields. The use of surfactants in membrane protein is an expanding technique to isolate, crystallise and reconstitute proteins in the organism. Understanding and mimicking the role and function of the different proteins in the human body is the first step toward the development of drugs. The formation of protein-detergent complexes at concentrations of surfactant above the CMC can be analysed using Raman spectroscopy.

Moreover, surfactants are widely used as additives in paint in order to improve the mechanical stability of the paint and to prevent cracking or scaling. They are also used as wetting agents that allow better spreading of the paint and as dispersive additives which prevent the agglomeration of pigments by adsorbing on their surfaces. Additionally, the addition of surfactants stabilize the microemulsions in latex paint by forming micelles around polymers. All of these processes occur at concentrations higher than the CMC. The use of Raman spectroscopy and intensity ratios might also be a valuable method to give an insight of the different mechanisms.

Surfactants are also used in food and pharmaceutical industry as foaming and emulsifying agents. As an example, they have many applications in food washing, fermentation processes and food preservation. The ability of certain surfactants such as SDS to form mixed micelles with food additives such as salicylic acid is commonly employed to solubilize these substances in food. The observation of mixed micelles between SDS and a wide range of food additives with Raman spectroscopy might give more accurate information on the onset of this process.

Intensity studies of petroleum solutions using Raman spectroscopy have also many applications in the oil industry. Such concept can be applied to approach flow assurance issues in pipelines. In order to ensure good flows of hydrocarbon mixtures inside the pipelines and prevent precipitation and sedimentation of particles, in-situ analytical tools can be developed to monitor the flow parameters at anytime. The precipitation of asphaltenes is dependent on the pressure, the temperature and the flow debit. In addition to the pressure and temperature sensors installed inside the pipelines, the implementation of an in-situ Raman spectrometer could be an effective method to determine the presence of asphaltene nanoaggregates using intensity variations.

5.2. Recommendations

Several improvements are recommended for future work:

- Selecting model compounds which have multiple modes of interactions and self-assemble in a step-wise mechanism. Investigation the aggregation of dyes with the Raman spectroscopy might give additional analytical tools to study the asphaltene self-association in organic solvents.
- The VR microemulsions experiments illustrated in this thesis were not conclusive and the interactions between water and asphaltenes need to be further investigated. Once again, it would be interesting to study the influence of water on dye aggregation.
- Using the Principal Component analysis to study the chemical composition of VR and asphaltenes. Identifying the functional groups characteristic of asphaltenes might help to understand how such compounds interact.
- Using Raman microscopy as a complementary method. Raman microscopy gives information about the distribution of particles within the cell.

Bibliography

1. **International Energy Agency.** *Medium-Term Market Report 2015- Market Analysis and Forecasts to 2020.* s.l. : IEA, 2015.

2. **Speight, James G.** *Chemistry and Technology of Petroleum, Fifth Edition.* s.l. : CRC Press, 2014.

3. **Ancheyta, Jorge and Speight, James G.** *Hydroprocessing of Heavy Oils and Residua.* Boca Raton : CRC Press, 2007.

4. **Canada's Oil and Natural Gas Producers.** *2015 CAPP Crude Oil Forecast, Markets & Transportation.* Calgary : Canadian Association of Petroleum Producers, 2015.

5. **Gray, Murray R.** *Upgrading Oilsands Bitumen and Heavy Oil.* Edmonton : The University of Alberta Press, 2015.

6. *Aggregation of Asphaltenes Obtained From a Brazilian Crude Oil in Aromatic Solvents.* **Loh, Watson, Mohamed, Rahoma S. and Ramos, Antonio C. S.** s.l. : Petroleum Science and Technology, 1999, Vol. 17, pp. 147-163.

7. *Aggregation of Asphaltenes as Determined by Calorimetry.* **Andersen, Simon Ivar and Birdi, Kulbir S.** 2, s.l. : Journal of Colloid and Interface Science, 1991, Vol. 142, pp. 497-502.

8. *The Critical Micelle Concentration of Asphaltenes As Measured by Calorimetry.* **Andersen, Simon Ivar and Christensen, Steen D.** s.l. : Energy&Fuels, 2000, Vol. 14, pp. 38-42.

9. *High-Q Ultrasonic Determination of the Critical Nanoaggregate Concentration of Asphaltenes and the Critical Micelle Concentration of Standard Surfactants.* **Andreatta, Gaelle, Bostrom, Neil and Mullins, Oliver C.** s.l. : Langmuir, 2005, Vol. 21, pp. 2728-2736.

10. *Absorbance and fluorescence spectroscopy on the aggregaton behaviour of asphaltene-toluene solutions.* **Goncalves, S., et al.** 2004, Fuel, Vol. 83, pp. 1823-1828.

11. *Thermo-optical studies of asphaltene solutions: evidence for solvent-solute aggregate formation.* **Acevedo, S., et al.** 1999, Fuel, Vol. 78, pp. 997-1003.

12. **Khalili, Khaled.** *Development, Implementation and Validation Of In-Situ Raman Hot Stage Reactor.* Edmonton : Department of Chemical & Material Engineering, University of Alberta, 2014.

13. **Ferraro, John R., Nakamoto, Kazuo and Brown, Chris W.** *Introductory Raman Spectroscopy-Second Edition.* s.l. : Elsevier Science, 2003.

14. **Larkin, Peter.** Infrared and Raman Spectroscop: Principles and Spectral Interpretation. *Infrared and Raman Spectroscopy.* Oxford : Elsevier, 2011, pp. 135-176.

15. **Smith, Ewen and Dent, Geoffrey.** *Modern Raman Spectroscopy- A Practical Approach, Ch1.* Chichester, West Sussex, England : Wiley & Sons Ltd., 2005.

16. *The Raman Spectrum of Bromine.* **Stammreich, H.** 79, 1950, Physical Review Letters, Vol. 78, pp. 79-80.

17. **Colthup, Norman B., Daly, Lawrence H. and Wiberley, Stephen E.** *Introduction to Infrared and Raman Spectroscopy, second edition.* New York : Academic Press, Inc., 1975.

18. **Mayo, Dana W., Miller, Foil A. and Hannah, Robert W.** *Course Notes on the Interpretation of Infrared and Raman Spectra Ch1.* Hoboken, New Jersey : John Wiley & Sons, 2004.

19. *Raman characteristics of hydrocarbon and hydrocarbon inclusions.* **Zhang, Nai, et al.** 8, s.l. : Sci China Ser D-Earth Sci, 2007, Science in China Press, Vol. 50, pp. 1171-1178.

20. *Raman Cross Sections of Selected Hydrocarbons and Freons.* **Stephenson, David A.** Warren : Journal of Quantitative Spectroscopy& Radiative Transfer, 1974, Vol. 14, pp. 1291-1301.

21. **Dollish, Francis R., Fateley, William G. and Bentley, Freeman F.** *Characteristic Raman Frequencies of Organic Compounds.* New York : John Wiley and Sons, 1974.

22. *The Excess Volume of Binary Mixtures of trans-Decalin with Cyclohexane and with n-Alkanes.* **Gomez-Ibanez, Jose and Wang, Tieh Chu.** 2, 1966, The Journal of Physical Chemistry, Vol. 70, pp. 391-395.

23. *Excess Thermodynamic Functions of n-Hexane+ Toluene: Application of Flory's Theory.* **Malakondaiah, K., Subbarangaiah, K. and Subrahmanyam, S. V.** 1991, Physics and Chemistry of Liquids, Vol. 23, pp. 49-56.

24. *Raman Spectroscopy of Crude Oils and Hydrocarbon Fluid Inclusions: A Feasibility Study.* **Orange, Daniel, et al.** Santa Cruz : Mineral Spectroscopy : A Tribute to Roger G.Burns, Geochem. Soc., 1996, Vol. 5, pp. 65-81.

25. **Kubitscheck, Ulrich.** Introduction to Optics and Photophysics. [book auth.] Kubitscheck Ulrich. *Fluorescence Microscopy: from Principles to Biological Applications.* s.l. : Wiley , 2013.

26. *Photobleaching of Fluorescent Dyes under Conditions Used for Single-Molecule Detection: Evidence of Two-Steps Photolysis.* **Eggeling, C., et al.** s.l. : Anal. Chem., 1998, Vol. 70, pp. 2651-2659.

27. **Hansen, Susanne Brunsgaard.** *The Application of Raman Spectroscopy for Analysis of Multi-Component Systems.* Lyngby, Denmark : s.n., 2000.

28. *Raman Spectroscopy of Carbon and Solid Bitumens in Sedimentary and Metamorphic Rocks.* **Jehlicka, Jan, Ondrej, Urban and Pokorny, jan.** Prague : Spectrochimica Acta Part A, 2003, Vol. 59, pp. 2341-2352.

29. *Some Correlating Principles of Detergent Action.* **Presto, Walter C. and Preston, Walter.** 1948, Journal of Physical Chemistry, Vol. 52, pp. 84-97.

30. *Fluorophotometric determination of critical micelle concentration (CMC) of ionic and non-ionic surfactants with carbon dots via Stokes shift.* **Bhaisare, Mukesh Lavkush, et al.** 2015, Talanta, Vol. 132, pp. 572-578.

31. *Effect of electrolytes on the physiochemical behaviour of sodium dodecyl sulphate micelles.* **Dutkiewicz, E. and Jakubowska, A.** 2002, Colloid and Polymer Science, Vol. 280, pp. 1009-1014.

32. *Ionic liquids effect on critical micelle concentration of SDS: Conductivity, fluorescence and NMR studies.* **Pal, Amalendu and Chaudhary, Sheena.** 2014, Fluid Phase Equilibria, Vol. 372, pp. 100-104.

33. *Raman spectroscopy of micellization-induced liquid–liquid fluctuations in sodium dodecyl sulfate aqueous solution.* **Dolenko, Tatiana A.; Burikov, Sergey A.; Dolenko, Sergey A.; Efitorov, Alexander O.; Yuriy, A.** 2015, Journal of Molecular Liquids, Vol. 204, pp. 44-49.

34. *Study of the Vibrational Characteristics of Aerosol OT by Laser Raman Spectroscopy.* **Maitra, Amarnath and Kumarjain, Tanoj.** 1987, Colloids and Surfaces, Vol. 28, pp. 19-27.

35. *Vibrational Mode Behavior of SDS Aqueous Solutions Studied by Raman Scattering.* **Picquart, Michel.** 1986, Journal of Physical Chemistry, Vol. 90, pp. 243-250.

36. *Thermodynamics of Micellization of Aerosol OT in Polar and Nonpolar Solvents. A Calorimetric Study.* **Mukherjee, Kallol and Moulik, S.P.** 1993, Langmuir, Vol. 9, pp. 1727-1730.

37. *Solution behaviour of Aerosol OT in non-polar solvents.* **Tapas, De K. and Maitra, Amarnath.** 1995, Adv. Colloid Inteface Sci., Vol. 59, pp. 95-193.

38. *Evidence for a Critical Micelle Concentration of Surfactants in Hydrocarbon Solvents.* **Smith, Gregory N., et al.** 2013, Langmuir, Vol. 29, pp. 3252-3258.

39. *Vibrational Spectroscopic Study of the Structure of Sodium Bis(2-ethylhexyl) sulfosuccinate Reverse Micelles and Water-in-Oil Microemulsions.* **Moran, Paul D., Bowmaker, Graham A. and Cooney, Ralph P.** 3, 1995, Langmuir, Vol. 11, pp. 738-743.

40. *Formation of AOT Reversed Micelles and W/O Microemulsions.* **Kawai, Takeshi, et al.** 1992, Bull.Chem.Soc.Jpn., Vol. 65, pp. 2715-2719.

41. *Structural Studies of Aoerosol OT Reverse Micellar Aggregates by FT-IR Spectroscopy.* **Jain, Tanoj Kumar, Varshney, Manoj and Maitra, Amarnath.** 1989, Journal of Physical Chemistry, Vol. 93, pp. 7409-7416.

42. *Comparative study on structure of solubilized water in reversed micelles. 1. FT-IR spectroscopic evidence of water/AOT/n-Heptane systems.* **Li, Quan, et al.** 1998, Journal of Physical Chemistry, Vol. 102, pp. 3168-3174.

43. *Macrostructures of the asphaltic fractions by various instrumental methods.* **Dickie, J. P. and Yen, T. F.** 1967, Analytic Chemistry, Vol. 39, pp. 1847-1852.

44. *Interaction and Solubilization of Water by Petroleum Asphaltenes in Organic Solution.* **Andersen, Simon Ivar, et al.** 2001, Langmuir, Vol. 17, pp. 307-313.

45. **Mullins, Oliver C., et al.** *Asphaltenes, Heavy Oils and Petroleomics.* New York : Springer, 2010.

46. *Molecular Size and structure of Asphaltene from Various Sources.* **Groenzin, Henning and Mullins, Oliver C.** 2000, Energy and Fuel, Vol. 14, pp. 677-684.

47. *The Modified Yen Model.* **Mullins, Oliver C.** 2010, Energy&Fuels, Vol. 24, pp. 2179-2207.

48. *Discussion on the Structural Features of Asphaltene Molecules.* **Liao, Z., et al.** 2009, Energy Fuels, Vol. 12, pp. 6272-6274.

49. *Quantitative Evidence of Bridged Structures in Asphaltenes by Thin Pyrolysis.* **Karimi, A., et al.** 8, 2011, Energy & Fuels, Vol. 25, pp. 3581-3589.

50. *Quantitative Molecular Representation and Sequential Optimization of Athabasca Asphaltenes.* **Sheremata, Jeff M., et al.** Edmonton : Energy&Fuels, 2004, Vol. 18, pp. 1377-1384.

51. *Asphaltic bitumen as a colloid system.* **Pfeiffer, J. P. and Saal, R. N. J.** 1940, Journal of Physical Chemistry, Vol. 44, pp. 139-145.

52. *Aggregation and kinetics of asphaltenes in organic solvents.* **Sheu, Eric Y., et al.** s.l. : Fuel, Vol. 71, pp. 299-302.

53. *Calorimetric Evidence about the Application of the Concept of CMC to Asphaltene Self-Association.* **Merino-Garcia, Daniel and Andersen, Simon I.** Denmark : s.n., 2005, Journal of Dispersion Science and Technology, Vol. 26, pp. 217-225.

54. *Molecular Mechanics and Microcalorimetric Investigations of the Effects of Molecular Water on the Aggregation of Asphaltenes in Solutions.* **Murgich, Juan, et al.** 2002, Langmuir, Vol. 18, pp. 9080-9086.

55. **Murgich, Juan.** Intermolecular Forces in Aggregates of Asphaltenes and Resins. *Petroleum Science and Technology.* 2002, Vol. 20, 9&10, pp. 983-997.

56. *Molecular Mechanics of Aggregates of Asphaltenes and Resins of the Athabasca Oil.* **Murgich, Juan and Strausz, Otto P.** 1&2, 2001, Petroleum Science and Technology, Vol. 19, pp. 231-243.

57. *Effect of Asphaltene Structure on Association and Aggregation Using Molecular Dynamics.* **Sedghi, Mohammad, et al.** 2013, The Journal of Physical Chemistry, Vol. 117, pp. 5765-5776.

58. *Molecular Recgnition and Molecular Mechanics of Micelles of Some Model Asphaltenes and Resins.* **Murgich, Juan, Rodriguez, Jesus M. and Aray, Yosslen.** 1996, Energy & Fuels, Vol. 10, pp. 68-76.

59. *Molecular Simulation and the Aggregation of the Heavy Fractions in Crude Oils.* **Murgich, J.** 2003, Molecular Simulation, Vol. 29, pp. 451-461.

60. *Simulation of Interactions in Asphaltene Aggregates.* **Rogel, Estrella.** 2000, Energy&Fuels, Vol. 14, pp. 566-574.

61. *Effect on Molecular Interactions of Chemical Alteration of Petroleum Asphaltenes.* **Juyal, P., Merino-Garcia, D. and Andersen, S. I.** Denmark : s.n., 2005, Energy & Fuels, Vol. 19, pp. 1272-1281.

62. *Supramolecular Assembly Model for Aggregation of Petroleum Asphaltenes.* **Gray, Murray R., et al.** Edmonton : s.n., 2011, Energy&Fuels, Vol. 25, pp. 3125-3134.

63. *Initial stages of asphaltene aggregation in dilute crude oil solutions: studies of viscosity and NMR relaxation.* **Evdokimov, Igor N., Eliseev, Nikolay Yu. and Akhmetov, Bulat R.** 2003, Fuel, Vol. 82, pp. 817-823.

64. *Asphaltene aggregation in organic solvent.* **Oh, Kyeongseok, Ring, Terry A. and Milind, Deo D.** 2004, Journal of Colloid and Interface Science, Vol. 271, pp. 212-219.

65. **Huc, Alain-Yves Ed.** *Heavy Crude Oils: From Geology to Upgrading: an Overview.* s.l. : IFP Publications, 2010.

66. **Vandenabeele, Peter.** *Practical Raman Spectroscopy: an Introduction.* Chichester, West Susses, United Kingdom : Wiley, 2013.

67. **Schrader, Bernhard.** *Infrared and Raman Spectroscopy: Methods and Applications.* s.l. : Wiley, 1995.

68. **Lewis, Ian R. and Edwards, Howell.** *Handbook of Raman Spectroscopy: From the Research Laboratory to the Process Line.* s.l. : CRC Press, 2001.

69. *Phase Behaviour of Athabasca Bitumen.* **Bazyleva, A., et al.** 7, 2001, Chemical & Engineering Data, Vol. 56, pp. 3242-3253.

70. *Molecular Weight and Specific Gravity Distributions for Athabasca and Cold Lake Bitumens and Their Saturates, Aromatics, Resin and Asphaltene Fraction.* **Peramanu, S., Pruden, B. B. and Rahimi, P.** 8, 1999, Industrial & Engineering Chemistry, Vol. 36, pp. 3121-3130.

71. **Nicpon, Michal.** *In Situ Observation of Hydrodesulfurization of Heavy Oils and Bio Oils.* Edmonton : University of Alberta, 2013.

72. *Baseline Correction Using Adaptive Iteratively Reweighted Penalized Least Squares.* **Zhang, Zhi-Min, Chen, Shan and Liang, Yi-Zeng.** 2010, Royal Society of Chemistry, Vol. 135, pp. 1138-1146.

73. *An Intelligent Background-Correction Algorithm for Highly Fluorescent Samples in Raman Spectroscopy.* **Zhang, Zhi-Min, et al.** 6, s.l. : Journal of Raman Spectroscopy, 2010, Vol. 41, pp. 659-669.

74. *A New General-Purpose Fully Automatic Baseline-Correction Procedure for 1D and 2D NMR Data.* **Cobas, Carlos J., et al.** 2006, Journal of Magnetic Resonance, Vol. 183, pp. 145-151.

75. *The Raman Spectrum and the Structure of Water.* **Cross, Paul C., Burnham, John and Leighton, Philip A.** 6, 1937, Journal of the American Chemical Society, Vol. 59, pp. 1134-1147.

76. **Tanabe, K and Hiraishi, J.** *Spectral Data Base for Organic Compounds, SDBS.* [Online] [Cited: 11 18, 2015.] http://sdbs.db.aist.go.jp .

77. *Spectre infrarouge et attribution des vibrations des toluenes C6H5CH3,, C6H5CD3 et C6D5CD3, .* **Fuson, N., Garrigou-Lagrange, C. and Josien, M. L.** 1960, Spectrochimica Acta, Vol. 16, pp. 106-127.

78. **Smith, Brian C.** *Infrared Spectral Interpretation: A Systematic Approach.* s.l. : CRC Press, 1999.

79. *The Infrared and Raman Spectra of Cyclohexane and Cyclohexane-d12.* **Miller, Foil A. and Golob, Helen R.** Pittsburgh : s.n., 1964, Spectrochimica Acta, Vol. 20, pp. 1517-1530.

80. *The Infrared and Raman Spectra of Toluene, Toluene-a-d3, m-Xylene, and m-Xylene-aa'-d6.* **Wilmshurst, J. K. and Bernstein, H. J.** 1957, Canadian Journal of Chemistry, Vol. 35, pp. 911-925.

81. **Socrates, George.** *Infrared and Raman Characteristic Group Frequencies: Tables and Charts.* s.l. : John Wiley & Sons, 2001.

82. *Vibrational Spectral and Analysis of cis-Decahydronaphthalene.* **Mani, P. and Suresh, S.** 10, Padur, India : s.n., 2011, Asian Journal of Chemistry, Vol. 23, pp. 4299-4302.

83. *Spectroscopy of the C-H Stretching Vibrational Band in Selected Organic Molecules.* **Sebek, Jiri, et al.** 2013, Journal of Physical Chemistry, Vol. 117, pp. 7442-7452.

84. **Valmalette, Jean-Christophe, et al.** *Raman Scattering of Linear Chains of Strongly Coupled Ag Nanoparticles on SWCNTs.* s.l. : Nature, 2014.

85. *Study of the Adsorption of Sodium Dodecyl Sulfate (SDS) at the Air/Water Interface: Targeting the Sulfate Headgroup Using Vibrational Sum Frequency.* **Johnson, C. Magnus and Tyrode, Eric.** 2005, The Journal of Physical Chemistry, Vol. 7, pp. 2635-2640.

86. *On the Conformational State of Surfactants in the Solid State and in Micellar Form. A Laser-Excited Raman Scattering Study.* **Kalyanasundaram, K. and Thomas, J.K.** 13, 1973, The Journal of Physical Chemistry, Vol. 80, pp. 1462- 1473.

87. *Hydrocarbon Chain Conformations in Micelles. A Nuclear Magnetic Relaxation Study.* **Chevalier, yves and Chachaty, Claude.** 1985, Journal of Physical Chemistry, Vol. 89, pp. 875-880.

88. *An Investigation of Surfactant Behaviour at the Liquid/Liquid Interface with Sum-Frequency Vibrational Spectroscopy.* **Conboy, J. C., et al.** 1997, Progress in Colloid and Polymer Science, Vol. 103, pp. 10-20.

89. *Dependence of Alkyl Chain Conformation of Simple Ionic Surfactants on Head Group Functionality as Studied by Vibrational Sum-Frequency Spectroscopy.* **Conboy, John C., Messmer, Marie C. and Richmond, Geraldine L.** 1997, Journal of Physical Chemistry, Vol. 101, pp. 6724-6733.

90. *Conformational dependence of Raman Frequencies and Intensities in Alkanes and Polyethylene.* **Tarazona, Antulio, et al.** 1997, Vibrational Spectroscopy, Vol. 14, pp. 159-170.

91. **Luttschwager, Nils Olaf Bernd.** *Raman Spectroscopy of Conformational Rearrangements at Low Temperatures- Folding and Stretching of Alkanes in Supersonic Jets.* Germany : Springer, 2014.

92. *Conformational Dependences of the Raman Scattering Intensities from Polynucleotides. III. Order-Disorder Changes in Helical Structures.* **Small, Enoch W. and Peticolas, Warner L.** 8, Eugene, Oregon : John Wiley & Sons, 1971, Biopolymers, Vol. 10, pp. 1377-1416.

93. *Raman Intensities of Carbon-Carbon Stretching Modes in a Model Membrane.* **Susi, H., Byler, D. M. and Damert, W. C.** 1980, Chemistry and Physics of Lipids, Vol. 27, pp. 337-344.

94. *The Structures and Vibrational Frequencies of a Series of Alkanes Using the SPASIBA Force Field.* **Derreumaux, Philippe, Dauchez, Manuel and Vergoten, Gerard.** 1993, Journal of Molecular Structure, Vol. 295, pp. 203-221.

95. *Structure of a layer of AOT adsorbed at the air/liquid interface at the critical micelle concentration determined by neutron reflection.* **Li, Z. X., et al.** 1995, Progress in Colloid Polymer Science, Vol. 98, pp. 243-247.

96. *What is so special about Aerosol-OT? 1. Aqueous Systems.* **Nave, Sandrine and Eastoe, Julian.** 2000, Langmuir, Vol. 16, pp. 8733-8740.

97. *Effects of Hydrophilic and Hydrophobic Counterions on the Coulombic Interactions in Perfluorosulfonate Ionomers.* **Cable, Kevin M., Mauritz, Kenneth A. and Moore, Robert B.** 1995, Journal of Polymer Science: Part B: Polymer Physics, Vol. 33, pp. 1065-1072.

98. *A Fourier Transform Infrared Study of Water-Head Group Interactions in Reversed Micelles Containing Sodium Bis(2-ethylhexyl) sulfosuccinate (AOT).* **Christopher, David J., et al.** 2, 1992, Journal of Colloid and Interface Science, Vol. 152, pp. 465-472.

99. **Bakulin, Artem A., et al.** Dynamics of Water Confined in Reversed Micelles: Multidimensional Vibrational Spectroscopy Study. *American Chemical Society.* 49, 2013, Vol. 117, pp. 15545-15558.

100. *The methylbenzenes-I. Vapor-phase vibrational fundamentals, internal rotations and a modified valence force field.* **Draeger, J. A.** 4, 1985, Spectrochimica Acta, Vol. 41A, pp. 607-627.

101. *On the versatile surfactant Aerosol-OT (AOT): Its physiochemical and surface chemicals behaviours and uses.* **Mukherjee, K and Moulik, S.P.** 3, 1995, Proc.Indian natn.Sci.Acad., Vol. 62, pp. 215-232.

102. ***Eicke, H.F., et al.*** *1975, PHys. Chem., Vol. 79, p. 667.*

103. Water dynamics in large and small reverse micelles: From two ensembles to collective behaviour. ***Moilanen, David E., et al.*** *2009, The journal of Chemical Physics, Vol. 131, p. 014704.*

104. ***Gray, M. R.*** *Upgrading of Oil Sands Bitumen and Heavy Oil. Edmonton : s.n., 2010.*

105. Fourier Transform Infrared Investigation on Water States and the Conformations of Aerosol-OT in Reverse Microemulsions. ***Zhou, Guo-Wei, Li, Gan-Zuo and Chen, Wen-Jun.*** *2002, Langmuir, Vol. 18, pp. 4566-4571.*

106. Effect of Chemical Composition on Asphaltenes Aggregation. ***Durand, Emmanuelle, et al.*** *2010, Energy & Fuels, Vol. 24, pp. 1051-1062.*

107. Near Infrared Spectroscopy: fundamentals, practical aspects and analytical applications. ***Pasquini, Celio.*** *2, Campinas : Journal of the Brazilian Chemical Society, 2003, Vol. 14.*

108. ***Mullins, Oliver C. and Sheu, Eric Y.*** *Structures and Dynamics of Asphaltenes. s.l. : Springer, 1999.*

109. ***Andreatta, Gaelle., Bostrom, Neil and Mullins, Oliver C.*** *Ultrasonic Spectroscopy of Asphaltene Aggregatiion. [book auth.] Mullins Oliver C. Asphaltenes, heavy Oils and Petroleomics. New York : Springer, 2007, pp. 231-257.*

110. Chapter2: Chemical and Physical Studies of Petroleum Asphaltenes. ***Speight, James G.*** *Part A, 1994, Developments in Petroleum Science, Vol. 40, pp. 7-65.*

111. Single Molecule Force Spectroscopy of Asphaltene Aggregates. ***Long, Jun, Xu, Zhenghe and Masliyah, Jacob H.*** *Edmonton, Alberta : s.n., 2007, Langmuir, Vol. 23, pp. 6182-6190.*

112. Conformational Dependence of Raman Frequencies and Intensities in Alkanes and Polyethene. ***Koglin, E. and Meier, R.J.*** *3-4, 1999, Computational and Theoretical Polymer Science, Vol. 9, pp. 327-333.*

113. Chain Conformation of Aerosol OT in Water-in-Oil Microemulsions as Studied by Laser Raman Spectroscopy. ***Jain, Tanoj Kumar and Maitra, Amarnath.*** *1989, Colloids and Surfaces, Vol. 36, pp. 87-95.*

114. Thermodynamics of micellization of Aerosol OT in polar and nonpolar solvents. A calorimetric study. ***Mukherjee, Kallol, Moulik, S. P. and Mukherjee, D. C.*** *7, 1993, Langmuir, Vol. 9, pp. 1727-1730.*

115. Sum-Frequency Vibrational Spectroscopy of the Solid/Liquid Interface. ***Bain, Colin D.*** *9, 1995, Journal of the Chemical Society, Faraday Transitions, Vol. 91, pp. 1281-1296.*

116. Aggregation Processes in Micellar Solutions: A Raman Study. ***Cazzolli, G., et al.*** *2012, Journal of Raman Spectroscopy.*

117. ***McCreery, Richard L.*** *Raman Spectroscopy for Chemical Analysis. s.l. : John Wiley & Sons, Inc., 200.*

118. ***Zhang, Z-M, et al.*** *An Intelligent Background-Correction Algorithm for Highly Fluorescent Samples in Raman Spectroscopy. Journal of Raman Spectroscopy. 2009, Vol. 41, pp. 659-669.*

119. Baseline Correction Using Adaptative Iteratively Reweighted Penalized Least Squares. ***Zhang, Z-M, Chen, S. and Liang, Y-Z.*** *2010, Analyst, Vol. 135, pp. 1138-1146.*

APPENDIX A: airPLS algorithm

Analysis

```
% ------- Initial loading of Data ----------------------------------
---------

% folder = input('Enter folder analysis: \n','s');
folder = 'Stryker_new'
path_to_data = ['raw_data/' folder];
[name, hdr, Date, Time, Date_serial, Elapsed_time, wavenumber,
intensity] = myloadfun(path_to_data);

x = wavenumber;
y = intensity;

% x = (1/785 - 1./x)*10^7; % Change nm to wavenumber

% Filtering of the data based range
I = find(x>4100 | x<200); % this data is funky
x(I) = [];
y(I,:) = [];

% Delete data before initial time
interval = input('Enter time interval in hrs: \n'); % input: [1 5]
if ~isempty(interval)
      rxn_start = interval(1);
      rxn_end = interval(2);

      J = find(Elapsed_time<rxn_start | Elapsed_time>rxn_end);
      Elapsed_time(J) = [];
      y(:,J) = [];
end

% Delete data when the spectrometer is saturated
strip = [];
maxout = 68:220;
for j=1:size(y,2)
      if max(y(maxout,j)) > 64000
            strip = [strip j];
      end
end
y(:,strip) = [];
Elapsed_time(strip) = [];

% ------- airPLS ---------------------------------------------------
---------
%
% Dependancies:
%   airPLS.m       Baseline correction using adaptive iteratively
reweighted
```

```
%                   Penalized Least Squares
%
% References:
%   Zhang, Z.-M., Chen, S., & Liang, Y.-Z. (2010). Baseline correction
using
%   adaptive iteratively reweighted penalized least squares. The
Analyst,
%   135(5), 1138â€“46. doi:10.1039/b922045c

lambda = 10e3;
[y_pls, backgr_pls] = airPLS(y', lambda, 2);
backgr_pls = backgr_pls';
y_pls = y_pls';

% % Savitsky-Golay smoothing filter along time axis
% p=3; % filter order
% n = 5; % filter length
% y_pls = sgolayfilt(y_pls',p,n);
% y_pls = y_pls';

% Simple data export - for use in matplotlib/gnuplot to produce better
quality plots
% folder = input('Processed data to be stored in: \n','s');
path_proc_data = ['proc_data/',folder];
[s, mess, messid] = mkdir(path_proc_data);
csvwrite([path_proc_data,'/x.csv'],x);
csvwrite([path_proc_data,'/y.csv'],y);
csvwrite([path_proc_data,'/t.csv'],Elapsed_time');
csvwrite([path_proc_data,'/y_backgr_airpls.csv'],backgr_pls);
csvwrite([path_proc_data,'/y_corr_airpls.csv'],y_pls);

% Generate data file for plotting in GNUplot
% set pm3d interpolate 0,0
% unset surface
% set key outside
% splot "surfacedata_airpls.txt"

FID = fopen([path_proc_data,'/surfacedata_raw.txt'],'w');
for i=1:length(Elapsed_time)
     fprintf(FID,'%f %f %f\n', [x,
repmat(Elapsed_time(i),length(x),1), y(:,i)]');
    fprintf(FID,'\n');
end
fclose(FID);

FID = fopen([path_proc_data,'/surfacedata_airpls.txt'],'w');
for i=1:length(Elapsed_time)
     fprintf(FID,'%f %f %f\n', [x,
repmat(Elapsed_time(i),length(x),1), y_pls(:,i)]');
    fprintf(FID,'\n');
end
fclose(FID);
```

```
% % ------- CWT ------------------------------------------------------
-----------
% %
% % Dependancies:
% %  R Packages:
% %   baselineWavelet obtained from
https://code.google.com/p/baselinewavelet/
% %   R.matlab        not currently being used
% %
% % References:
% %   Zhang, Z.-M., Chen, S., Liang, Y.-Z., Liu, Z.-X., Zhang, Q.-M.,
% %   Ding, L.-X., â€¦ Zhou, H. (2009). An intelligent background-
correction
% %   algorithm for highly fluorescent samples in Raman spectroscopy.
Journal of
% %   Raman Spectroscopy, 41(6), 659â€“669. doi:10.1002/jrs.2500
% %
% % Parameters used in performing cwt baseline correction can be
modified inside
% % the file baselinewaveletscript458.R
% % Default paramaters are:
% %  threshold = 0.05
% %  lambda = 100
% %  SNR = 1
% %  ridgeLength = 5

% % Process data using baselinewaveletscript.R script
% fprintf('Processing data ...')
% command = ['R CMD BATCH baselinewaveletscript458.R'];
% [status, result] = system(command);
% if status ~= 0
%     fprintf(result)
% end
% fprintf('Processing data completed \n')

% backgr_cwt = csvread('y_backgr_cwt.csv');
% y_cwt = csvread('y_corr_cwt.csv');

% % Generate data file for plotting in GNUplot
% % set pm3d interpolate 0,0
% % unset surface
% % set key outside
% % splot "surfacedata_cwt.txt"

% FID = fopen('surfacedata_cwt.txt','w');
% for i=1:length(Elapsed_time)
%    fprintf(FID,'%f %f %f\n', [x,
repmat(Elapsed_time(i),length(x),1), y_cwt(:,i)]');
%     fprintf(FID,'\n');
% end
```

```
% fclose(FID);


% ------- LSD method ------------------------------------------------
---------
%
% Not implemented yet - Still have to go through python script sent
from author
% and fix it up
%
% Dependancies:
%   Python Packages:
%   Numpy
%   Scipy
%
% References:
%   Rowlands, C., & Elliott, S. (2011). Automated algorithm for
baseline
%   subtraction in spectra. Journal of Raman Spectroscopy, 42(3),
363â€“369.
%   doi:10.1002/jrs.2691
```

airPLS

```
function [Xc,Z]= airPLS(X,lambda,order,wep,p,itermax)
%  Baseline correction using adaptive iteratively reweighted Penalized
Least Squares;
%  Input
%         X:row matrix of spectra or chromatogram (size m*n, m is
sample and n is variable)
%         lambda: lambda is an adjustable parameter, it can be
adjusted by user. The larger lambda is, the smoother z will be
%         order: an integer indicating the order of the difference of
penalties
%         wep: weight exception proportion at both the start and end
%         p: asymmetry parameter for the start and end
%         itermax: maximum iteration times
%  Output
%         Xc: the corrected spectra or chromatogram vector (size m*n)
%         Z: the fitted vector (size m*n)
%  Examples:
%         Xc=airPLS(X);
%         [Xc,Z]=airPLS(X,10e9,2,0.1,0.5,20);
%  Reference:
%         (1) Eilers, P. H. C., A perfect smoother. Analytical
Chemistry 75 (14), 3631 (2003).
%         (2) Eilers, P. H. C., Baseline Correction with Asymmetric
Least
%         Squares Smoothing,
http://www.science.uva.nl/~hboelens/publications/draftpub/Eilers_2005.
pdf
%         (3) Gan, Feng, Ruan, Guihua, and Mo, Jinyuan, Baseline
correction by improved iterative polynomial fitting with automatic
threshold. Chemometrics and Intelligent Laboratory Systems 82 (1-2),
59 (2006).
%
%  zhimin zhang @ central south university on Mar 30,2011

if nargin < 6
    itermax=20;
  if nargin < 5
     p=0.05;
    if nargin < 4
       wep=0.1;
      if nargin < 3
          order=2;
          if nargin < 2
               lambda=10e7;
              if nargin < 1
                   error('airPLS:NotEnoughInputs','Not enough input
arguments. See airPLS.');
              end
          end
      end
```

```
    end
  end
end

[m,n]=size(X);
wi = [1:ceil(n*wep) floor(n-n*wep):n];
D = diff(speye(n), order);
DD = lambda*D'*D;
for i=1:m
    w=ones(n,1);
    x=X(i,:);
    for j=1:itermax
        W=spdiags(w, 0, n, n);
        C = chol(W + DD);
        z = (C\(C'\(w .* x')))';
        d = x-z;
        dssn= abs(sum(d(d<0)));
        if(dssn<0.001*sum(abs(x)))
            break;
        end
        w(d>=0) = 0;
        w(wi)   = p;
        w(d<0)  = j*exp(abs(d(d<0))/dssn);
    end
    Z(i,:)=z;
end
Xc=X-Z;
```

Myloadfun

```
function [name, hdr, Date, Time, Date_serial, Elapsed_time,
wavenumber, intensity] = myloadfunc(path_to_data)
% For automation file reading and plotting

fnames = dir([path_to_data '/text_files/*.txt']);
for K =1:length(fnames)
      FID = fopen([path_to_data '/text_files/' fnames(K).name]);
      name{K} = strrep(fnames(K).name(1:end-4),'_',' ');
      hdr{K} = textscan(FID,'%s',17,'delimiter','\t');
      Date{K} = hdr{K}{1}{3}([11:17 31:34]);
      Time{K} = hdr{K}{1}{3}([18:25]);
      Date_serial(K) = datenum([Date{K} Time{K}], 'mmm dd
yyyyHH:MM:SS');
      Elapsed_time(K) = (Date_serial(K) - Date_serial(1))*24; % time in
hours
      temp = textscan(FID,'%f %f');
      if K == 1
            wavenumber = temp{1};
      end
      intensity(:,K) = temp{2};
      fclose(FID);
end
```

APPENDIX B: Normalization of the Raman spectra

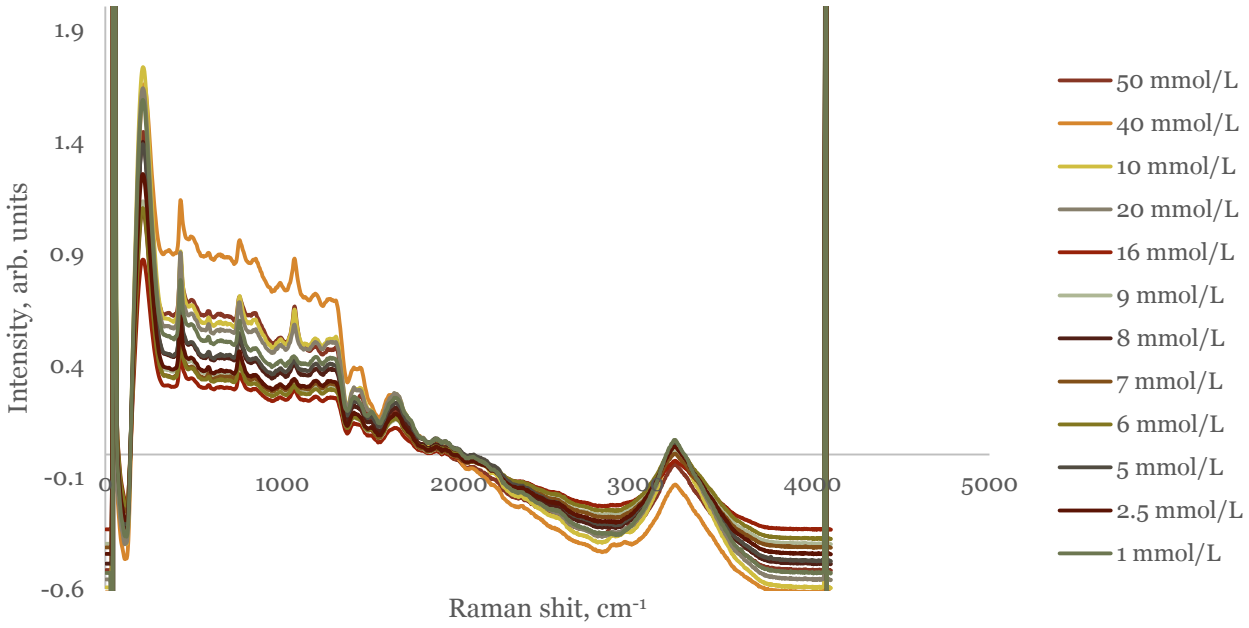

Figure A-1: Raman spectra of SDS dilutions in water after normalization with the standardize function in Excel

APPENDIX C: Validation of the Raman set-up for non-reactive systems

Observation of common solvents with the Raman spectrometer

Methyl Naphthalene

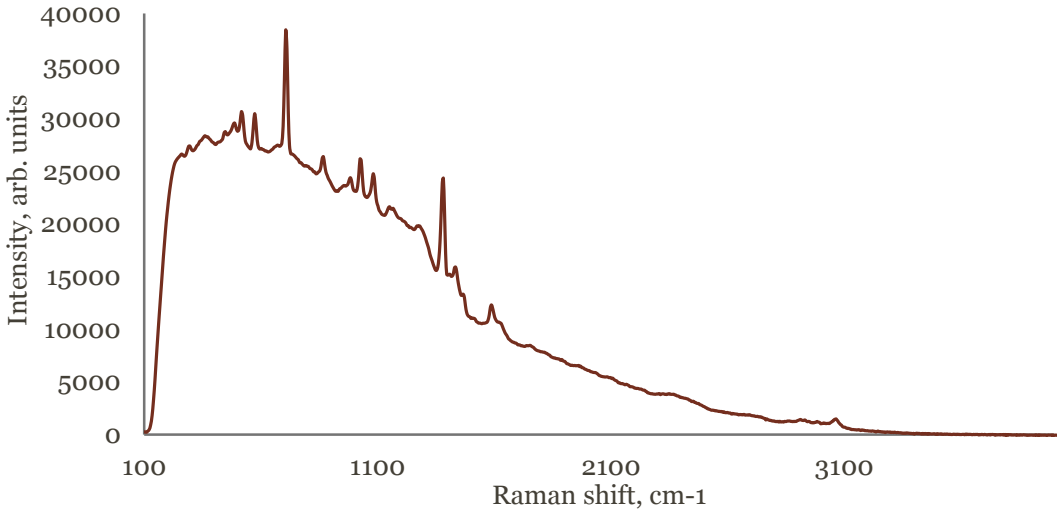

(a)

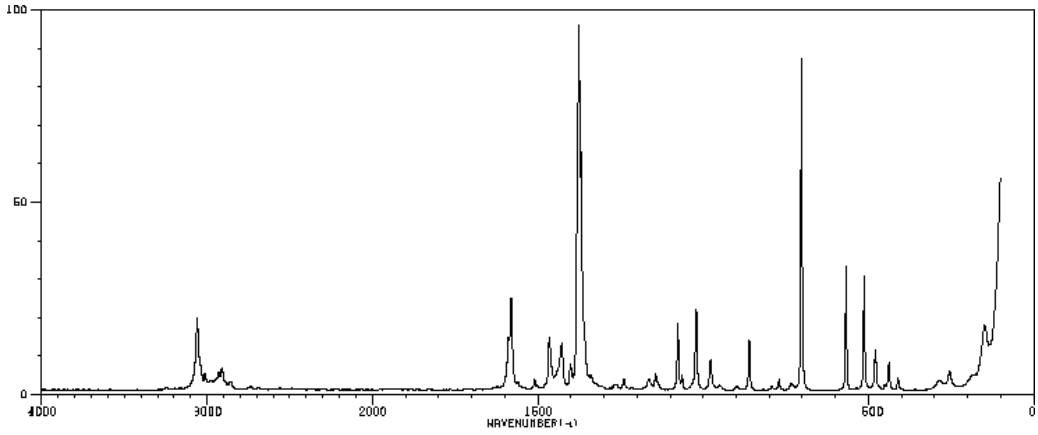

1-METHYLNAPHTHALENE
SDBSNO = 1347 $C_{11}H_{10}$ RM-01-03317 : 4880A.200M.LIQUID

3061	19	614	30
1581	24	480	11
1467	14	149	17
1429	13		
1377	94		
1078	18		
1028	22		
862	13		
703	86		
669	33		

Figure A-2: (a) Experimental Raman spectrum of 1-MethylNaphthalene; (b) Raman spectrum of 1-Methyl Naphthalene published on the SDBS website (76)

APPENDIX D: Baseline and Raman spectra of aqueous solutions of SDS

Raman spectrum of the sapphire window

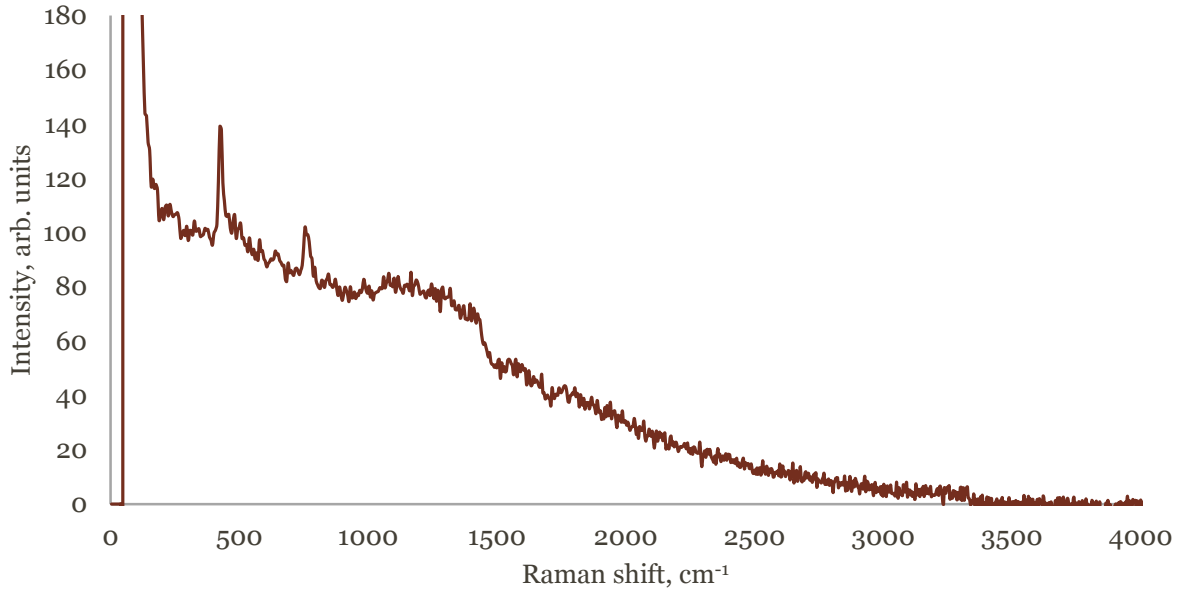

Figure A-3: Raman spectrum of the sapphire glass. The baseline illustrated in this spectrum is the same one presents in the signals of aqueous solutions of SDS and AOT

Raman spectra of aqueous solutions of SDS

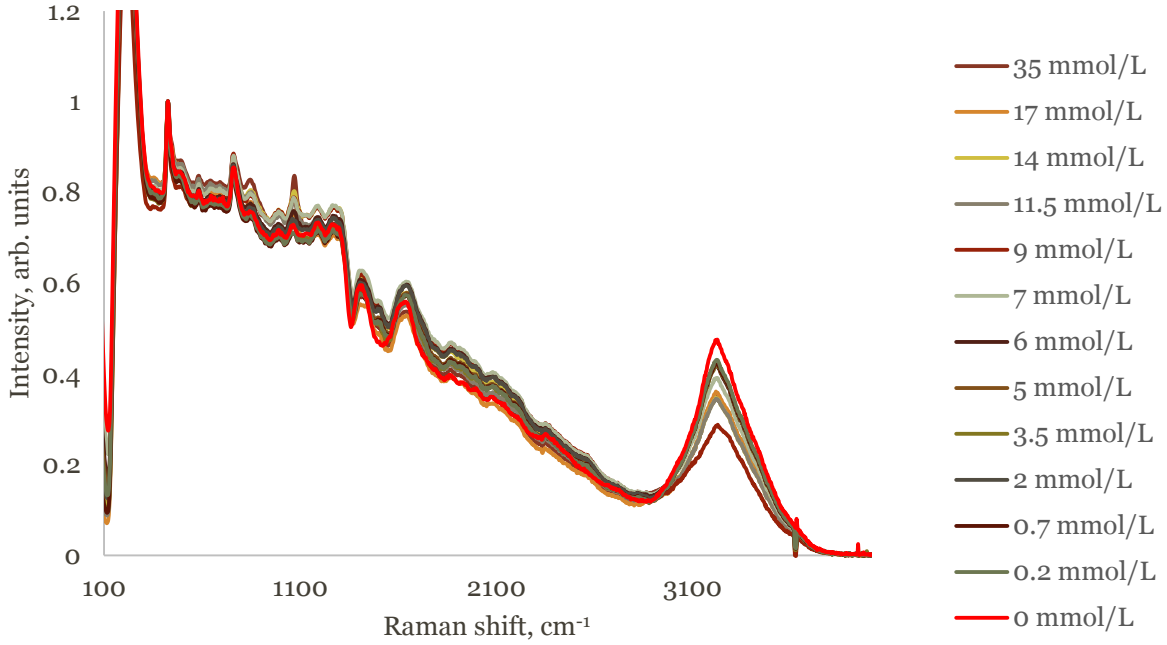

Figure A-4: Raman spectra of aqueous solutions of SDS (3 march)

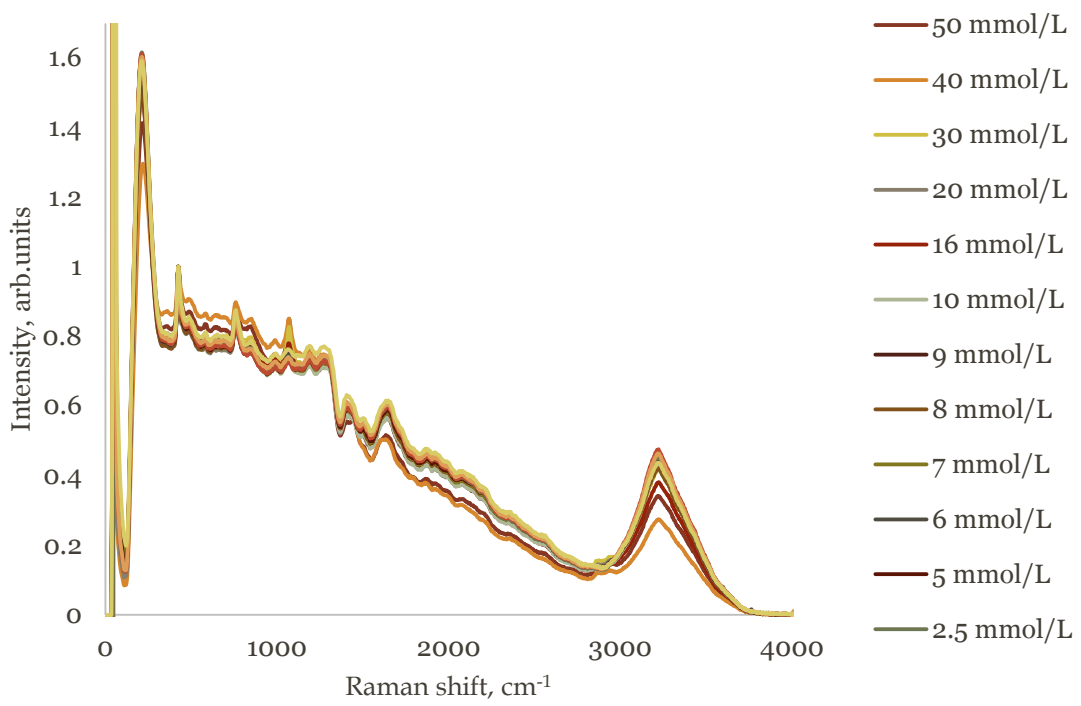

Figure A-5: Raman spectra of aqueous solutions of SDS (6 march)

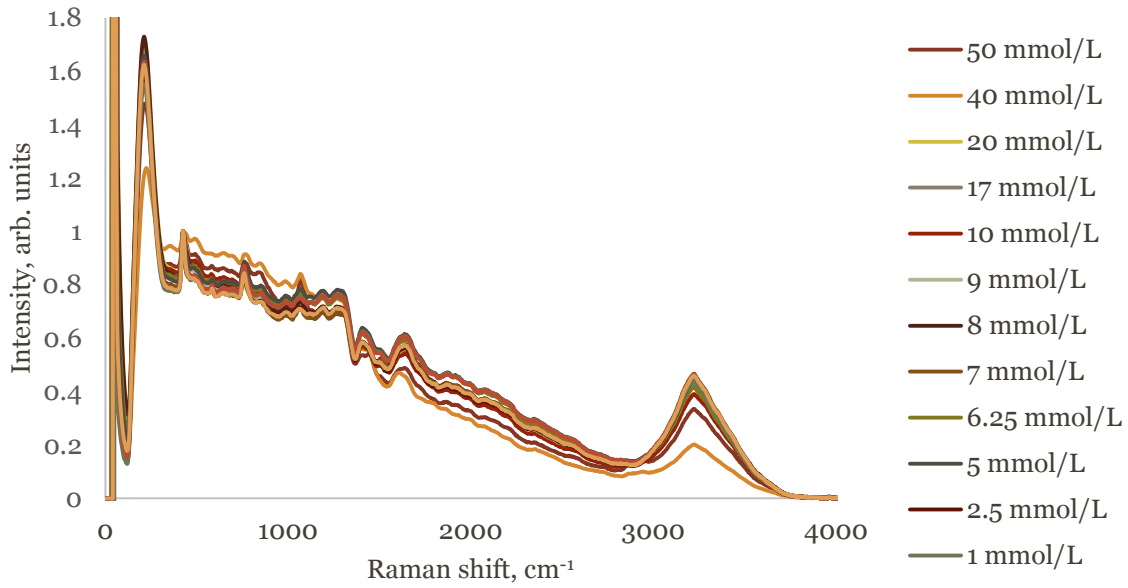

Figure A-6: Raman spectra of aqueous solutions of SDS (13 march)

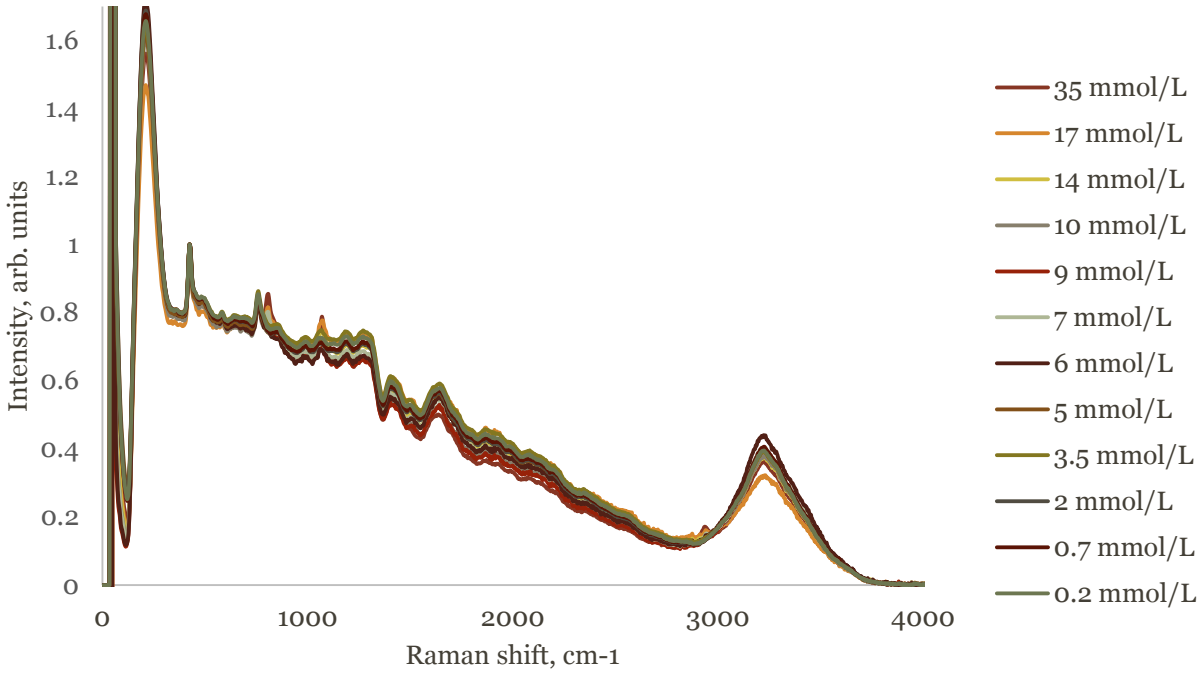

Figure A-7: Raman spectra of aqueous solutions of SDS (25 feb)

APPENDIX E: Raman spectra of aqueous solutions of AOT

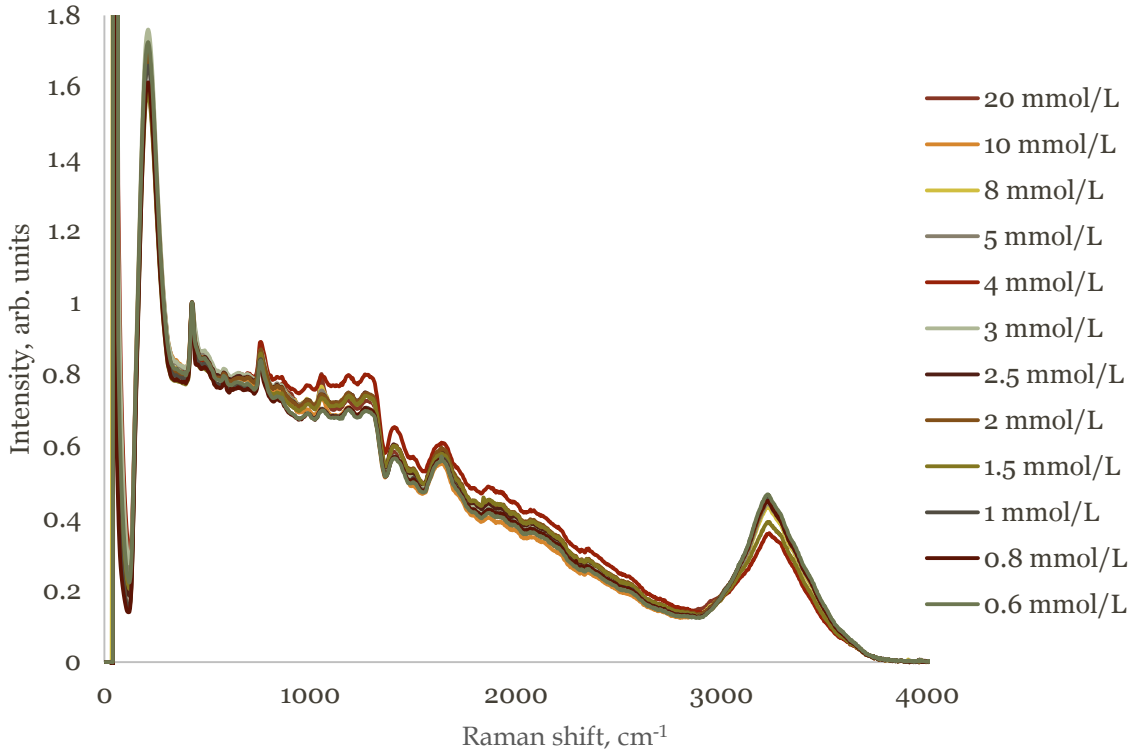

Figure A-8: Raman spectra of aqueous solutions of AOT (21 april)

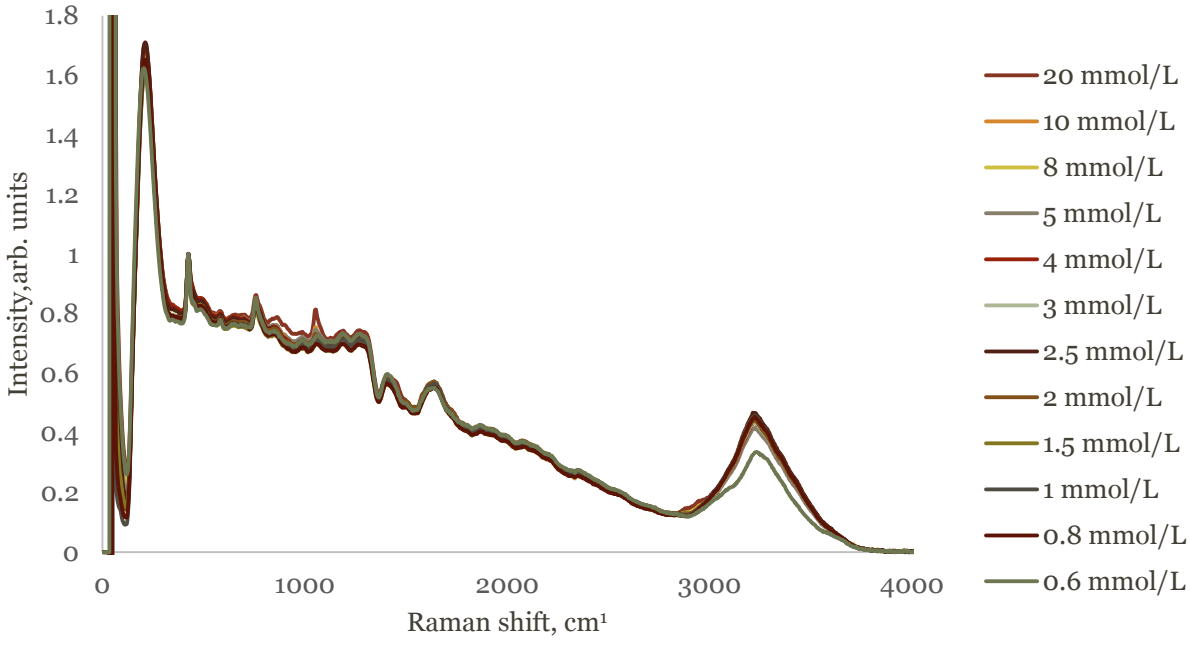

Figure A-9: Raman spectra of aqueous solutions of AOT (22 april)

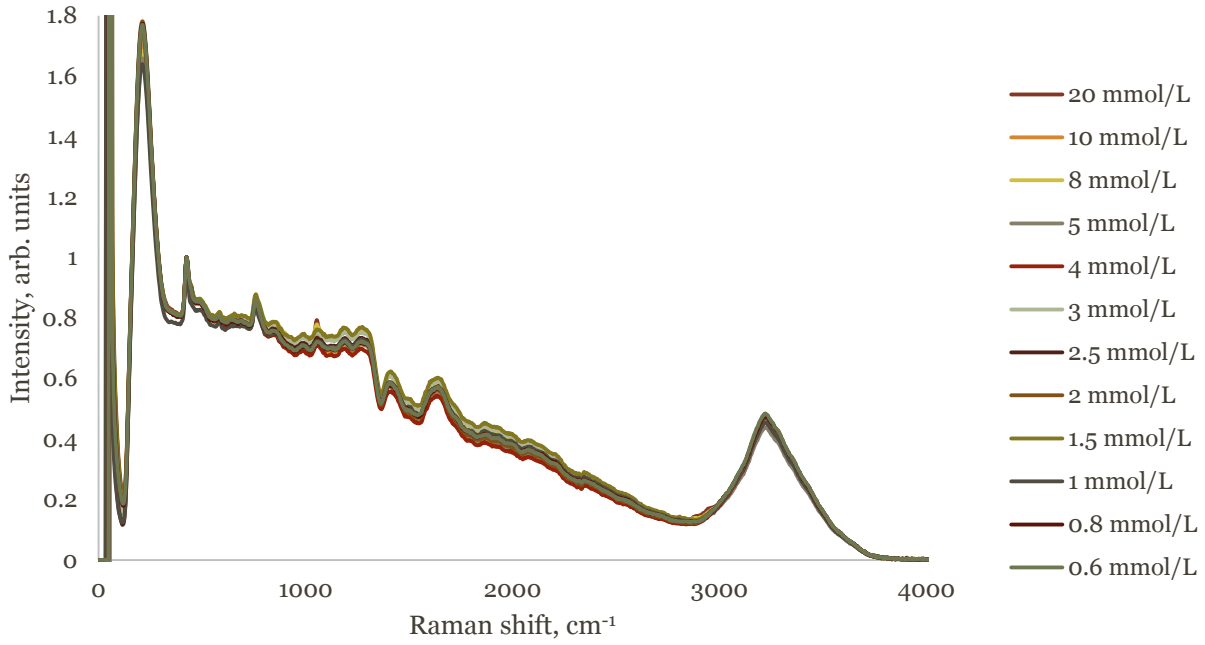

Figure A-10: Raman spectra of aqueous solutions of AOT (23 april)

APPENDIX F: Solutions of VR in toluene

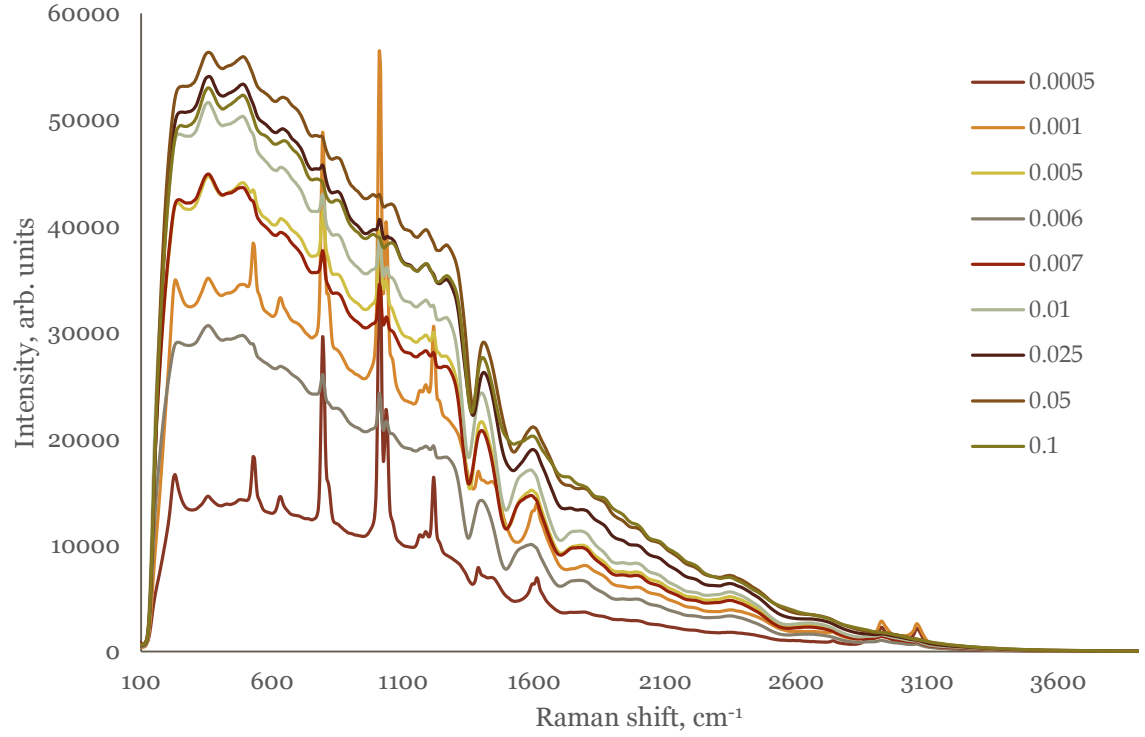

Figure A-11: Averaged Raman spectra of VR solutions in toluene, acquired during the first observation date

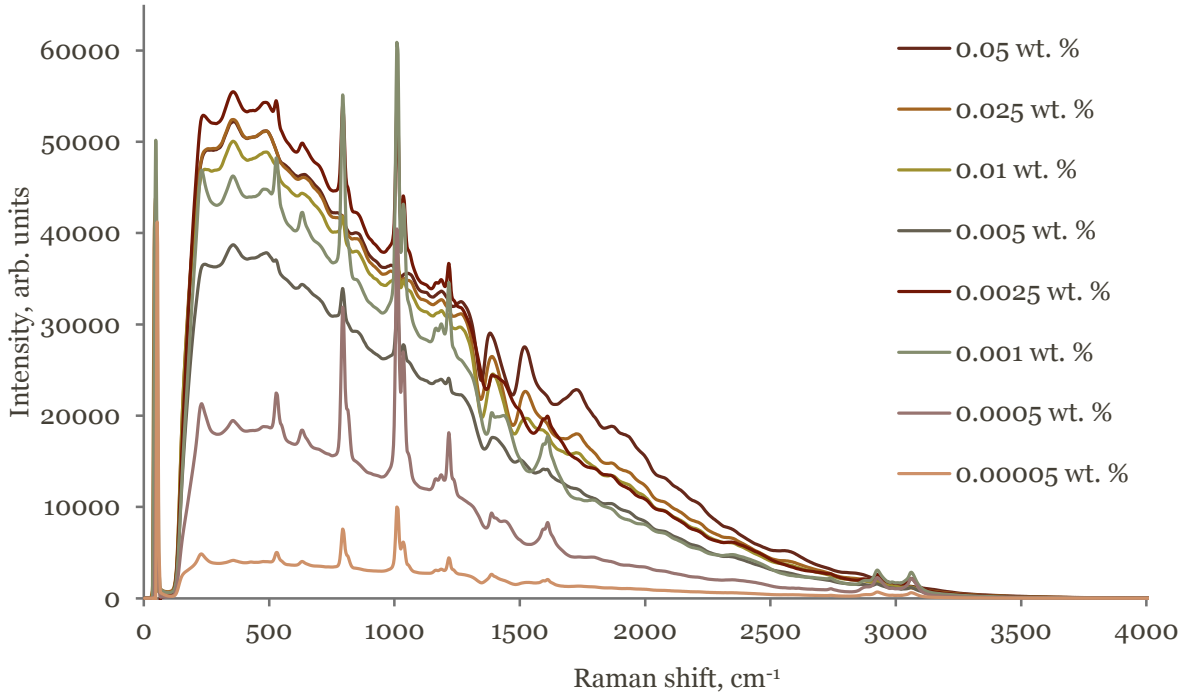

Figure A-12: Averaged Raman spectra of VR solutions in toluene, acquired during the second observation date

APPENDIX G: VR/ water/toluene microemulsions

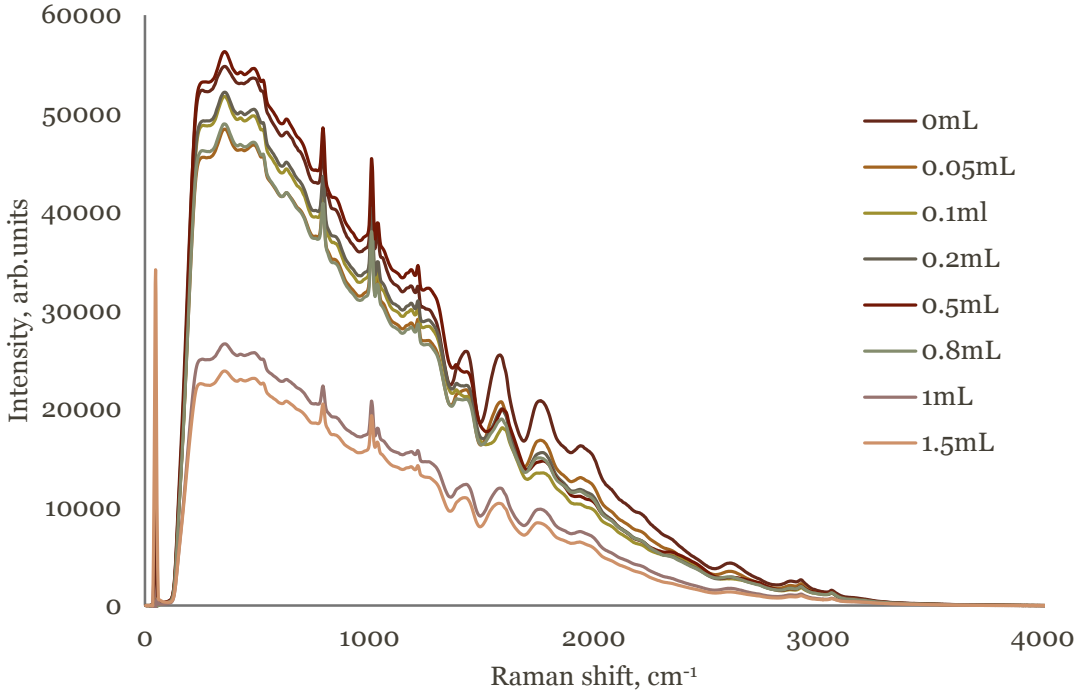

Figure A-13: VR/water/toluene microemulsions prepared in 0.0025 wt. % VR in toluene

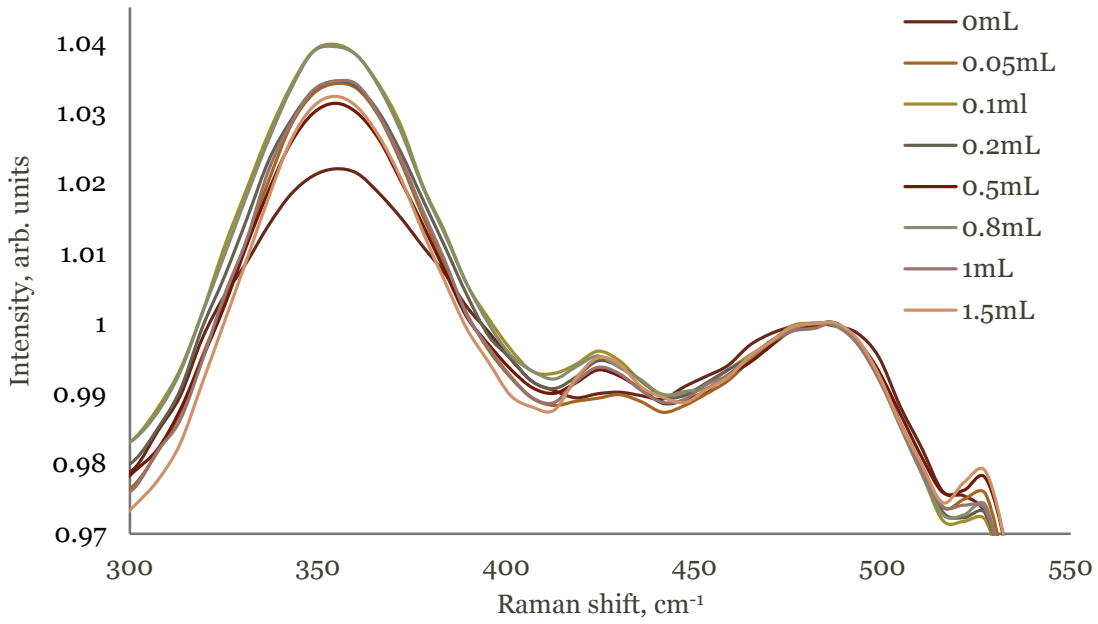

Figure A-14: Intensity variation in the 550-300 cm^{-1} region for VR/water/toluene microemulsions (0.0025 wt. % VR in toluene)

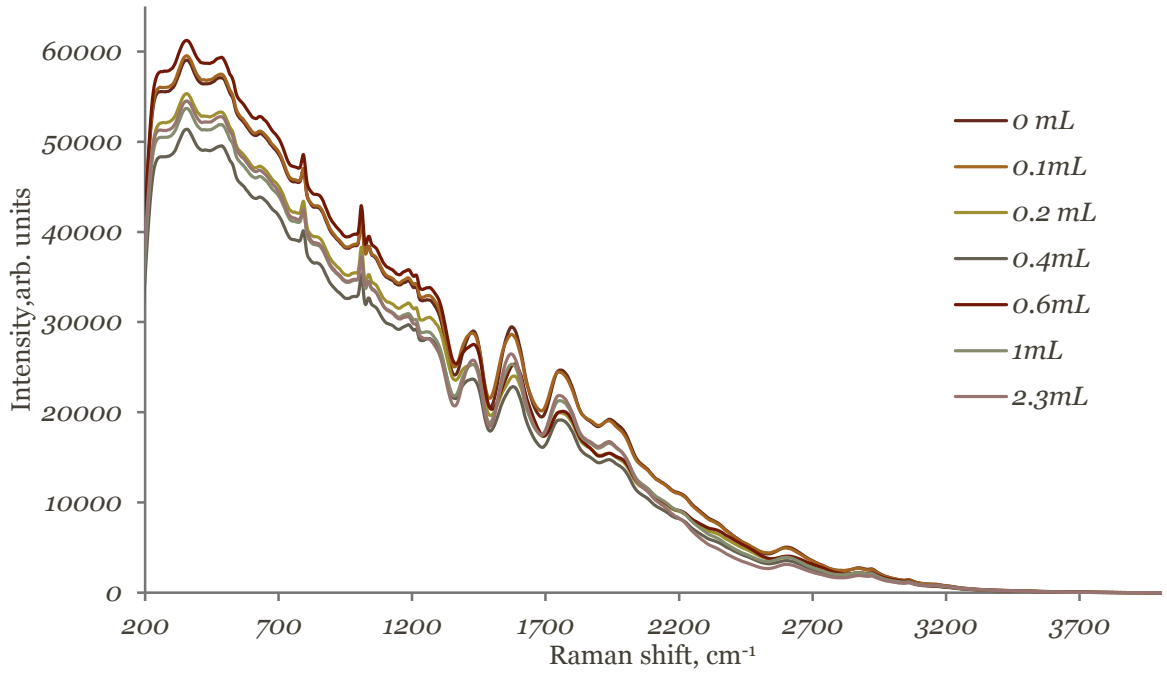

Figure A-15: VR/water/toluene microemulsions prepared in 0.005 wt. % VR in toluene

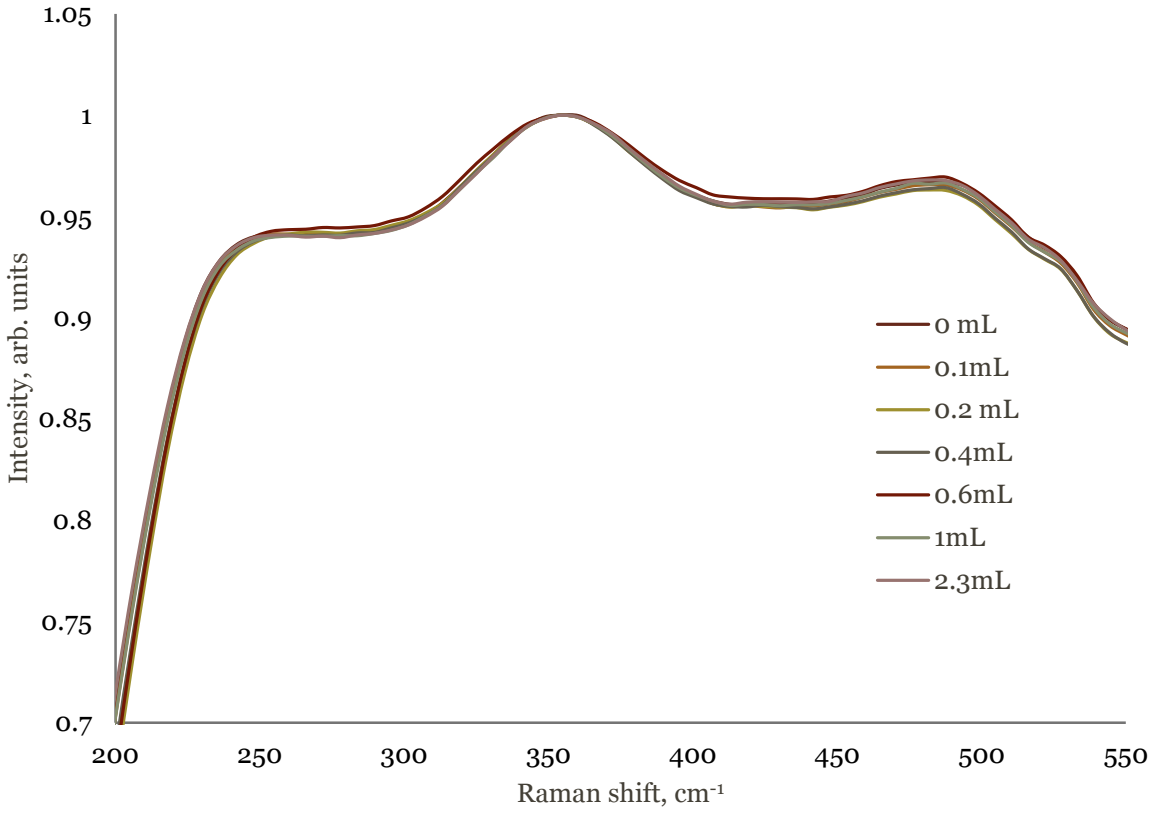

Figure A-16: Intensity variation in the 550-200 cm-1 region for VR/water/toluene microemulsions (0.005 wt. % VR in toluene)